PRO-SIS

Sviluppo e disseminazione di algoritmi per il progetto delle innovative strategie di protezione sismica “CONSTRAIN” e applicazione pilota su edifici esistenti in muratura

Razvoj in diseminacija postopkov za projektiranje inovativnega načina potresnega utrjevanja obstoječih zidanih stavb “CONSTRAIN”

Report 1.1
Modelli analitici di dimensionamento

Poročilo 1.1
Analitični modeli za dimenzioniranje

SETTEMBRE 2024

SEPTEMBER 2024

Authors: Gattesco N.[1], Boem I.[1], Rizzi E.[1], Gams M.[2]

(1) Department of Engineering and Architecture, University of Trieste (Italy)

(2) Faculty of Civil and Geodetic Engineering, University of Ljubljana (Slovenia)

www.ita-slo.eu/pro-sis

https://www.facebook.com/61556327101140

https://www.linkedin.com/showcase/interreg-italia-slovenija-pro-sis

PRO-SIS

Development and dissemination of procedures for designing an innovative way seismic strengthening of existing masonry buildings "CONSTRAIN"

Report 1.1
Analytic model for dimensioning

SEPTEMBER 2024

Authors: Gattesco N.[(1)], Boem I.[(1)], Rizzi E.[(1)], Gams M. [(2)]

(1) Department of Engineering and Architecture, University of Trieste (Italy)

(2) Faculty of Civil and Geodetic Engineering, University of Ljubljana (Slovenia)

www.ita-slo.eu/pro-sis

https://www.facebook.com/61556327101140

https://www.linkedin.com/showcase/interreg-italia-slovenija-pro-sis

Interreg
Italia-Slovenija
PRO-SIS

Cofinanziato dall'Unione europea
Sofinancira Evropska unija

2021 2027

Report 1.1
Analytic model for dimensioning

Summary

1. Introduction ... 3
2. Summary of the “CONSTRAIN” experimental program ... 4
3. Strengthening with CRM ... 5
3.1. Technique characteristics ... 5
3.2. In-plane behaviour of piers ... 7
3.2.1. Summary and analysis of the experimental results ... 7
3.2.2. Analytic model ... 27
3.2.3. Application and validation ... 30
3.3. In-plane behaviour of spandrels ... 33
3.3.1. Summary and analysis of the experimental results ... 33
3.3.2. Analytic model ... 50
3.3.3. Application and validation ... 54
3.4. Out-of-plane behaviour ... 57
3.4.1. Summary and analysis of the experimental results ... 57
3.4.2. Analytic model ... 65
3.4.3. Application and validation ... 68
4. Roof ring beams with FRP meshes embedded in bed joints ... 70
4.1. Technique characteristics ... 70
4.2. Out-of-plane behaviour ... 71
4.2.1. Summary and analysis of the experimental results ... 71
4.2.2. Analytic model ... 77
4.2.3. Application and validation ... 80
5. Ring beams with externally-bonded FRP strips ... 81
5.1. Technique characteristics ... 81
5.2. Out-of-plane behaviour ... 82
5.2.1. Summary and analysis of the experimental results ... 82

5.2.2. Analytic model 89
5.2.3. Application and validation 91
Acknowledgments 92
References 93
Appendix A. 94
I. Masonry characteristics 94
II. Strengthening materials characteristics 96

1. Introduction

The report collects the results of Activity 1.1 of the "PRO-SIS" project, aimed at the "Development of analytical models to quantify the performances of structures reinforced with the innovative "CONSTRAIN" techniques and validation with experimental results".
The CONSTRAIN project (INTERREG V-A ITALIA-SLOVENIA 2014-2020 - https://2014-2020.ita-slo.eu/it/constrain) was aimed at developing intervention strategies to reduce the seismic vulnerability of existing masonry buildings and assess their effectiveness by means of an extended experimental campaign. The proposed strategies, based on the use of fiber-based composite materials, allow for substantial reductions in seismic vulnerability through interventions executed from the exterior of the buildings, without requiring the relocation of people and belongings inside the buildings.
The aim of the "PRO-SIS" project (INTERREG VI-A ITALIA-SLOVENIA 2021-2027 - https://www.ita-slo.eu/it/pro-sis) is to develop the necessary methods for the proper design and application of these strategies, as well as their application to case-study buildings scheduled for structural improvements in the near future, and the drafting of guidelines concerning the design and execution procedures for the "CONSTRAIN" reinforcement interventions. Accurate analytical and numerical algorithms are developed and calibrated, based on the experimental results of "CONSTRAIN", so to extend the studied cases and provide the designers with robust strategies for the detailed design of the proposed systems with the commonly used automatic calculation softwares.
This document reports the first approach to the definition and calibration of analytical-mechanical models capable of describing the behaviour of the different structural elements subjected to seismic loads (masonry piers and spandrels, walls subjected to out-of-plane bending, roof and floor ring beams). The report is divided into different sections, for each type of "CONSTRAIN" tests performed. For each section, the first part resumes the previously obtained experimental results, providing also a critical review and an interpretation of the resisting mechanisms. In the second part, the proposed analytical model for estimating the behaviour is described; in the third, the analytic method is applied to the experimental samples and compared with the experimental results.

2. Summary of the "CONSTRAIN" experimental program

The list and main characteristics of the experimental tests carried out within the "CONSTRAIN" project are reported in Table 2.1 (each specimen is identified with an alphanumeric string). The main characteristics of the materials are resumed in Appendix A.

Table 2.1: Summary of the experimental program carried out within the CONSTRAIN project

Type of test	Masonry type	Sample ID	Strengthening
In-plane tests on masonry piers	Stone R2	P-R2U	/
	Stone R2	P-R2R-1	CRM on one-side
	Stone R2	P-R2R-2	CRM on two-sides
	Solid brick B2	P-B2U	/
	Solid brick B2	P-B2R-1	CRM on one-side
	Solid brick B2	P-B2R-2	CRM on two-sides
	Solid brick B1	P-B1U	/
	Solid brick B1	P-B1R	CRM on one-side
In-plane tests on masonry spandrels	Stone R2	S-R2U-1	/
	Stone R2	S-R2R-1	CRM on one-side
	Stone R2	S-R2U-2	/
	Stone R2	S-R2R -2	CRM on two-sides
	Solid brick B2	S-B2U-1	/
	Solid brick B2	S-B2R-1	CRM on one-side
	Solid brick B1	S-B1U-1	/
	Solid brick B1	S-B1R-1	CRM on one-side
Out-of-plane tests on piers	Stone R2	B-R2	CRM on one-side
	Solid brick B2	B-B2	CRM on one-side
	Solid brick B1	B-B1	CRM on one-side
Pushover tests on a pilot building	Stone R2	PB-U	/
	Stone R2	PB-R	CRM on one-side
Out-of-plane tests on roof ring beams	Stone R2	T-R2	GFRP mesh in bed joints
	Solid brick B1	T-B1	GFRP mesh in bed joints
Out-of-plane tests on floor ring beams	Stone R2	C-R2	CFRP eccentric strips
	Solid brick B1	C-B1	CFRP eccentric strips

3. Strengthening with CRM

3.1. Technique characteristics

The Composite Reinforced Mortar - CRM technique (Fig. 3.1.1) can be generally adopted to improve the resistance, displacement and dissipative capacities of existing masonry elements in both in-plane and out-of-plane directions. The technique consists in the application, on the masonry surface (one or both sides), of a mortar coating with preformed Fiber-Reinforced Polymer - FRP composite meshes embedded, in combination with the introduction of transversal connectors. In particular, Glass fibres meshes (GFRP) are considered, with a minimum coating thickness of 30 mm.

In addition, FRP "L"-shaped connectors are inserted into holes drilled in the masonry and injected with resin; in front of each connector, a FRP mesh sheet is positioned to distribute stresses within the coating.

In case of application of CRM at both sides of the masonry (Fig. 3.1.2a), the holes passed side-by-side throughout the masonry; one connector for each side is inserted in the hole, so that the two connectors overlapped within the masonry thickness.

In case of application of CRM only on one side of the masonry (Fig. 3.1.2b), a single connector is inserted. However, in case of double or multiple leaves masonry, additional transversal connectors (called "artificial diaton") are also introduced, involving almost the whole masonry thickness, to create the connection between leaves and prevent leaves separation and delamination phenomena (Fig. 3.1.2c). The artificial diaton is composed of a threaded steel bar centred in a cement-based mortar core injected in a transversal hole drilled in the masonry (typically by using a water-cooled core drilling machine) and with a thick steel washer screwed at the head. The term "artificial diaton" recognises a transversal tying element not originally present in the masonry and introduced during the strengthening intervention. In contrast, "non-artificial diaton" or, simply, "diaton", commonly refers as a large stone element arranged as header during the wall construction, connecting the leaves.

The main characteristics for the CRM component materials adopted in the "CONSTRAIN" tests are resumed in Appendix A.

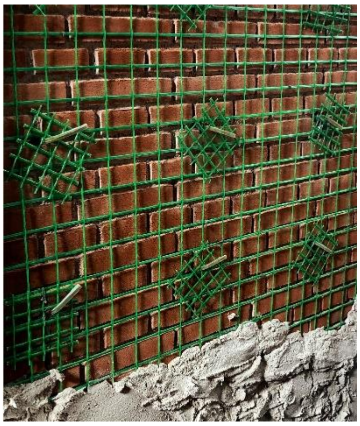

Fig. 3.1.1 Application of the CRM strengthening technique on a masonry wall.

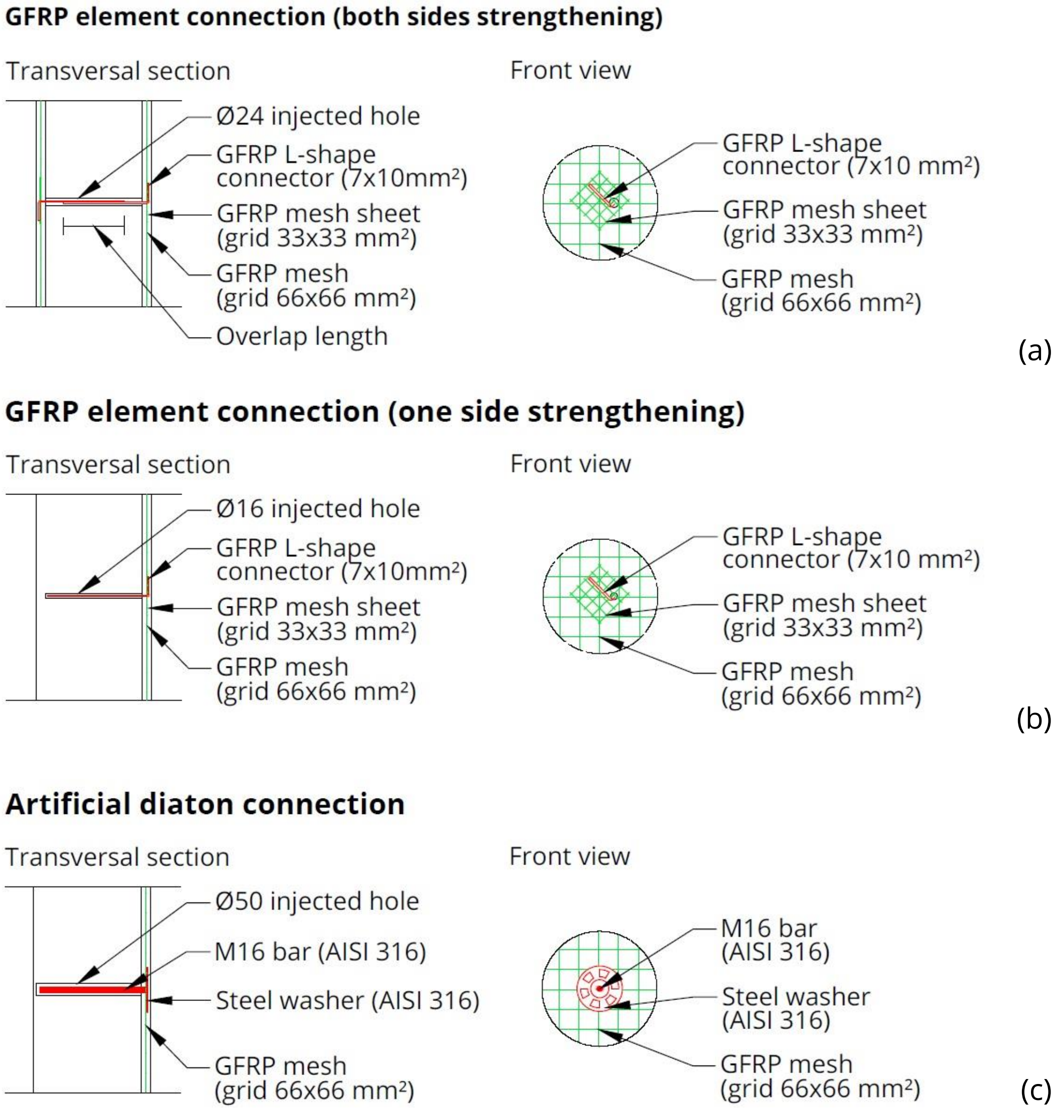

Fig. 3.1.2 Main features of the transversal connectors for the CRM strengthening technique: FRP connection for double-sides (a) and single-side (b) application, and additional "artificial diaton" connection for multiple leaves masonry (c).

3.2. In-plane behaviour of piers

3.2.1. Summary and analysis of the experimental results

The pier samples were rectangular masonry panels having a width of 1500 mm and a height of 1960 mm (Fig. 3.2.1). Each specimen was built between a bottom and a top reinforced concrete (RC) beam 300 mm height, 1500 mm long and with a thickness equal to that of the plain masonry. Three different masonry types were considered: R2, B2 and B1 (Appendix A.). A total of eight panels were built and tested (Table 3.1): three in rubble stone masonry (R2), three in double leaf solid brick masonry (B2), and two in single leaf solid brick (B1) masonry. In the strengthened samples, the CRM layer was extended over the upper and lower RC beams to reproduce the continuity of the strengthening system at the piers' extremities in actual structures. The positioning of the GFRP connectors and of GFRP connectors combined with artificial diatones is schematized in Fig. 3.2.2.

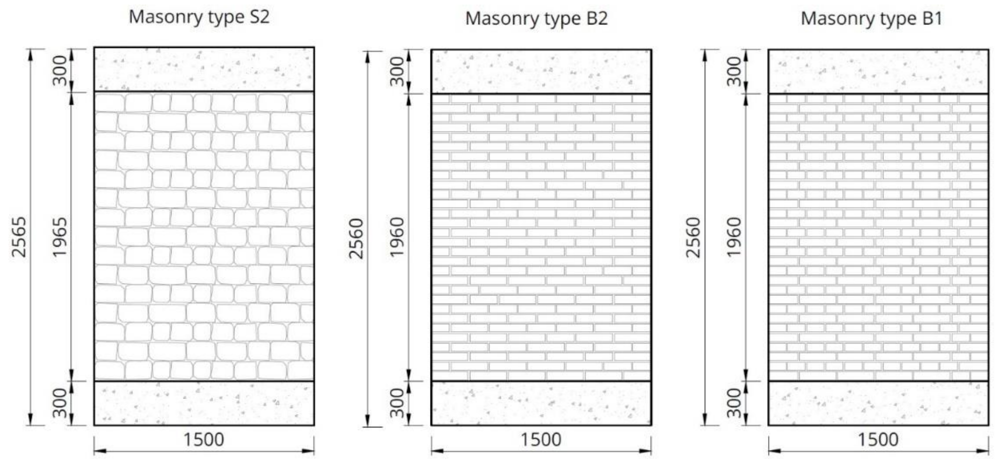

Fig. 3.2.1 Main geometric characteristics of the pier samples.

Table 3.1: Summary of the CONSTRAIN experimental tests on piers

Sample ID	Masonry type	Strengthening system	Connectors
P-R2U	R2	/	/
P-R2R-1	R2	CRM on one-side	GFRP + diatons, 1 side
P-R2R-2	R2	CRM on two-sides	GFRP, passing-through
P-B2U	B2	/	/
P-B2R-1	B2	CRM on one-side	GFRP + diatons, 1 side
P-B2R-2	B2	CRM on two-sides	GFRP, passing-through
P-B1U	B1	/	/
P-B1R-1	B1	CRM on one-side	GFRP, 1 side

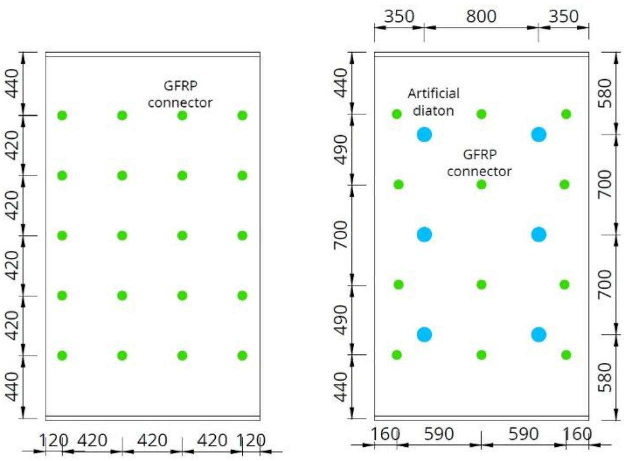

Fig. 3.2.2 Positioning of the connectors in CRM strengthened pier samples.

The test setup is schematized in Fig. 3.2.3: the lower RC beam was bolted to a stiff steel beam fixed to the laboratory floor. The RC beam at the top of the sample was bolted to the upper stiff steel beam of the testing apparatus. At the lateral extremities of the upper steel beam, two electro-mechanical actuators, connected to the floor, were installed to control the amount of vertical axial load and the rotation at the top. During testing, they were governed so as the applied axial load was maintained constant during the tests (axial stress level was 0.5 MPa) and the rotations of the upper steel beam were constrained. A third actuator, positioned at the side of the upper steel beam (left side), at its mid-height, applied the lateral loading, which was applied by cycles with increasing displacement amplitude. Each load amplitude was repeated only once before it was increased.

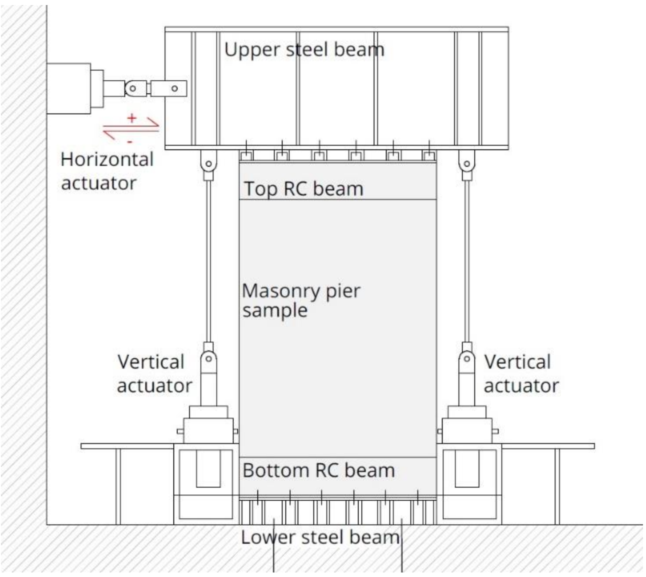

Fig. 3.2.3 Schematization of the test setup for piers.

The behaviour of each sample is described in the following, reporting also monitored loads and displacements and evolution of the crack pattern, which was surveyed at the back side by means of a Digital Image Correlation (DIC) system. The main results are then summarized and compared.

The global behaviour of the pier is described in terms of capacity curves, which show the applied horizontal load V_P (shear force) as a function of the horizontal displacement of the top RC beam d_P. The pier drift γ_P was determined by dividing d_P by the pier's height.

According to the typical in-plane failure mechanisms of historic masonry elements, two groups of cracks were generally expected: mainly hotiontal cracks at the corners of the pier, related to in-plane bending failure, and diagonal cracks in the center of the pier, indicative of an in-plane shear mechanism. For monitoring such occurrances, the relative displacements along the diagonals (d_1 and d_2) and throughout the piers height (d_{vL} and d_{vR}, at left and right side) were monitored at both sides of the pier samples. The diagonal displacements were measured on a base length of about 2365 mm centred in the pier area; the vertical on a base length of about 1960 mm.

In addition, the global vertical displacements between the upper steel beam and the laboratory floor were also measeured (d_{Vtot}) to monitor possible additional movements external to the deformations of the masonry sample. Positive displacements conventionally refer to elongations.

- Test P-R2U (Fig. 3.2.4)

The first damage was observed almost in the middle of the wall, where a sub-vertical crack formed. Then, the crack grew in length with increasing load and other cracks formed from the centre of the panel, with an inclined trend. The diagonal cracks grew and eventually connected the corners of the wall. At the end, the unreinforced stone masonry pier responded in shear, characterised by diagonal cracks: the cracks ran almost exclusively through joints and involved the whole masonry thickness. The progressive opening of diagonal cracks was detected by the diagonal transducers (positive values that alternatively occurred at the opposite diagonals); the vertical transducers evidenced a gradual shortening of the sample during the test.

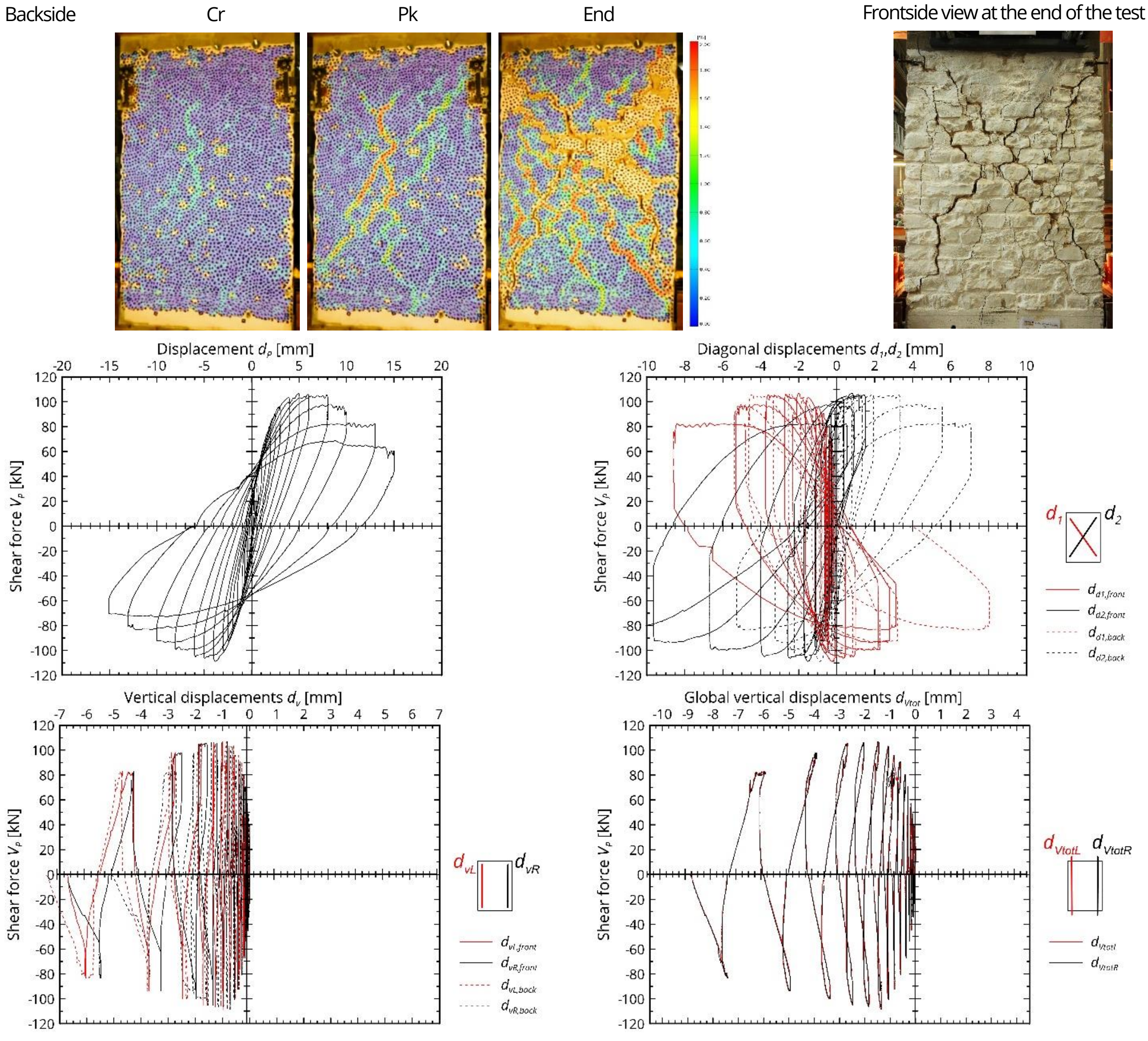

Fig. 3.2.4 Main results of test P-R2U.

- Test P-R2R-1 (Fig. 3.2.5)

It is observed that, before the beginning of the test, the sample had minor cracks in the first mortar bedding and at the base of the coating. This may have likely led to a lower-than-expected initial stiffness, which resulted quite similar to that of the unstrengthened sample.
During the test, damage developed differently on the strengthened and unstrengthened sides: the response and damage on the unstrengthened (front) side were again in shear, which was clear from the diagonal cracks. On the strengthened (back) side, the cracks in the coating were almost vertical initially, at the centre of the sample, only starting to incline when approaching to the maximum resistance; horizontal cracks in the coating also appeared near the corners, indicating the activation of bending. Despite these horizontal cracks, the governing mechanism was shear, as evidently from the alternating elongations detected by the diagonal transducers, whereas the global vertical displacements almost remained negative. (d_{Vtot}) The vertical transducers applied at the two sides of the sample (d_V) behaved differently: those on the unstrengthened side mainly measured a gradual compression, while those applied on the mortar coating detected elongations, likely related to the activation of the bending mechanism. The cracking in the unstrengthened side was concentrated in a few large cracks, whereas the cracking in the coating was widely spread out in much more cracks. Finally, almost at the end of the test, a vertical crack was observed at the sides of the sample and the coating diffusely lost bond with the masonry, except where transversal connectors were present, and the also the coating near some of the steel connectors crumbled and the GFRP mesh fractured.

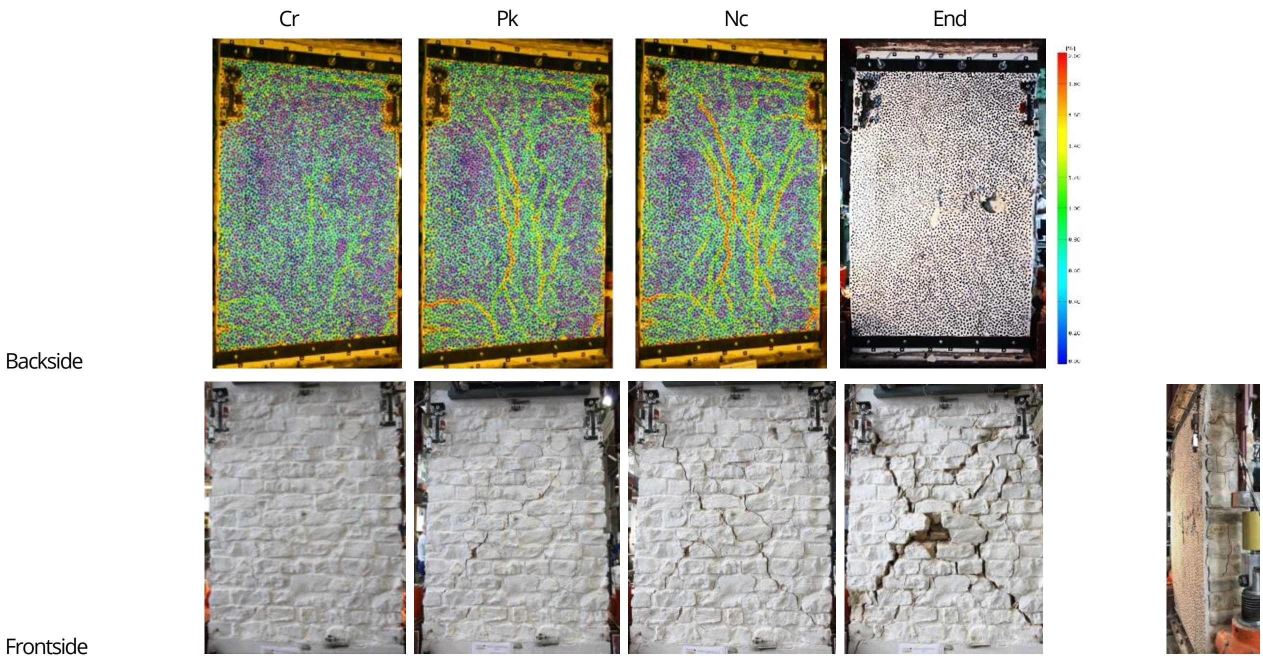

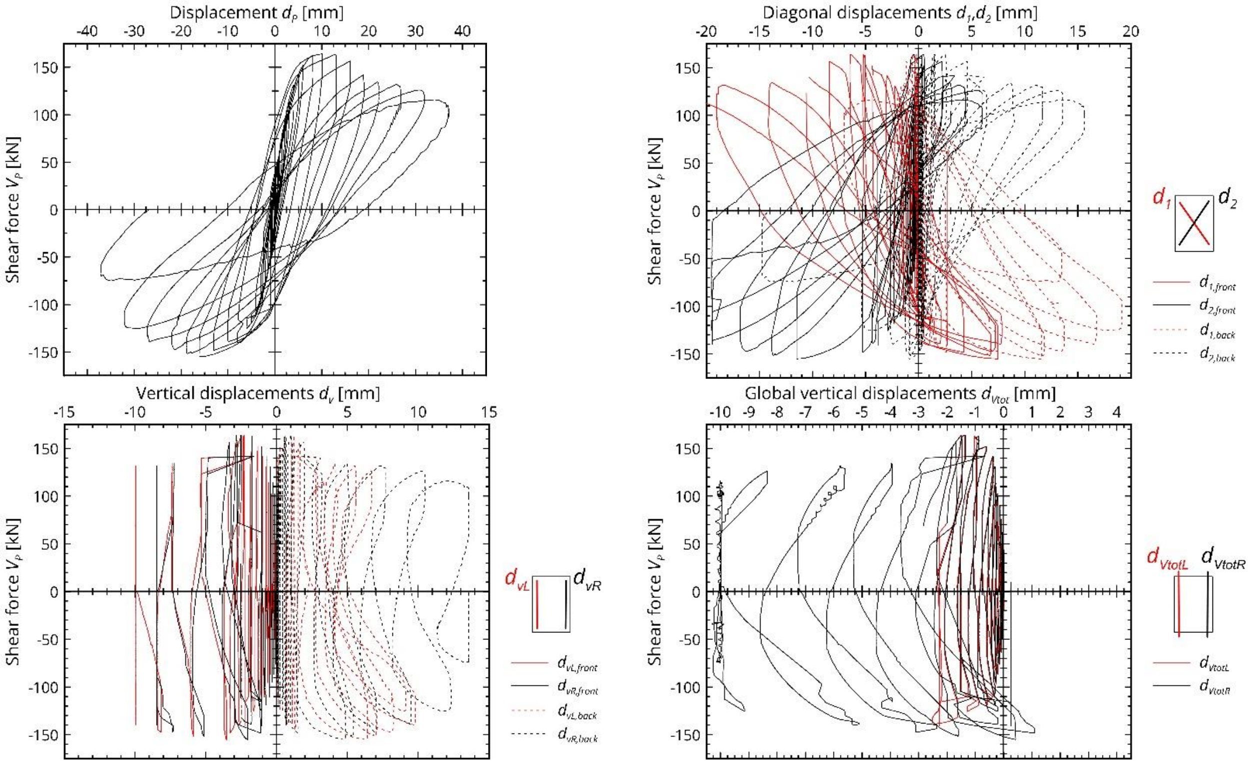

Fig. 3.2.5 Main results of test P-R2R-1

- Test P-R2R-2 (Fig. 3.2.6)

The first cracks were horizontal at the bottom and top corners, indicating the activation of bending damage; however, also some sub-vertical cracks formed at the centre of the sample. When approaching to the maximum resistance, other horizontal, parallel cracks occurred at the corners and several inclined cracks propagated diagonally from the centre of the panel, Horizontal and inclined cracks, widely spread over a large area, indicated the combined activation of bending and shear mechanisms. This was evident also from the consistent elongations monitored by both diagonal and vertical transducers installed on the sample.
Close to the end of the test, the coating diffusely lost the bond with masonry, by connectors. Also, a vertical crack between the wythes developed and gradually widened until the end of the test.

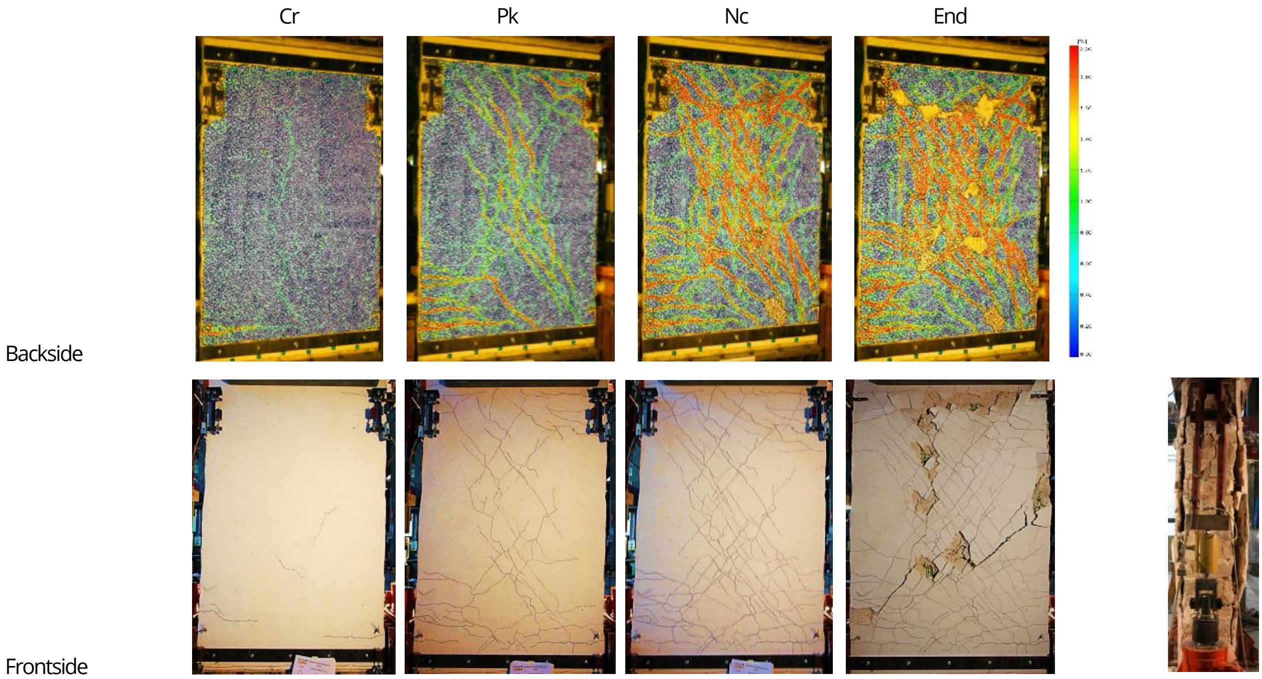

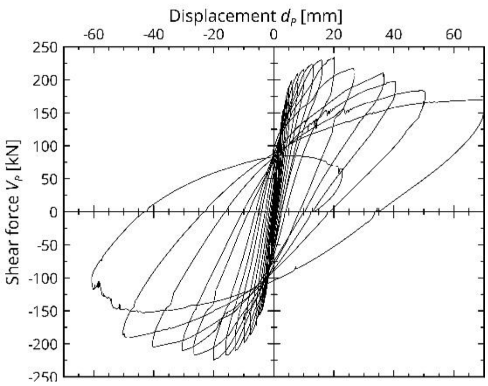

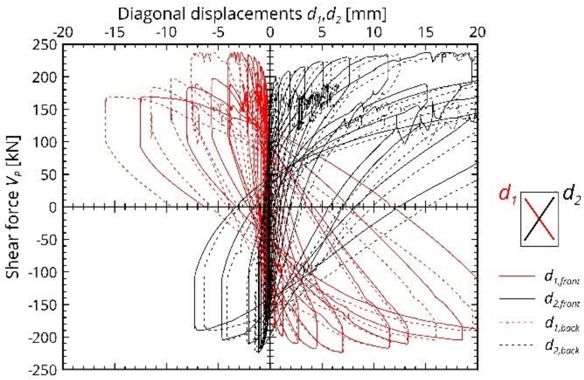

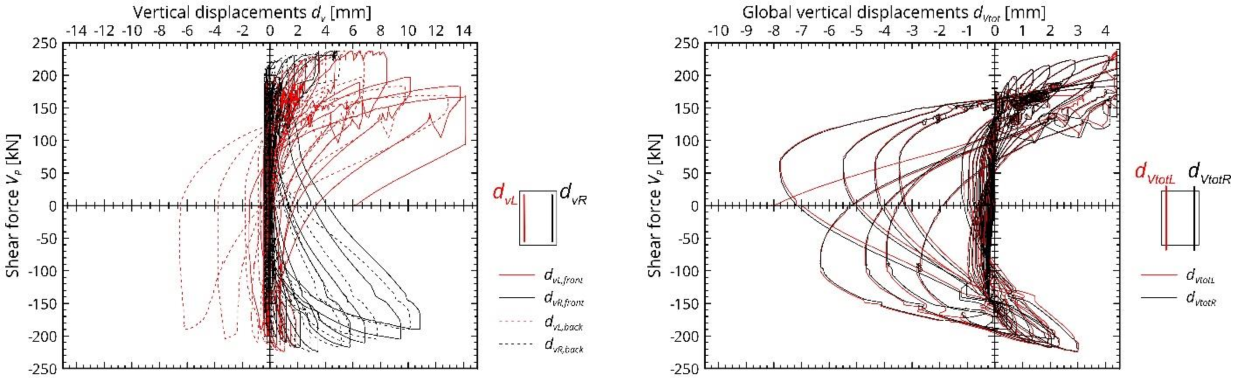

Fig. 3.2.6 Main results of test P-R2R-2.

- Test P-B2U (Fig. 3.2.7)

The pier responded in shear, characterised by diagonal cracks: the first cracks were scattered in bricks and head joints, starting from the centre of the panel and then developing along the diagonal trajectories throughout the whole thickness. The diagonal cracks were monitored by the diagonal transducers (positive values occurring alternatively at the opposite diagonals). The progressive shortening of the sample was surveyed by the vertical transducers (negative values). During the test, also significant cracking at the sides of the sample, due to separation of the leaves, was observed.

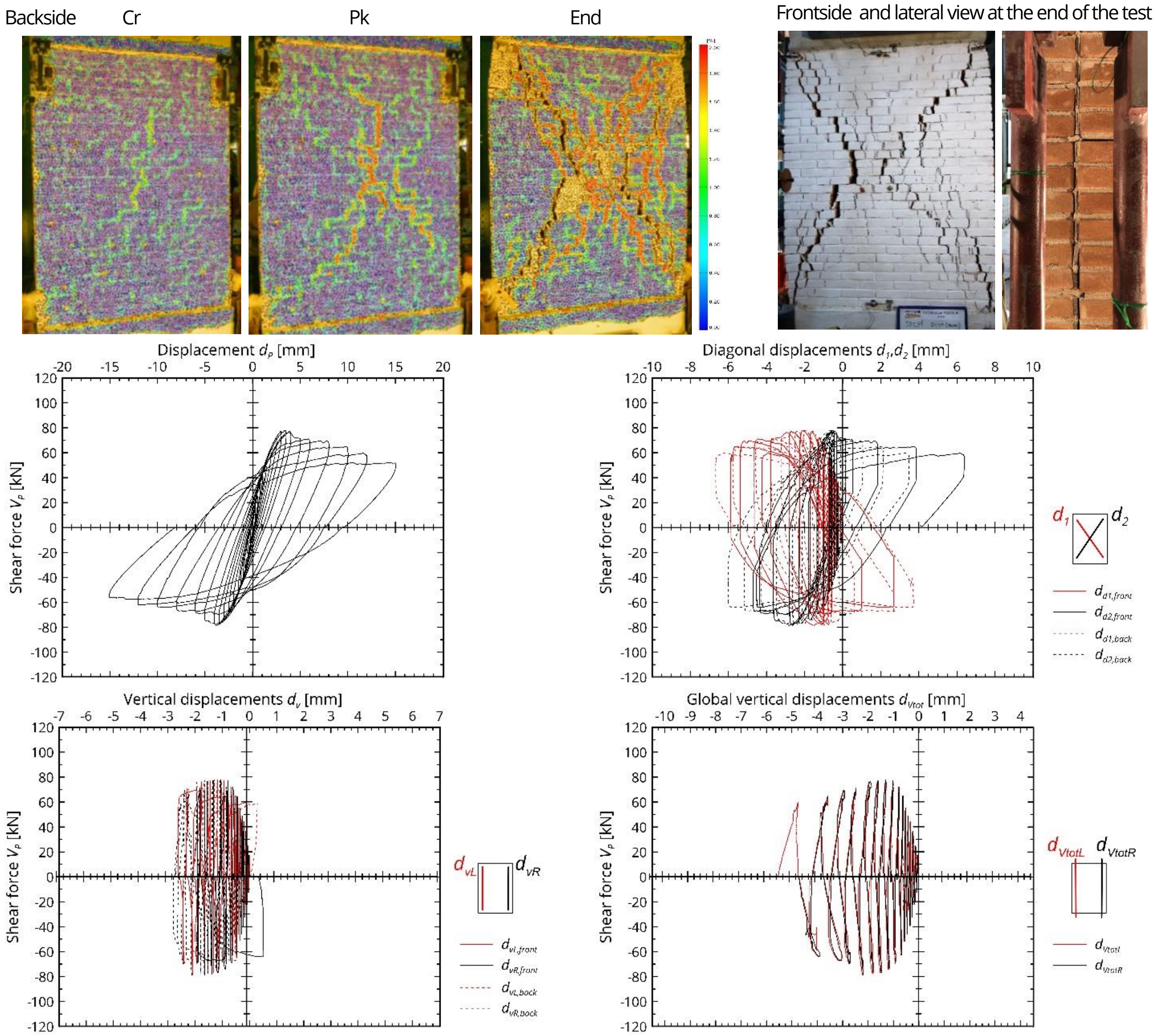

Fig. 3.2.7 Main results of test P-B2U.

- Test P-B2R-1 (Fig. 3.2.8)

The initial damage in the wall manifested as horizontal cracks at the top and bottom corners. With increasing load, the horizontal cracks propagated until peak resistance, when suddenly an inclined crack formed in the coating and also on the unstrengthened side. In the post-peak response, diagonal cracks in both the coating and the masonry were active and gradually propagated and the separation of the leaves was also observed. At the end of the test, the leaf with the coating diffusely separated and heavily leaned out. However, the transversal connectors prevented the overturning. The combination of several horizontal and inclined cracks in the coating reflected the combined activation of bending and shear mechanisms, as detected also by positive values achieved by both diagonal and vertical transducers.

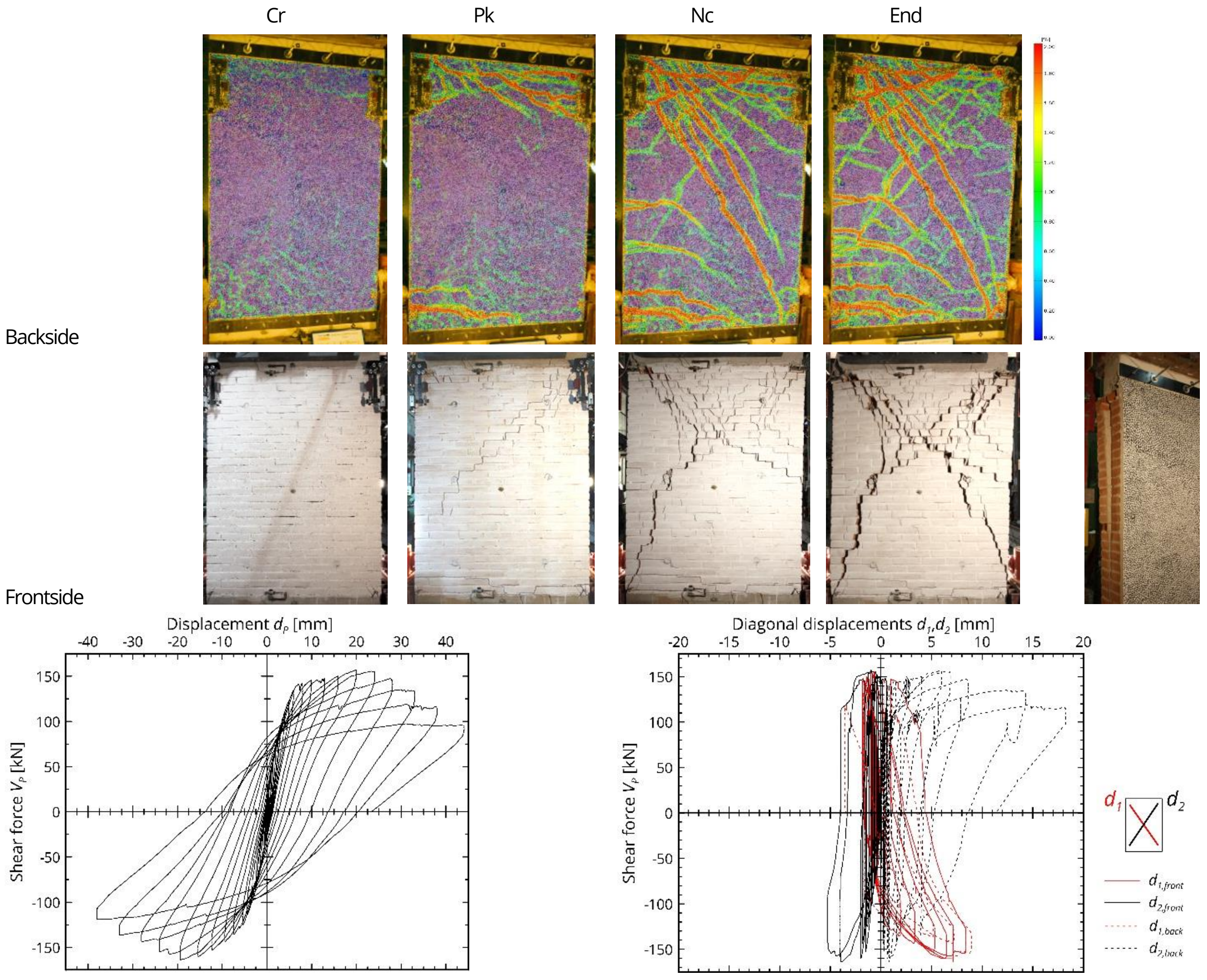

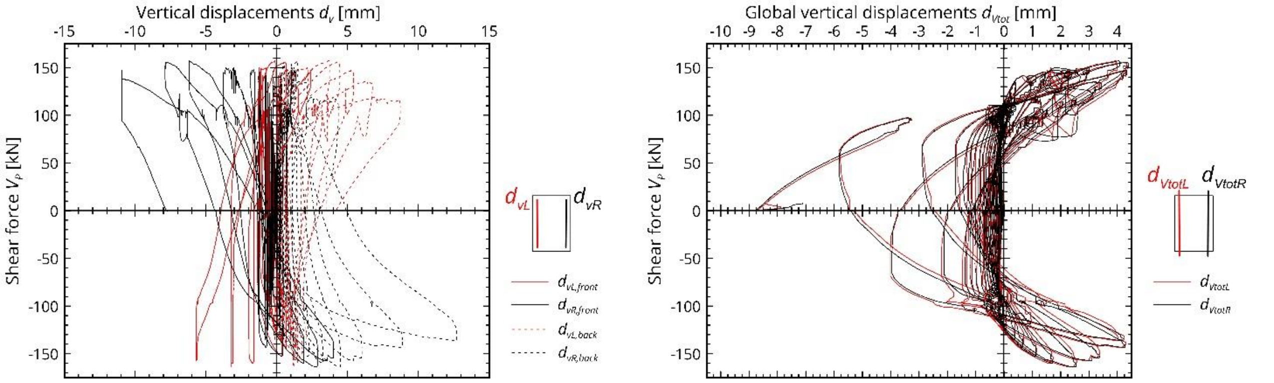

Fig. 3.2.8 Main results of test P-B2R-1.

- Test P-B2R-2 (Fig. 3.2.9)

The first damage was horizontal cracking at the base and top corners of the wall. This type of damage gradually propagated until peak resistance was reached. In post peak stage, the bending response remained dominant, but inclined cracks also appeared. The GFRP mesh fracture at the top of the wall was observed at collapse. Nor evident leaves separation of coating debonding were observed.

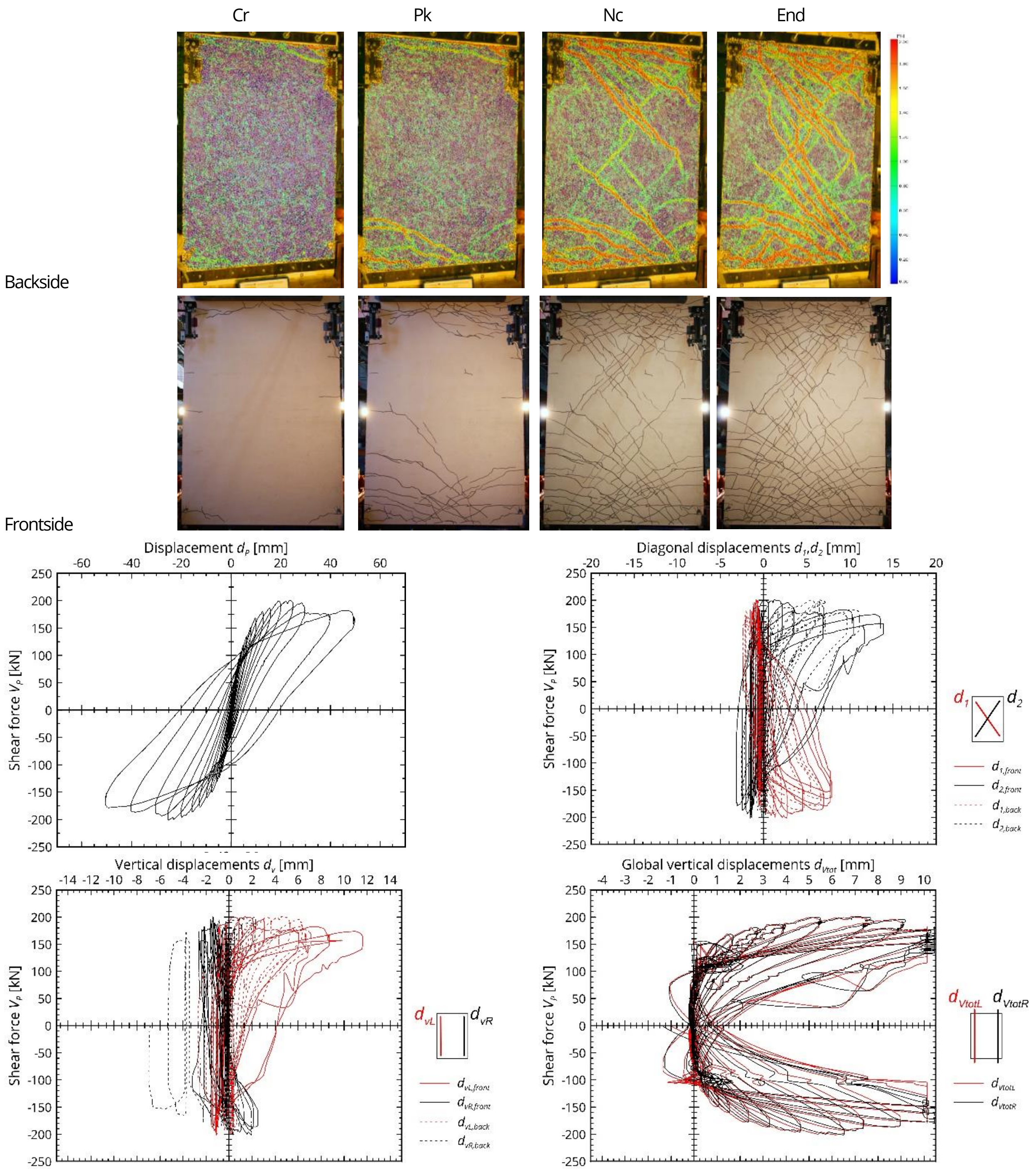

Fig. 3.2.9 Main results of test P-B2R-2.

- Test P-B1U (Fig. 3.2.10)

The first damage was horizontal cracks at the opposite corners, due to bending mechanism. Shortly after, a vertical crack at the centre of the wall opened. Approaching to the peak resistance, the vertical crack elongated at an angle towards the corners of the wall. Inclined cracking indicates shear response took over (as also detected by diagonal transducers) and continued until collapse was achieved.

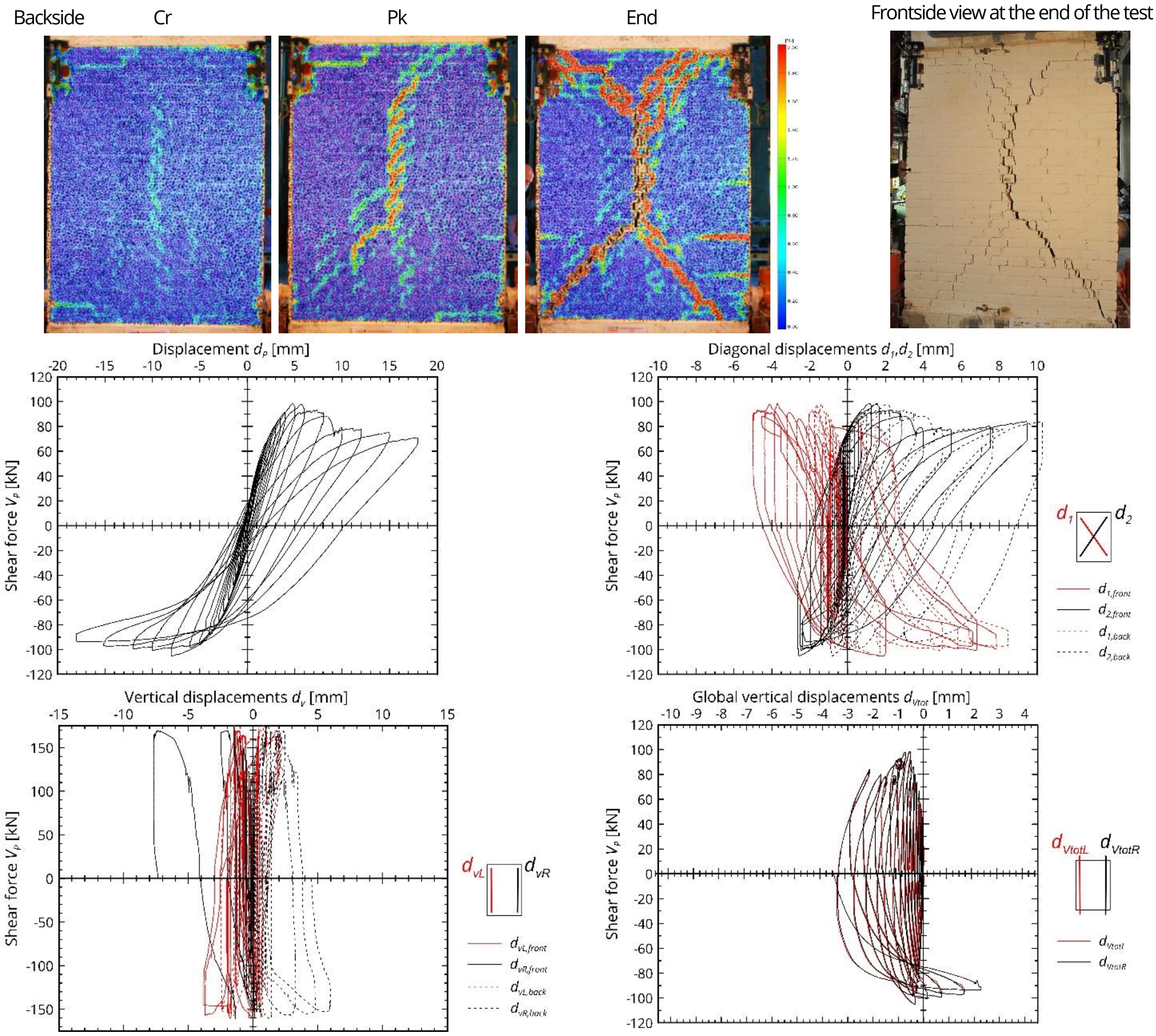

Fig. 3.2.10 Main results of test P-B1U.

- Test P-B1R-1 (Fig. 3.2.11)

The sample initially developed horizontal cracks on both the coating and the unstrengthened side. With increasing load, the horizontal cracks in the coating extended and propagated, but on the unstrengthened side some inclined cracks appeared in addition to the horizontal cracks, intersecting in the upper half of the wall. Shortly before peak resistance was reached, inclined cracks appeared also in the coating. After peak resistance, the inclined cracks were active and horizontal cracks barely activated. This continued until the end of the test. Although the inclined cracks were not exactly diagonal (from corner to corner), response was predominantly in shear.

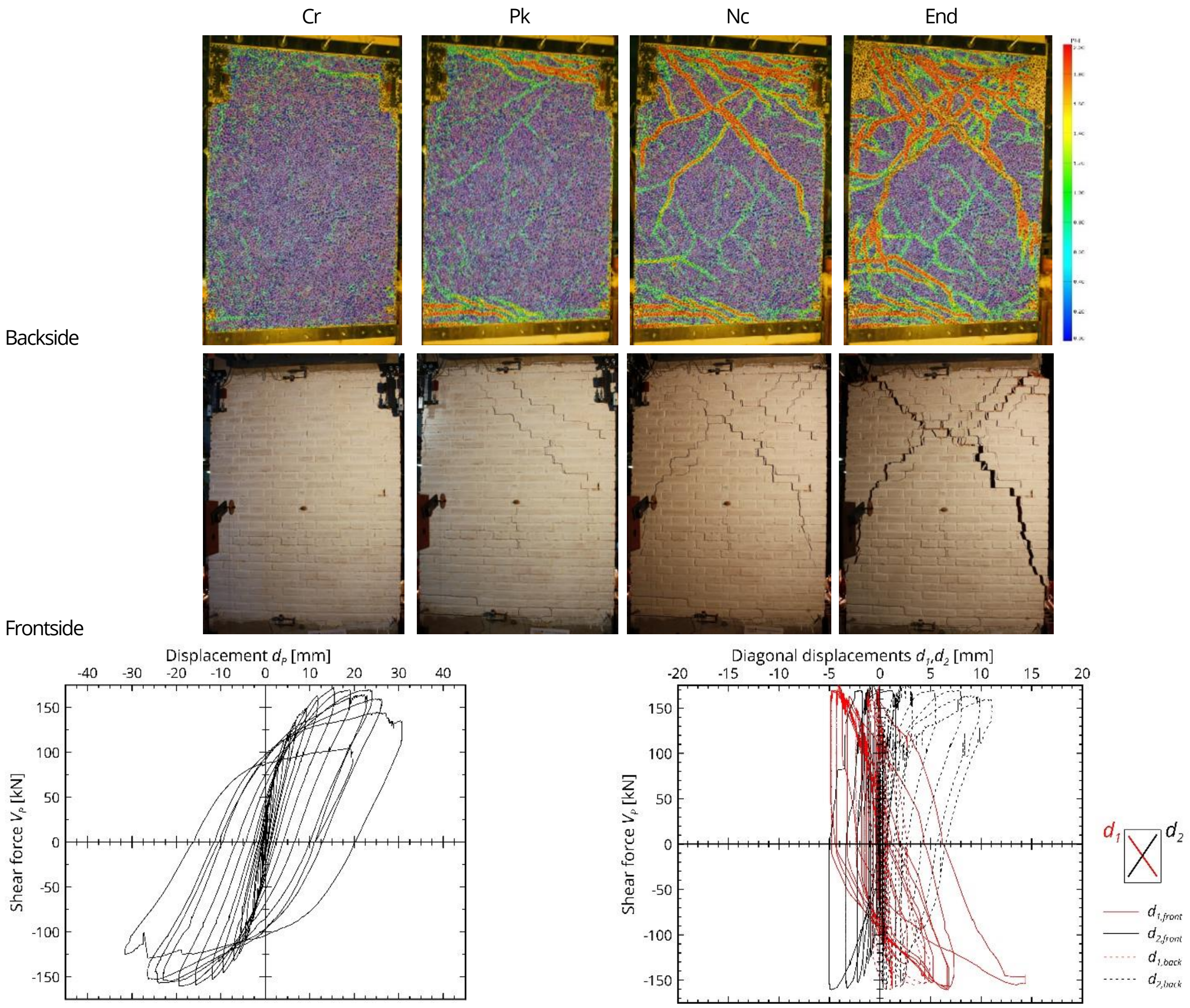

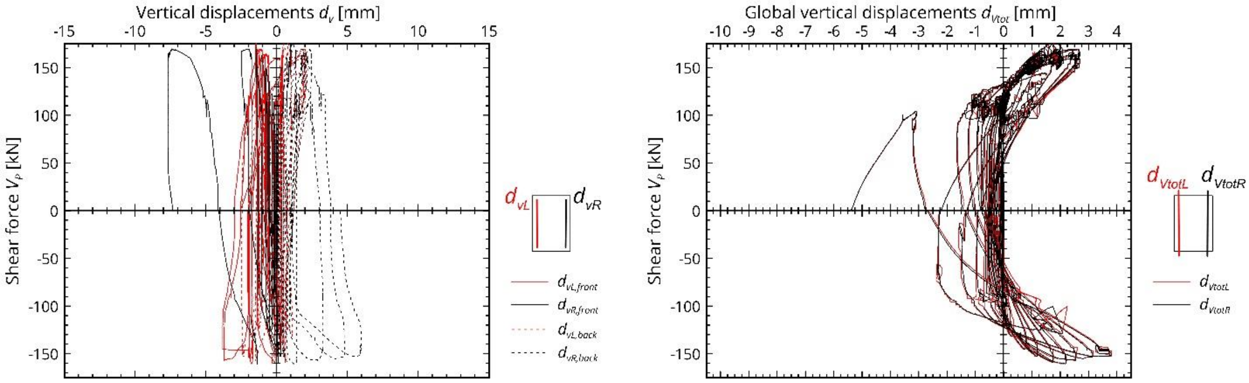

Fig. 3.2.11 Main results of test P-B1R-1.

The capacity curves comparison of unstrengthened and CRM strengthened pier samples is reported in Fig. 3.2.12. The values of V_P and d_P obtained from the eight experimental tests are summarized in Table 3.2 and in Fig. 3.2.13 for first cracking, peak load and end of the test (*Cr, Pk, End*).

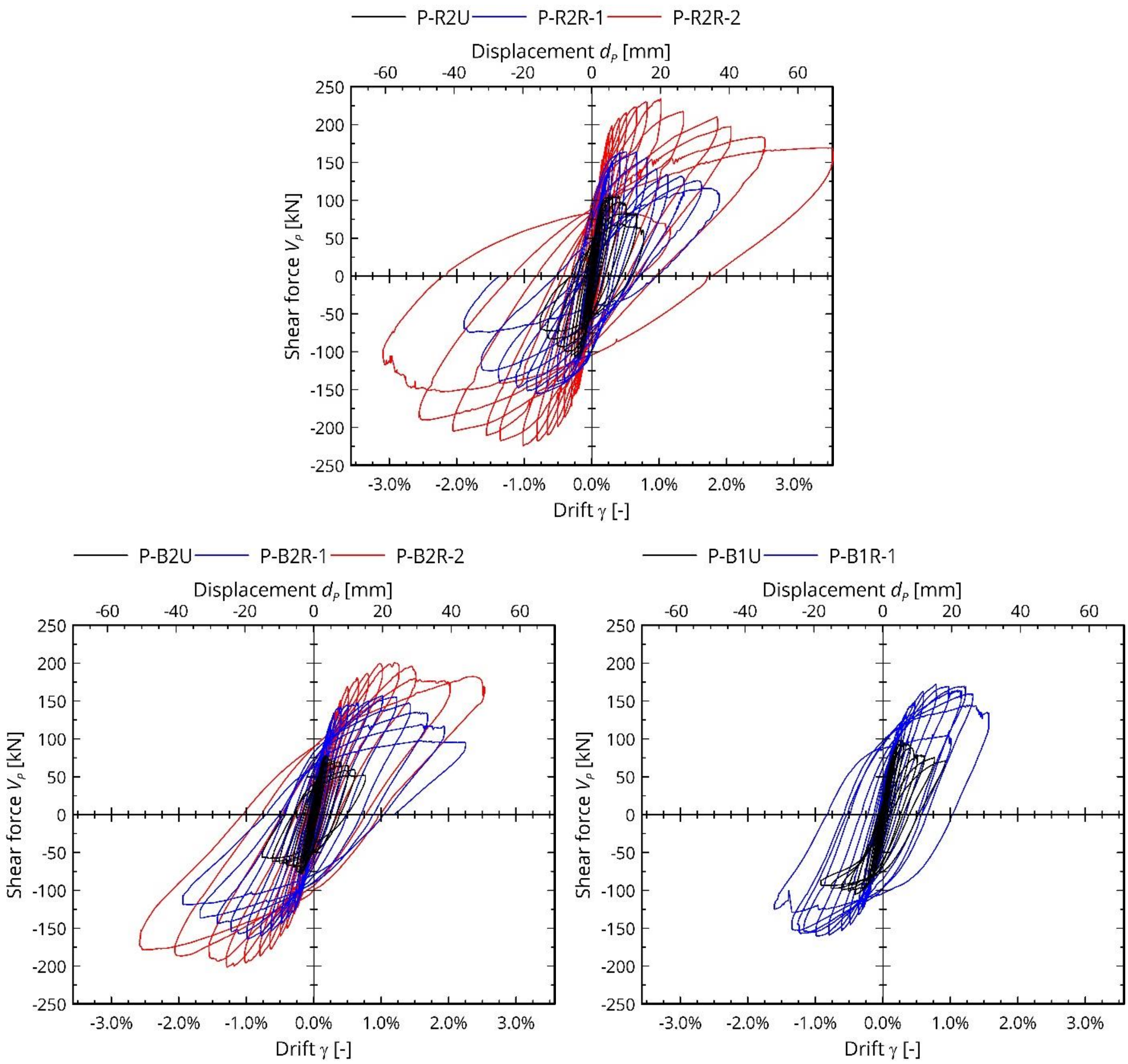

Fig. 3.2.12 Comparison of capacity curves of unstrengthened and CRM strengthened pier samples.

Table 3.2 Values of the lateral load (V_P) and horizontal displacement (d_P) measured in positive and negative loading directions, for the first cracking, peak load and end of the test.

	First cracking (*Cr*)		**Peak load (*Pk*)**		**End of test (*End*)**	
ID	V_P [kN]	d_P [mm]	V_P [kN]	d_P [mm]	V_P [kN]	d_P [mm]
P-R2U	83.2	2.0	106.8	4.9	74.7	13.0
	-84.8	-2.0	-108.8	-3.9	-76.2	-13.1
P-R2R-1	91.7	2.3	164.0	12.9	114.8	35.1
	-97.6	-2.5	-155.0	-16.2	-108.5	-32.2
P-R2R-2	157.2	3.7	234.3	19.8	164.0	68.0
	-157.6	-4.7	-224.5	-19.9	-157.1	-50.7
P-B2U	64.2	2.0	78.0	3.1	54.6	12.1
	-62.1	-2.0	-78.6	-4.0	-55.0	-15.0
P-B2R-1	98.0	3.2	157.0	20.1	109.9	38.1
	-95.0	-3.3	-164.0	-20.0	-114.8	-38.0
P-B2R-2	88.2	2.8	200.7	24.1	140.5	69.7
	-84.5	-2.6	-201.4	-25.1	-141.0	-70.4
P-B1U	55.7	1.3	98.5	4.8	68.9	18.1
	-63.4	-1.8	-105.3	-7.9	-73.7	-18.0
P-B1R-1	109.5	3.6	172.2	13.0	120.6	30.8
	-98.4	-3.0	-160.5	-16.1	-112.4	-31.6

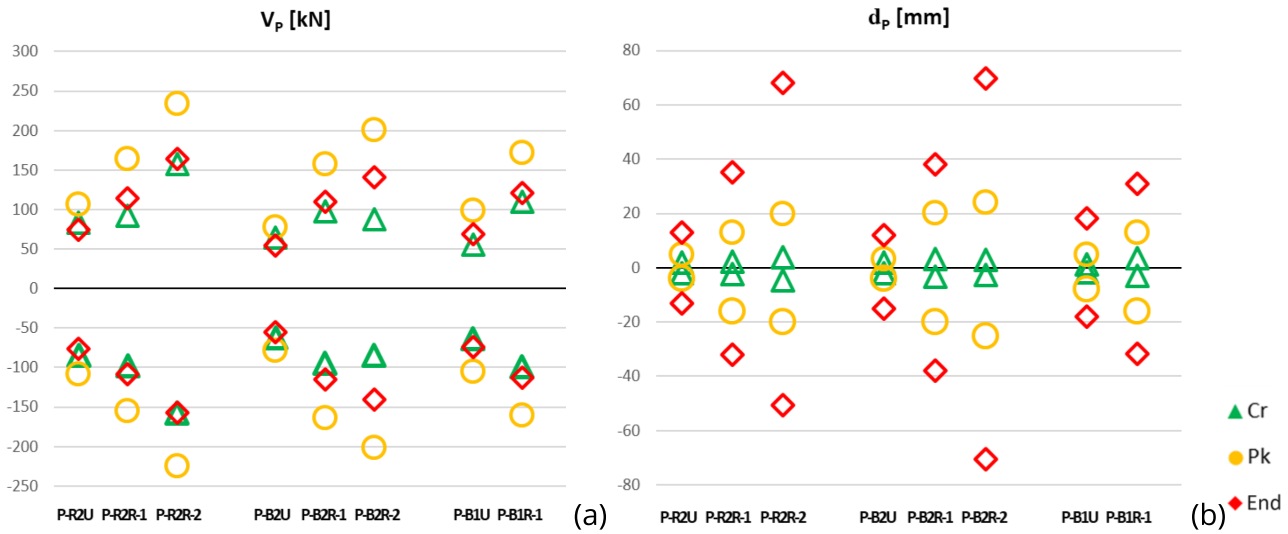

Fig. 3.2.13 Main test results of "P" samples: first cracking, peak and near collapse forces (a) and top horizontal displacements (b).

In all the unstrengthened masonry piers, the failure was governed by a pure diagonal cracking mechanism; the cracks had a stair-stepped trend and involved mainly the mortar joints (both head and bed joints). The stone masonry P-R2U attained to a mean peak load of 107.8 kN, quite similar to that of the single leaf brick masonry P-B1U (101.9 kN); a lower resistance was attained by the double leaf brick masonry P-B2U (78.3 kN). The ultimate displacement was quite high for P-B1U (18.1 mm), while lower for P-R2U and P-B2U (about 13.1-13.6 mm), due to the weak wythes connection. An evident leaf separation actually occurred in P-B2U, just after the peak load.
In the samples strengthened at one side only, the diagonal cracking mechanism was evidently detectable on the plain masonry side; diagonal cracks also occurred in the coating on the strengthened side, but in combination with horizontal and inclined cracks originating from the corners at the bottom and top of the pier, indicating also the activation of the in-plane bending mechanism. After reaching the peak load and approaching to collapse, leaf separation and coating debonding started to occur in P-R2R-1 and P-B2R-1 masonry and the coating debonding also activated in P-R2R-1. However, the presence of the transversal anchors contrasted the layer separation and overturning.
A very largely diffused crack pattern occurred in the two-sides strengthened samples, for the combined activation of diagonal cracking and bending mechanisms. The coating debonding (and the leaf separation in P-R2R-2) also activated when the collapse was incipient.

In the stone rubble masonry, the one-side CRM strengthening intervention led to an increase of the pier resistance of 1.48 times and determined an ultimate displacement 2.58 times higher in respect to the plain masonry. In case of strengthening at both sides, such increments resulted, respectively, 2.13 and 4.55 times. Actually, the one-side application provided values of strength and ultimate displacement almost in-between the plain and the two-sides strengthened configurations.
In the double leaf brick masonry, the peak resistance and the ultimate displacement of the one-side reinforced configuration were, respectively, 2.05 and 2.81 times those of the plain masonry. In case of strengthening at both sides, the increments were of 2.57 and 5.17 times. The one-side reinforcement applied on the single leaf brick masonry determined a pier resistance and ultimate displacement of 1.63 and 1.73 times those of the plain masonry.

The cyclic tests allow also to draw the trends of the piers cycle stiffness, K_P (evaluated as the slope of the peak-to-peak line within each loop of the V_P–d_P curve) by varying d_P (Fig. 3.2.14a). The stiffness degradation with increasing distortion shows an approximately power-law trend, with a softer degradation in the strengthened samples, in respect to the unstrengthened ones. At the end of the tests, the cycle stiffness degraded by about 90–95% of the initial value.
The cumulative input energy (E_{in}) and the dissipated hysteretic energy (E_{hys}) were quantified (Fig. 3.2.14b-c), as well as the E_{hys}/E_{in} ratios (Fig. 3.2.14d). E_{in} is the cumulative work to deform the sample from the beginning of the test to a specific target value of displacement d_P. For each loading cycle, it corresponds to the area under the positive and negative branches of the

hysteretic loop of the F_P-d_P graph. Similarly, the cumulative dissipated hysteretic energy E_{hys} is the sum of all the areas included in the hysteretic loops.
Finally, an estimation of the equivalent hysteretic damping with varying target displacement was performed (Fig. 3.2.14e), accordingly to the procedure reported in FEMA 440 [1].
In general, significantly higher input and dissipated cumulative energies resulted from the strengthened samples, in respect to the plain masonry (Table 3.3). The cumulative dissipated hysteretic energy for rubble stone, at the end of the tests, increased by 3.39 and 7.18 times compared to unstrengthened state, for piers P-R2R-1 and P-R2R-2, respectively. In case of two leaf brick masonry, the cumulative dissipated hysteretic energy was increased 5.46 and 8.73 times for piers P-B2R-1 and P-B2R-2, respectively. In case of single leaf brick masonry, the single sided application of coating increased the amount ofhysteretic cumulative dissipated hysteretic energy by a factor of 4.45.
Initially, the equivalent hysteretic damping, ξ_{hys}, ranged within 0.1-0.2, then experienced a rapid drop (more substantial in the strengthened samples) before increase again and reaching higher values (generally, up to 0.25-0.30).

Table 3.3 Cumulative input energy E_{in} and dissipated hysteresis E_{hys} at peak load (Pk) and at the end of the test (End), mean dissipated energy ratio in the cycles (E_{hys}/E_{in}). The ratios between strengthened and unstrengthened samples, for both E_{in} and E_{hys} are also calculated.

	Peak load (*Pk*)					**End of the test (*End*)**				
	E_{in} [J]	$E_{in,R}/E_{in,U}$ [-]	E_{hys} [J]	$E_{hys,R}/E_{hys,U}$ [-]	E_{hys}/E_{in} [-]	E_{in} [J]	$E_{in,R}/E_{in,U}$ [-]	E_{hys} [J]	$E_{hys,R}/E_{hys,U}$ [-]	E_{hys}/E_{in} [-]
P-R2U	2.84	1.00	2.02	1.00	0.71	11.95	1.00	9.62	1.00	0.81
P-R2R-1	16.33	5.74	12.21	6.06	0.75	44.65	3.74	32.59	3.39	0.73
P-R2R-2	27.06	9.52	14.44	7.16	0.53	101.13	8.46	69.10	7.18	0.68
P-B2U-1	2.02	1.00	1.14	1.00	0.56	8.04	1.00	6.11	1.00	0.76
P-B2R-1	18.92	9.39	9.51	8.31	0.50	52.41	6.52	33.36	5.46	0.64
P-B2R-2	27.01	13.40	11.42	9.98	0.42	87.72	10.91	53.32	8.73	0.61
P-B1U-1	4.85	1.00	2.43	1.00	0.50	13.59	1.00	7.04	1.00	0.52
P-B1R-1	14.79	3.05	7.05	2.91	0.48	47.58	3.50	31.33	4.45	0.66

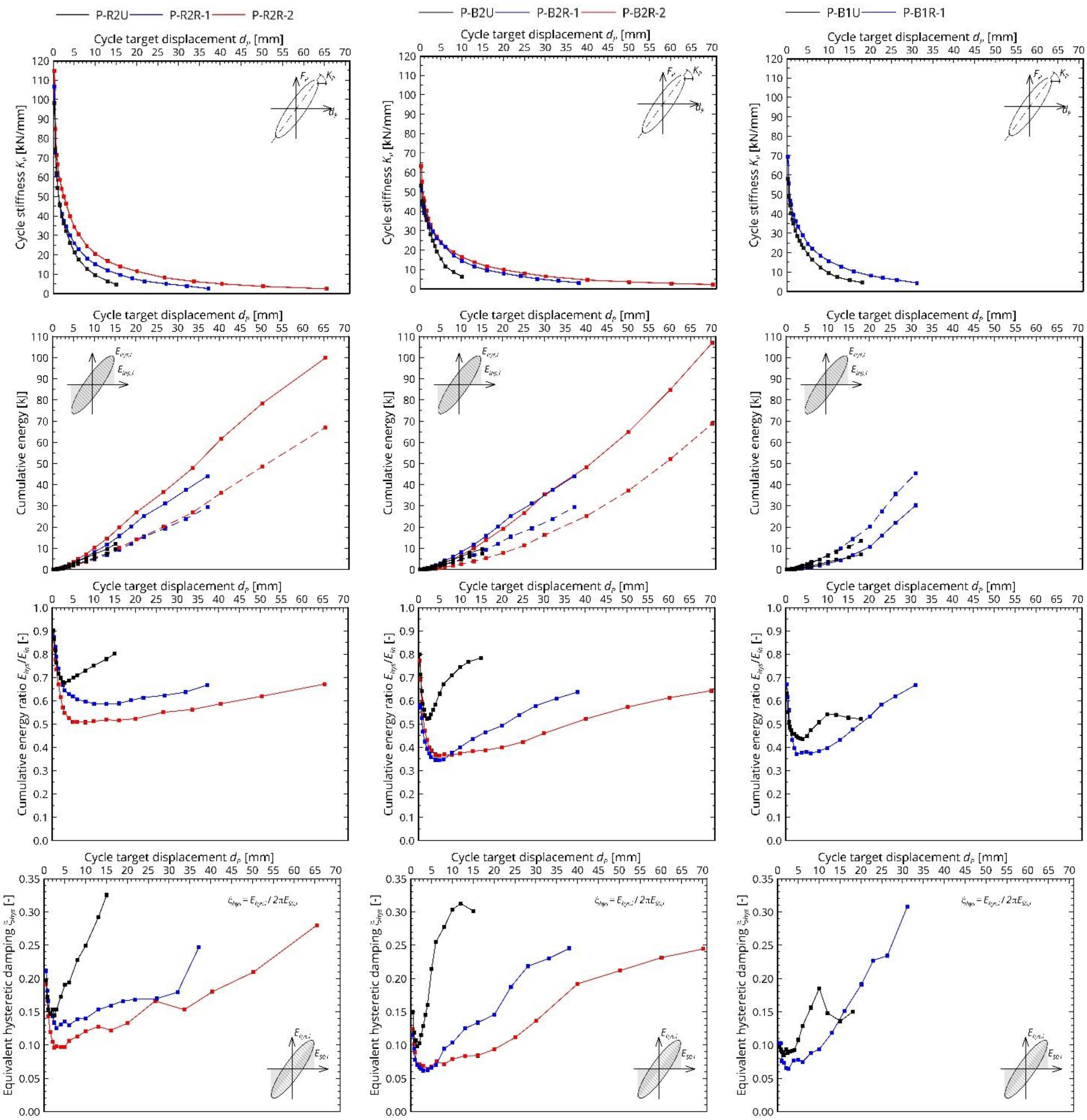

Fig. 3.2.14. Piers stiffness and energy characteristics, varying the cycle target displacement d_P.

3.2.2. Analytic model

Symbols:

t	masonry pier thickness
b	masonry pier width
l	masonry pier height (i.e. "effective length")
E_m	masonry Young's modulus
G_m	masonry shear modulus (~1/3E_m)
i	number of CRM-strengthened sides (1-2)
t_c	plaster nominal thickness
E_c	plaster Young's modulus
G_c	plaster shear modulus (~0.4E_c)
η	coefficient related to the pier static scheme (e.g. 3 for cantilever, 12 for shear type)
I	second bending moment of the uncracked pier cross section ($tb^3/12$)
σ_0	mean vertical compressive stress on the pier
τ_0	equivalent masonry shear strength for σ_0 = 0 (for "Turnšek and Čačovič" formula)
β	pier slenderness factor ($1.0 \leq \beta = l/b \leq 1.5$)
χ	effectiveness reduction factor (=1 for CRM at both-sides, ≤1 at one side)
γ	model coefficient (=2)
A_G	net cross section of a GFRP wire
T_G	mean tensile resistance of a GFRP wire
s	GFRP mesh grid pitch
l_f	CRM effective length (=l, but ≤b)
$\varepsilon_{lim,G}$	limit tensile strain of GFRP
E_G	GFRP Young's modulus
f_m	masonry compressive strength
α	coefficient of bending moment distribution (e.g. 1 for cantilever, 2 for shear type)
x	depth of the neutral axis of the cracked cross-section

To schematize analytically, in a simplified way, the in-plane lateral performances of masonry piers, an elastic-plastic behaviour can be considered (Fig. 3.2.15). To estimate the stiffness, resistance and ultimate displacement capacities, well-known correlations available in the literature can be considered for the unstrengthened masonry. For CRM strengthened masonry, the correlations need to be adjusted to account for the CRM contribution.

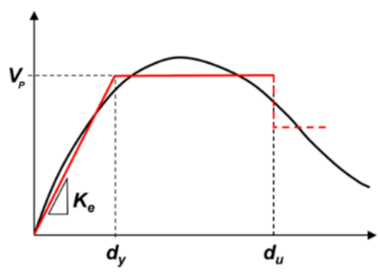

Fig. 3.2.15 Generic, simplified elastic-plastic schematization of the in-plane lateral performances of masonry piers (red line), in comparison with actual performances (black line).

To evaluate the pier stiffness, K_e, both the flexural and shear deformability shall be accounted, as indicated in Eq.(3.1). In case of CRM strengthened masonry, equivalent Young and shear moduli shall be considered, evaluating the average values between masonry and mortar coating, weighted on the respective thickness.

$$K_e = \frac{1}{\frac{l^3}{\eta I E} + \frac{1.2 l}{G b t}} \qquad (3.1)$$

For the evaluation of the pier's in-plane lateral resistance, V_P, the weakest mechanism between shear failure (due to diagonal cracking), $V_{P,d}$, and bending, $V_{P,f}$, is considered:

$$V_P = \min(V_{P,d}; V_{P,f}) \qquad (3.2)$$

The typical crack patterns that occur during seismic events are illustrated in Fig. 3.2.16. For these mechanisms to activate, the diagonal masonry strut should not prematurely fail in compression:

$$V_P \le 0.25 \cdot b \cdot t \cdot f_m \qquad (3.3)$$

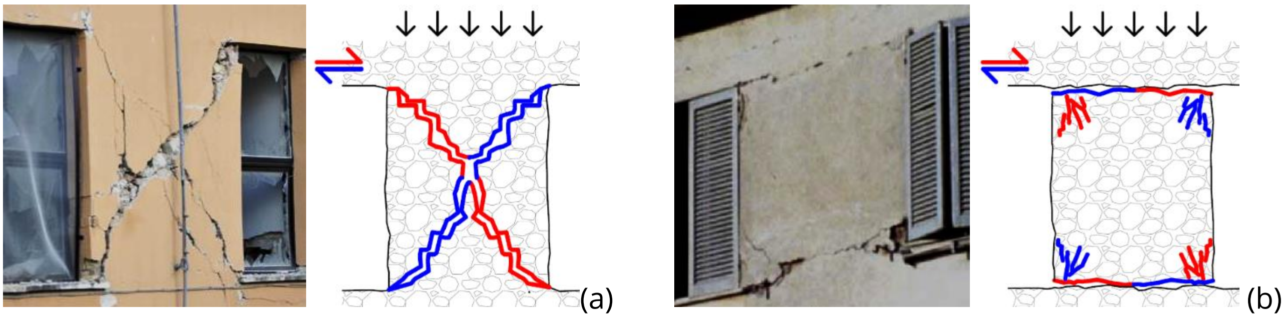

Fig. 3.2.16 Typical in-plane failure mechanism of masonry piers: diagonal cracking (a) and bending (b).

For the unstrengthened masonry piers (suffix URM), different resistant models can be found in the literature to estimate $V_{P,d(URM)}$. For example, the well-known "Turnšek and Čačovič" correlation, suitable for both regular and irregular masonry, can be applied (according to C8.7.1.16 in MIT 2019 [2]):

$$V_{P,d(URM)} = \frac{1.5\tau_0}{\beta} b \cdot t \sqrt{1 + \frac{\sigma_o}{1.5\,\tau_0}} \qquad (3.4)$$

The in-plane bending resistance of the unreinforced masonry piers is mainly due to the masonry compressive resistance and the stabilizing effect of the vertical loads ([7.8.2] in MIT 2018 [3]):

$$V_{P,f(URM)} = \frac{\alpha\, M_{P(URM)}}{l} = \frac{\alpha}{l} \frac{\sigma_o b^2 t}{2} \left(1 - \frac{\sigma_o}{0.85 f_m}\right) \qquad (3.5)$$

Both mechanisms benefit from the contribution of the CRM system, as the fiber-based composite material (the mesh wires), crossing both the diagonal and the horizontal cracks,

limits their opening, fostering a wider stress diffusion. However, to be effective against the bending failure, the CRM system has to be sufficiently extended beyond the pier end sections.
Due to the lack of specific correlations for the evaluation of the resistance of CRM strengthened masonry pier (suffix CRM), reference is herein made to CNR-DT 215/2018 [4], an Italian guideline available for FRCM strengthening systems, that have several similarities with CRM ones.
According to [4], the contribution given by the wires along the loading direction crossing the diagonal crack shall be added to that of the unstrengthened masonry:

$$V_{P,d(CRM)} = V_{P,d(URM)} + \chi \frac{1}{\gamma} \cdot i \cdot \frac{A_G}{s} \cdot l_f \cdot \varepsilon_{\lim,G} \cdot E_G \quad (3.6)$$

Note that, if the tensile failure of the fibers is attained, the factor $A_G \cdot \varepsilon_{\lim,G} \cdot E_G$ corresponds to the tensile resistance of a single wire, T_G.
For the bending failure mechanism of the CRM strengthened masonry pier, the tensile-resistant contribution of the vertical wires crossing the horizontal cracks at the end sections shall be accounted:

$$V_{P,f(CRM)} = \frac{\alpha M_{P(CRM)}}{l} = \frac{\alpha}{l}\left[0.8x \cdot f_m \cdot t\left(\frac{b}{2} - 0.4x\right) + \chi \frac{i \cdot A_G \cdot \varepsilon_{\lim,G} \cdot E_G}{s} \cdot \frac{(b-x)}{2}\left(\frac{b}{6} + \frac{x}{3}\right)\right] \quad (3.7)$$

$$\text{with} \quad x = b \cdot t\left(\sigma_0 + \chi \frac{i\, A_G \cdot \varepsilon_{\lim,G} \cdot E_G}{2s \cdot t}\right) \Big/ \left(0.8 \cdot f_m \cdot t + \chi \frac{i \cdot A_G \cdot \varepsilon_{\lim,G} \cdot E_G}{2s}\right).$$

Basically, $M_{P(CRM)}$ shall be evaluated by analysing a reinforced section subjected to combined compression and bending in cracked conditions, assuming conservation of plane sections, perfect bond among materials, masonry cracked in tension and plastic in compression, fibre mesh with linear-elastic behaviour in tension until the limit strain.
It is observed that the plaster contribution is neglected in both mechanisms. It is also worth noting that the introduction of effective transversal connectors in multiple-leaves masonry could be grossly considered by increasing the masonry shear strength, τ_0. Appropriate coefficients (range 1.2-1.5, depending on masonry type) are provided in C8.5.II of MIT 2019 [2].

The ultimate displacement capacity of the masonry pier, d_{Pu}, is evaluated on the basis of the chord rotation limits at the pier extremities, θ_{Pu}. For unstrengthened masonry, the values provided in C8.7.1.3.1.1 of MIT 2019 [2] can be applied – Eq. (3.8).

$$\theta_{Pu(URM)} = \begin{cases} 0.005 & if \;\; V_{P,d(URM)} < V_{P,f(URM)} \\ 0.010 & if \;\; V_{P,d(URM)} \geq V_{P,f(URM)} \end{cases} \quad (3.8)$$

For CRM masonry, in the lack of any guidance, doubled values could be considered, based on experimental evidences – Eq. (3.9).

$$\theta_{Pu(CRM)} = \begin{cases} 0.010 & if \;\; V_{P,d(CRM)} < V_{P,f(CRM)} \\ 0.020 & if \;\; V_{P,d(CRM)} \geq V_{P,f(CRM)} \end{cases} \quad (3.9)$$

3.2.3. Application and validation

The analytical model described in §3.2.2 is adopted to evaluate the lateral performances of the CONSTRAIN experimental tests on the pier samples resumed in §3.2.1.
The values of the unstrengthened masonry shear strength (τ_0) considered in the formulations are calculated from the CONSTRAIN experimental tests obtained for the unstrengthened pier samples (P-R2U, P-B2U and P-B2U in §3.2.1). In particular, since the diagonal cracking failure was attained in all the unstrengthened samples, Eq. (3.4) is solved for τ_0. For the resistance $V_{P,d(URM)}$, a bi-linearization of the backbone capacity curves is performed (according to C7.3.4.2 of MIT 2018 [3]) and the mean plastic value between positive and negative loading directions is considered.
For the Young's modulus, E_m, and the compressive strength, f_m, a preliminary estimation was done on the basis of Tab.C8.5.I of MIT 2019 [2], by performing a linear interpolation within the provided ranges for the different masonry types, starting from the values of shear strength τ_0. Actually, for the rubble stone sample, the values estimated by this procedure resulted slightly higher than the results of the monotonic compressive tests on masonry wallets (Appendix A.). Therefore, those experimental outcomes were assumed as consistent and representative and were thus prudentially set as input parameters for masonry R2. Conversely, for the solid brick masonry (both B2 and B1), the results of the monotonic compressive tests on masonry wallets (Appendix A.) provided values of both E_m and f_m significantly higher than Tab.C8.5.I. In this case, this latter calculated values were set as input parameters, since prudentially believed to be more representative for a masonry that is subjected to cyclic loading and whose orientation of principal compressive stresses may from the vertical.
The main results are summarized in Fig. 3.2.17 and compared graphically with the experimental capacity curves. It is worth to note that the elastic deformability of the apparatus ($1/K_{add,P}$, experimentally measured as 1/56000 mm/N) is added to that of the samples, as it is not negligible.

Main data										
b	[mm]	1500		σ_0	[MPa]	0.5		η	[-]	12
l	[mm]	1960		A_G	[mm2]	3.8		α	[-]	2
t_c	[mm]	30		T_G	[kN]	5.11				
E_c	[GPa]	10		s	[mm]	66				
G_c	[GPa]	4		l_f	[mm]	1500				

		P-R2U	P-R2R-1	P-R2R-2
t	[mm]	350	350	350
f_m	[MPa]	2.48	2.48	2.48
τ_0	[MPa]	0.071	0.071	0.071
i	[-]	-	1	2
χ	[-]	-	1.0	1.0
E	[MPa]	1074.2	1931.3	2788.5
G	[MPa]	358.1	700.9	1043.8
K_e	[N/mm]	54214	103178	152022
$K_{add,P}$	[N/mm]	56000	56000	56000
x	[mm]	-	437.3	490.6
M_P	[kNm]	150.2	190.9	221.0
$V_{P,f}$	[kN]	153.2	194.8	225.5
$V_{P,d}$	[kN]	102.2	160.2	218.3
V_P	**[kN]**	**102.2**	**160.2**	**218.3**
Mode	[-]	Shear	Shear	Shear*
$d_{P,e}$	**[mm]**	**3.71**	**4.41**	**5.33**
$d_{P,u}$	**[mm]**	**11.6**	**21.4**	**21.4 (41.0)**

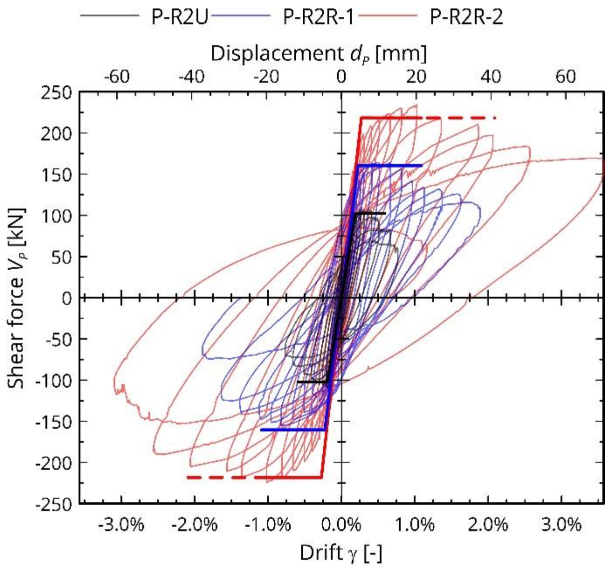

(*) since $V_{P,f}$ and $V_{P,d}$ are vely close, a combined shear/bending failure is expected, thus $d_{P,u}$ could likely reach values related to flexure.

		P-B2U	P-B2R-1	P-B2R-2
t	[mm]	250	250	250
f_m	[MPa]	2.98	2.98	2.98
τ_0	[MPa] (*)	0.068	0.068x1.3	0.068x1.3
i	[-]	-	1	2
χ	[-]	-	1.0	1.0
E	[MPa]	1335.7	2535.7	3735.7
G	[MPa]	445.2	925.2	1405.2
K_e	[N/mm]	48150	97104	145939
$K_{add,P}$	[N/mm]	56000	56000	56000
x	[mm]	-	386.4	450.3
M_P	[kNm]	112.9	153.6	185.7
$V_{P,f}$	[kN]	115.2	156.8	189.5
$V_{P,d}$	[kN]	71.2	141.3	199.3
V_P	[kN]	71.2	141.3	199.3
Mode	**[kN]**	**71.2**	**141.3**	**189.5**
$d_{P,e}$	[-]	Shear	Shear**	Bending
$d_{P,u}$	**[mm]**	**2.75**	**3.98**	**4.68**
M_P	**[mm]**	**11.1**	**21.1 (40.7)**	**40.7**

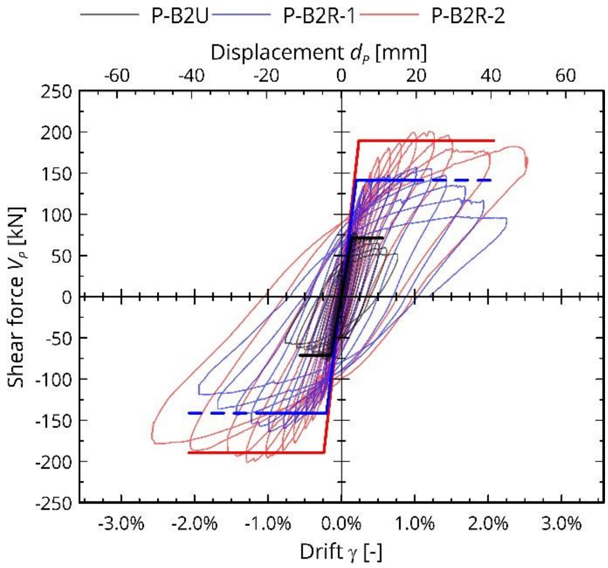

(*) 1.3 is the amplification factor of the shear strength in multiple-leaves solid brick masonry, to account for the benefits of effective transversal connectors (since leaves separation actually occurred in P-B2U, but not in P-B2R-1 and P-B2R-2).

(**) since $V_{P,f}$ and $V_{P,d}$ are very close, a combined shear/bending failure is expected, thus $d_{P,u}$ could likely reach values related to flexure.

		P-B1U	P-B1R-1
t	[mm]	250	250
f_m	[MPa]	3.84	3.84
τ_0	[MPa]	0.108	0.108
i	[-]	-	1
χ	[-]	-	1.0
E	[MPa]	1638.6	2838.6
G	[MPa]	546.2	1026.2
K_e	[N/mm]	59069	108041
$K_{add,P}$	[N/mm]	56000	56000
x	[mm]	-	304.2
$M_{P(CRM)}$	[kNm]	119.1	163.2
$V_{P,f(CRM)}$	[kN]	121.5	166.5
$V_{P,d(URM)}$	[kN]	94.2	94.2
$V_{P,d(CRM)}$	[kN]	-	152.3
$V_{P(CRM)}$	**[kN]**	**94.2**	**152.3**
Mode	[-]	Shear	Shear
$d_{P,e(CRM)}$	**[mm]**	**3.28**	**4.13**
$d_{P,u(CRM)}$	**[mm]**	**11.5**	**21.3**

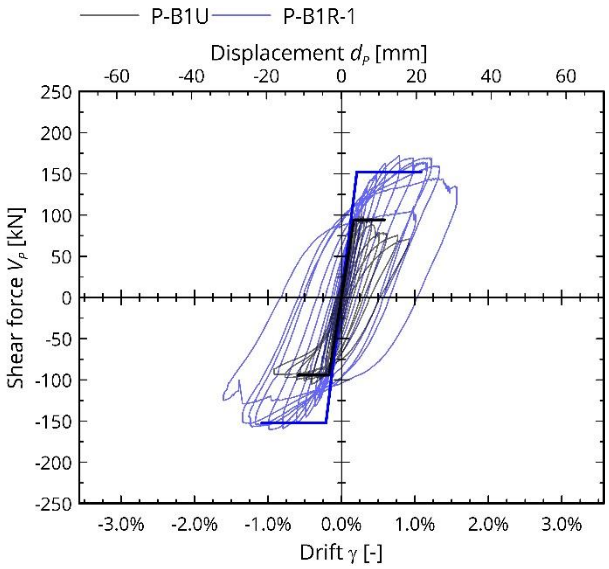

Fig. 3.2.17 Analytic results concerning the masonry pier samples and comparison with the experimental behaviour

3.3. In-plane behaviour of spandrels

3.3.1. Summary and analysis of the experimental results

The samples consisted of "H"-shape masonry panels (Fig. 3.3.1) aimed at recreating the spandrel area. To facilitate a uniform load distribution in testing, r.c. beams were created at the base and at the top of each masonry column.

Three different masonry types were considered: R2, B2 and B1 (Appendix A.). In the rubble stone samples, a timber lintel (2 beams, cross section 170x170 mm^2), indenting in each lateral column for 150 mm, was introduced under the spandrel, to reproduce the typical arrangements in historical stone buildings. Differently, in the solid brick samples, a masonry jack arch was created at the spandrel intrados, with couples of bricks arranged alternatively as headers or stretchers (height 250 mm).

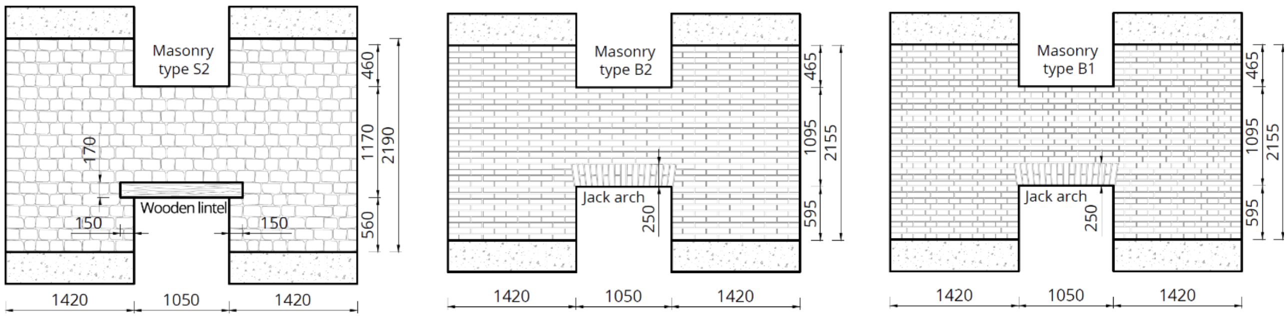

Fig. 3.3.1 Main geometric characteristics of the spandrel samples.

Four "H"-shape panels were built and tested firstly unstrengthened, up to a damage level close to the ultimate. Then they were repaired, retrofitted and tested again, up to a near-collapse condition (Table 3.4). The positioning of the GFRP connectors and of GFRP connectors combined with artificial diatones is schematized in Fig. 3.3.2.

Table 3.4: Summary of the CONSTRAIN experimental tests on spandrels.

Sample ID	Masonry type	Strengthening system	Connectors
S-R2U-1	R2	/	/
S-R2R-1	R2	CRM on one-side	GFRP + diatons, 1 side
S-R2U2	R2	/	/
S-R2R-2	R2	CRM on two-sides	GFRP, passing-through
S-B2U	B2	/	/
S-B2R	B2	CRM on one-side	GFRP + diatons, 1 side
S-B1U	B1	/	/
S-B1R	B1	CRM on one-side	GFRP, 1 side

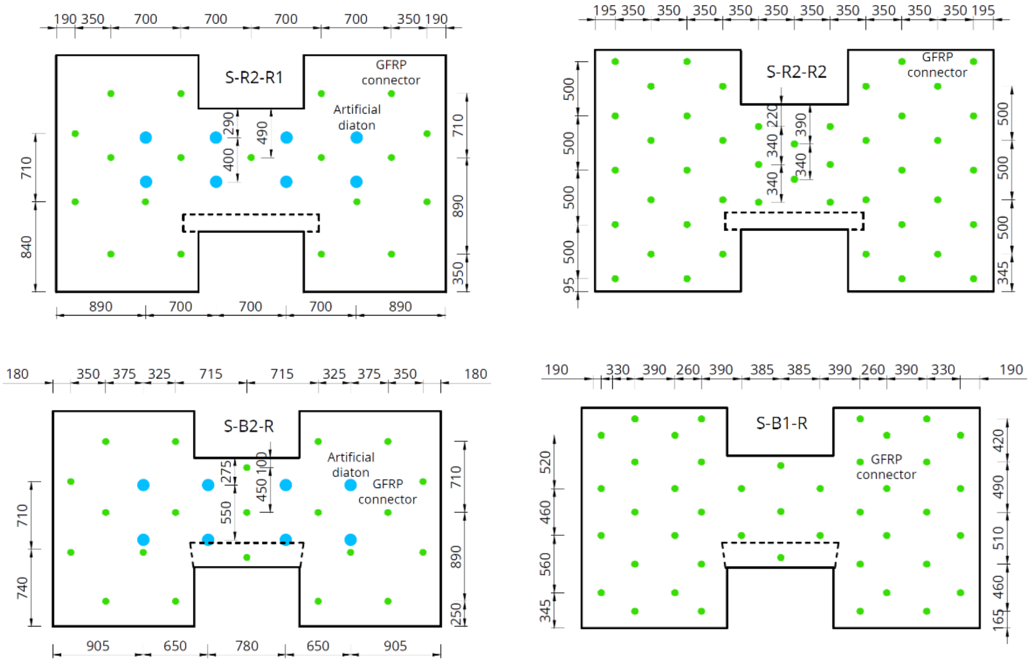

Fig. 3.3.2 Positioning of the connectors in CRM strengthened spandrel samples.

The test apparatus consisted of two independent horizontal steel beams, placed on support knuckle joints (equipped with load cells). The joints allowed the possibility of carrying loads in both compression and tension. Both joints were rotational; in addition, the right joint, allowed horizontal translations. Each external wall column of the H-shape masonry sample was positioned on one of the steel beams, vertically centered with the knuckle joint. Two servo-hydraulic actuators ortiented vertically were attached to the free, external ends of the steel beams and locked on independent steel frames. Four hydraulic pistons were installed on the columns to apply an axial compressive load. Each pistons was contrasted at the top by steel elements connected to the steel beams at the base by means of threaded rods. The four pistons were connected in parallel and introduced a constant force (correspondent to an axial stress level of about 0.33 MPa on the masonry columns). During the tests, the two external actuators moved at the same speed in opposite directions, which means that the two masonry piers rotated with the same direction and intensity. This caused shear and bending in the spandrel. The load was applied cyclically in the positive (clockwise rotation of the beams) and negative directions (anti-clockwise rotation), gradually increasing the target amplitude and performing three repetitions for each.

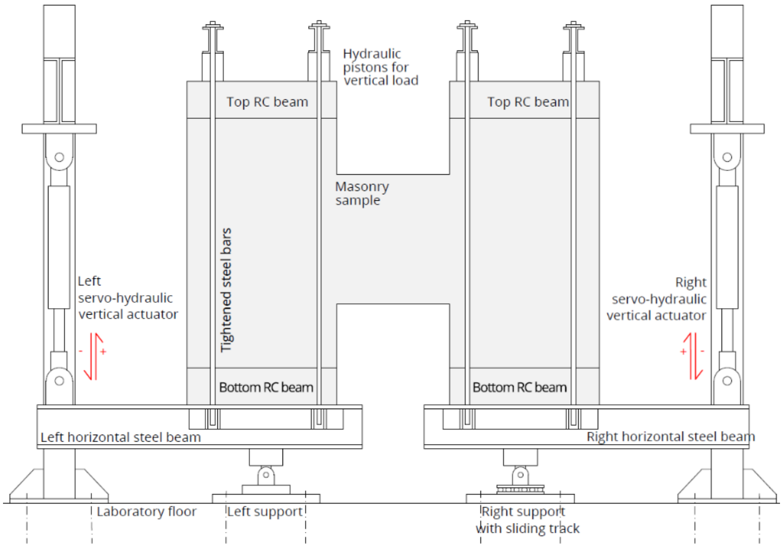

Fig. 3.3.3 Schematization of the test setup for spandrels.

The behaviour of each sample is described in the following, reporting also monitored loads and displacements and evolution of the crack pattern (surveyed at the front side by means of a Digital Image Correlation system). The main results are then summarized and compared.

The global behaviour of the spandrels is described in terms of capacity curves, representing the shear load, V_S, varying the vertical distortion d_S. The shear load V_S was obtained from the vertical translation equilibrium of the external vertical forces acting on the left half (as well as right half) of the sample, i.e. load applied by the outer actuator and the reaction at the support. The distortion d_S was calculated by using the following equation:

$$d_S = \left(\delta_{V,r} - \delta_{V,l}\right) \cdot \left(\frac{b_S}{2} + \frac{b_P}{2}\right) \Big/ \left(\frac{b_P}{2}\right), \qquad (3.10)$$

where b_S and b_P are the spandrel and the pier widths, respectively and δ_V the vertical displacements in correspondance on the inner corners of the two masonry columns (right – *r*, and left – *l*). The spandrel drift γ_S was determined by dividing d_S by the spandrel's length.

In addition to the distortion, the horizontal sliding of the right support (d_H) was monitored during the tests.

According to the typical in-plane failure mechanisms of historic masonry elements, two groups of cracks were generally expected: mainly vertical cracks at the spandrels ends, related to in-plane bending failure, and diagonal cracks within the spandrels, indicative of an in-plane diagonal shear mechanism. For monitoring such occurrances, the DIC system was employed to evaluate the trends of the equivalent horizontal strains at the top and the bottom of the spandrels (ε_{top} and ε_{bot}, respectively) and of the equivalent strains across the spandrels diagonals (ε_{d1} and ε_{d2}, respectively). Strains ε_{top} and ε_{bot} were calculated on a base length of about 1780 mm; ε_{d1} and ε_{d2} were calculated on a base length of about 700 mm centred in the spandrel area. In general, the monitored strains were positive (tensile strains), regardless of the loading direction, consistently with the formation of the cracks. Not-negligible residual strains were expected, as long as damage progressed.

- Test S-R2U-1 (Fig. 3.3.4)

The first cracking appeared at the spandrels opposite corners. The cracks gradually expanded, following the mortar joints in an almost vertical pattern until they spanned the entire height. Similar cracks emerged on both sides of the sample, spanning the full thickness of the wall. A significant drop in stiffness then occurred, and the cracking evolved asymmetrically. When loaded in the positive direction, damage was concentrated in the two vertical cracks at the spandrel ends. In contrast, a diagonal crack appeared when loaded in the negative direction, originating from the top-right corner, where the damage was primarily focused. Despite these differences, the load decrease was gradual in both cases. A mixed failure mode, involving both bending and shear, was observed. The horizontal displacements at the right support noticed the right pier pulled away from the left one; residual slip significantly increased with the number of load cycles. The horizontal strains at top and bottom resulted almost comparable, while diagonal strains were not, due to the activation of the inclined crack along one diagonal only.

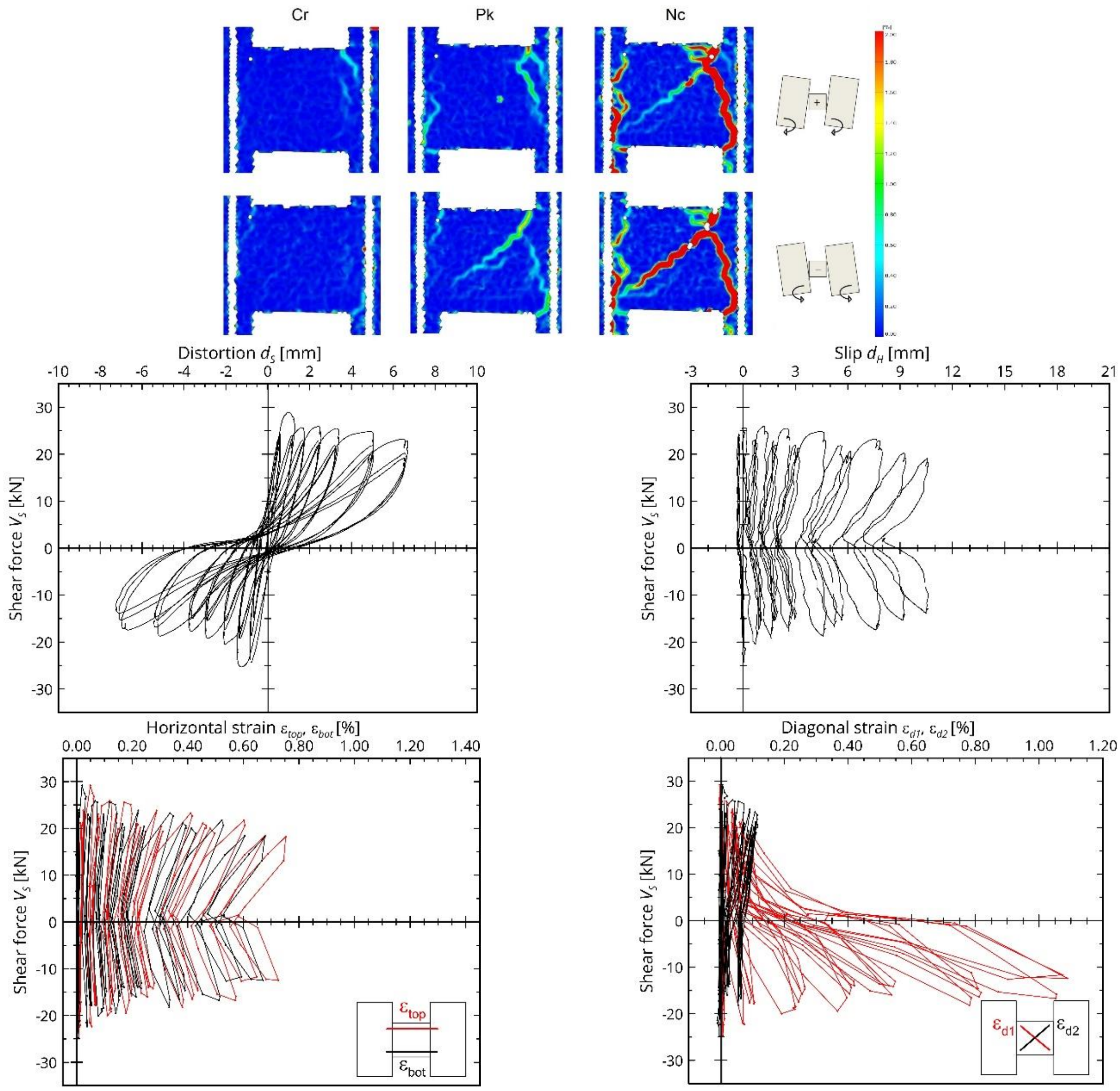

Fig. 3.3.4 Main results of test S-R2U-1.

- Test S-R2R-1 (Fig. 3.3.5)

The first cracks occurred at the opposite corners of the spandrel and initially involved only the mortar of the coating; then the cracks extended almost vertically, also new parallel cracks formed nearby. Inclined and diagonal cracks developed, spreading over the entire coating surface till the progressive failure of the GFRP wires, leading to a rapid load decrease. Mainly the horizontal wires at the spandrel corners fractured, indicating that final failure was due to bending, despite numerous diagonal cracks. During the test, the bond of the coating with the masonry was gradually lost over a large area of the cracked spandrel; no separation between the wall leaves was observed. On the unstrengthened back side, the masonry cracks were fewer than on the strengthened front side and reproduced the crack pattern of a plain wall, S-R2U-1. The right support began sliding quite early, as the first cracks occurred; the residual sliding progressed with the cycles. The horizontal strains progressed almost symmetrically, and so did the diagonal strains.

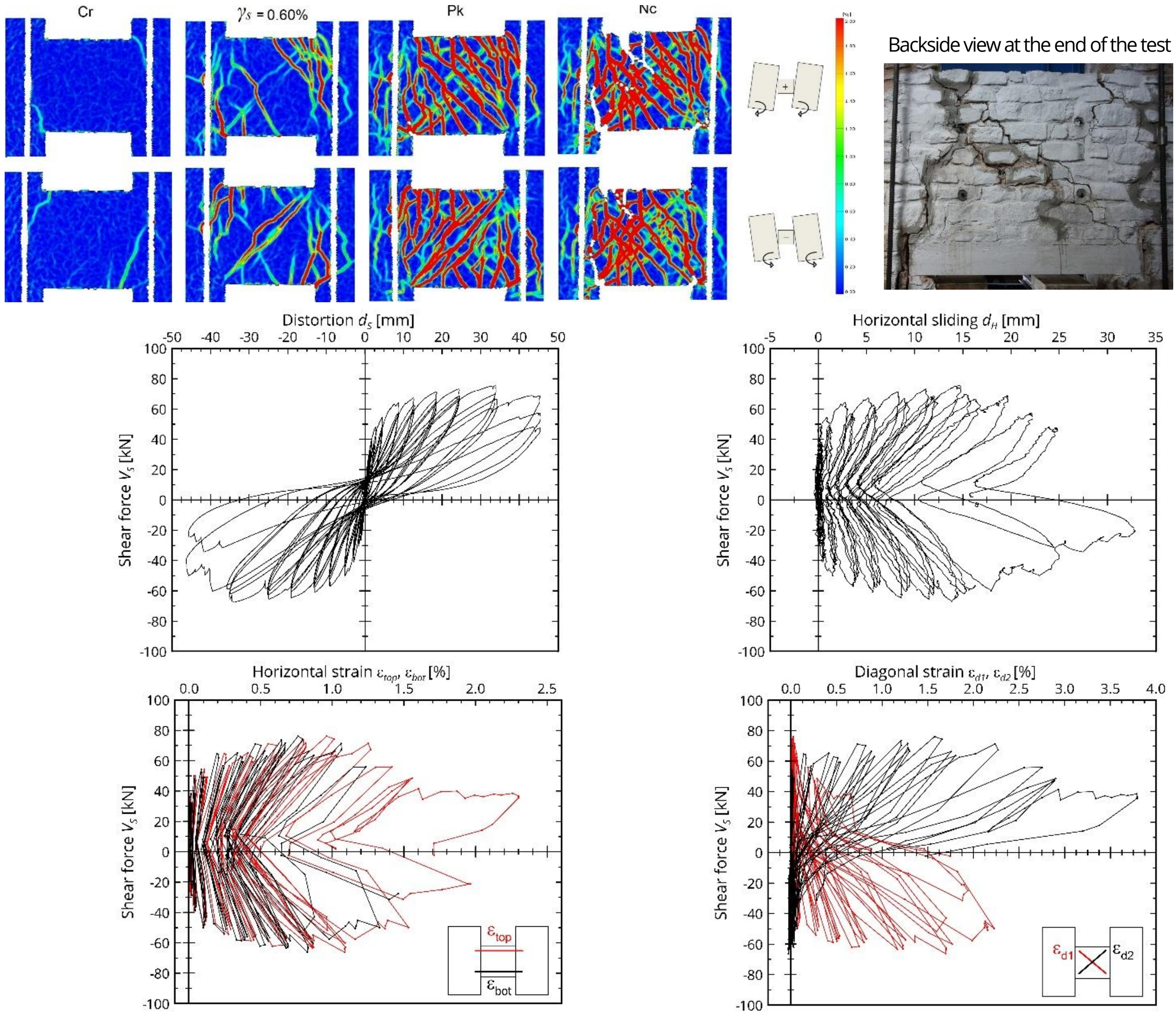

Fig. 3.3.5 Main results of test S-R2R-1.

- Test S-R2U-2 (Fig. 3.3.6)

The first cracks appeared at the opposite corners and the damage concentrated in two main, almost vertical cracks at the spandrel extremities, indicating failure governed by the bending mechanism (diagonal strains were quite negligible). Similar cracks emerged on both sides of the sample, spanning the full thickness of the wall. After the peak load, a gradual drop or resistance was surveyed, also with the progressive gradual residual slip between the piers. The horizontal strains at top and bottom were almost comparable.

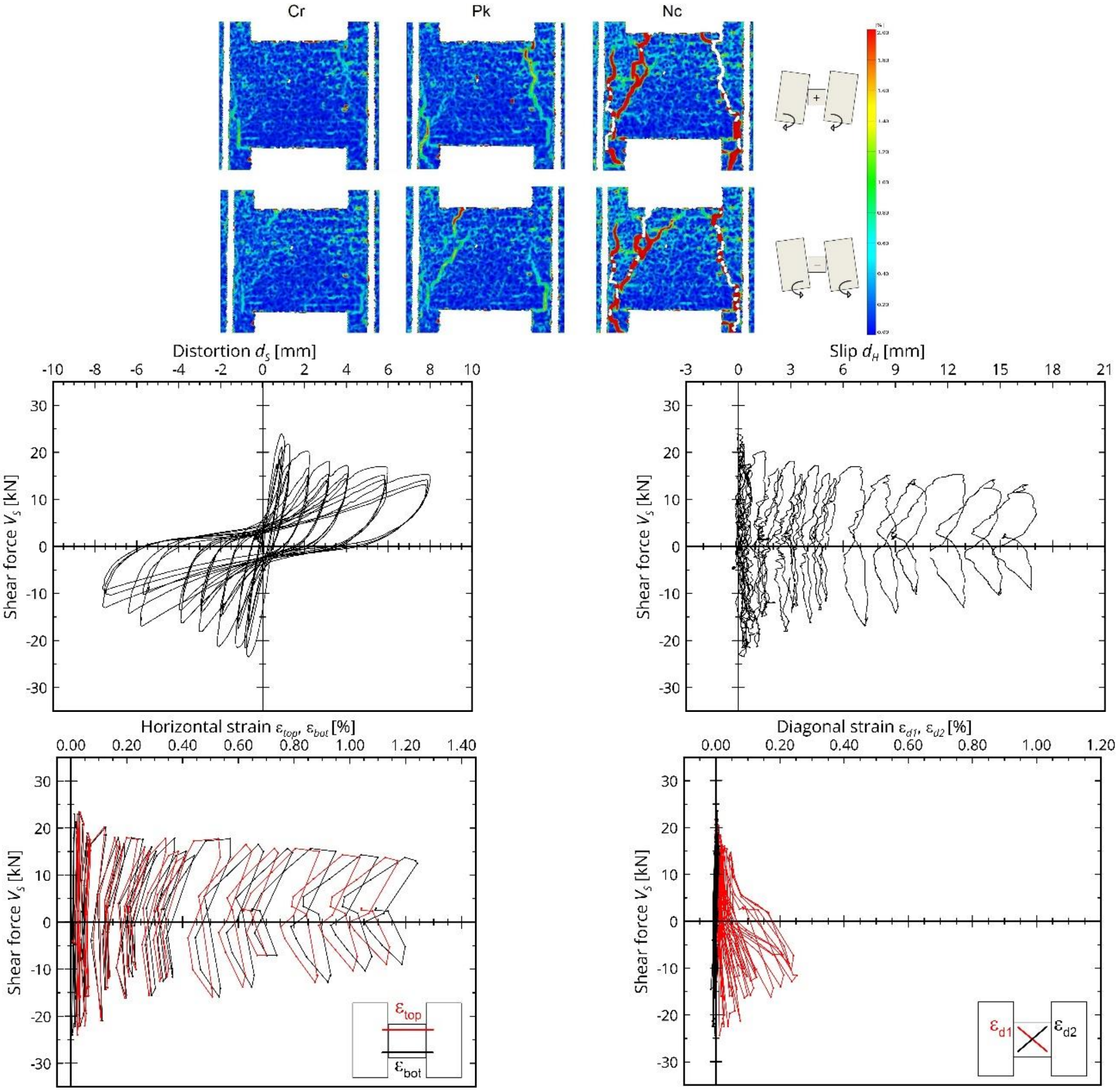

Fig. 3.3.6 Main results of test S-R2U-2.

- Test S-R2R-2

The first cracks formed in the coating, at opposite corners of the spandrel, displaying a vertical pattern. These cracks progressively extended and, due to load reversal, spanned the entire height of the spandrel. Additional vertical cracks appeared near the previous ones, followed also by inclined cracks in the coating within the spandrel area, so that the entire coating surface was covered by cracks once the peak resistance was reached. The collapse mode was flexural: the vertical crack at the right end of the spandrel widened, leading to the failure of the GFRP wires crossing the crack, on both the front and back sides. At the end of the test, some debonding of the coating from the masonry was observed around the wider cracks. Additionally, initial separation of the wall leaves was detected in the pier portions below the lintel. The horizontal sliding at the right support was quite limited until peak load; after that, increasing values were recorded, along with significant residual slip.

Actually, during the data post-processing, it emerged that a malfunction determined an unexpected, progressive reduction of the axial pre-stress level after the first cracking. With the reduced vertical load, N_S, horizontal cracks formed at the base of both piers, at the interface between the masonry and the RC beams: a crack opened from the inner corner of the left pier when loading in the positive direction, and from the inner corner of the right one for the opposite loading. The alternated opening of these cracks limited the actual rotation of the cracked pier in respect to that imposed by the apparatus, affecting the net spandrel distortion. The bottom horizontal strains resulted significantly higher that the top ones; diagonal strains were comparable.

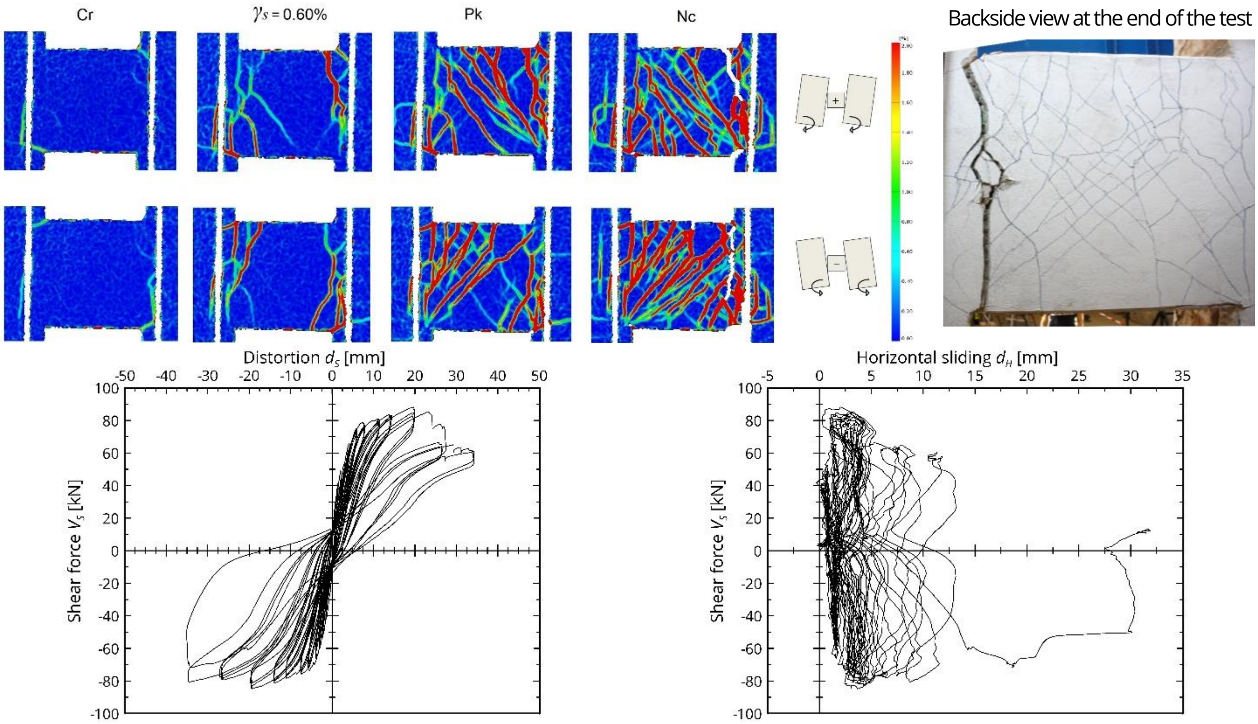

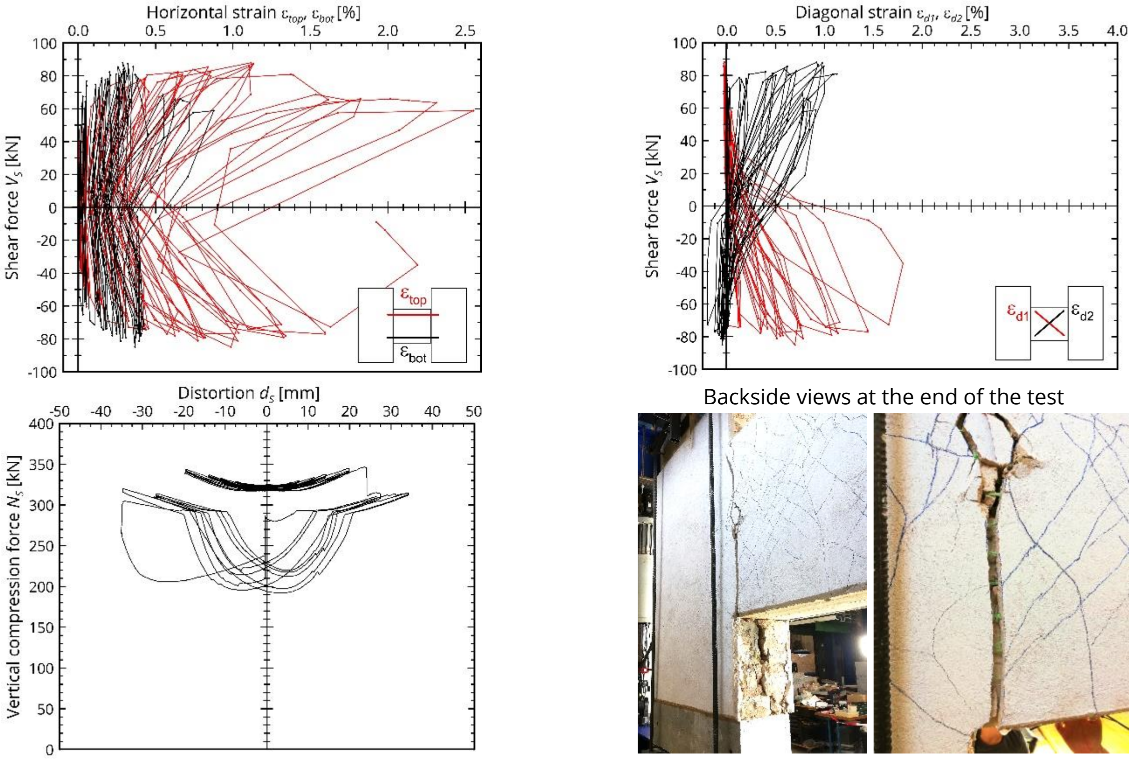

Fig. 3.3.7 Main results of test S-R2R-2.

- Test S-B2U (Fig. 3.3.10)

The first significant cracking occurred almost at the attainment of the peak load: the cracks were inclined, running mostly through the mortar joints (diagonal shear failure mechanism) and determined an abrupt resistance decay and a large horizontal sliding at the base right support. This triggered the lower portion of the masonry spandrel (mainly, the jack arch), fully surrounded by cracks, to detach from the upper portion at the end of the test. The crack pattern was identical on both sides of the sample, spanning the full thickness of the wall. The horizontal strains at top and bottom resulted almost comparable, as well as the diagonal strains (which clearly detected the occurrence of symmetric diagonal cracking).

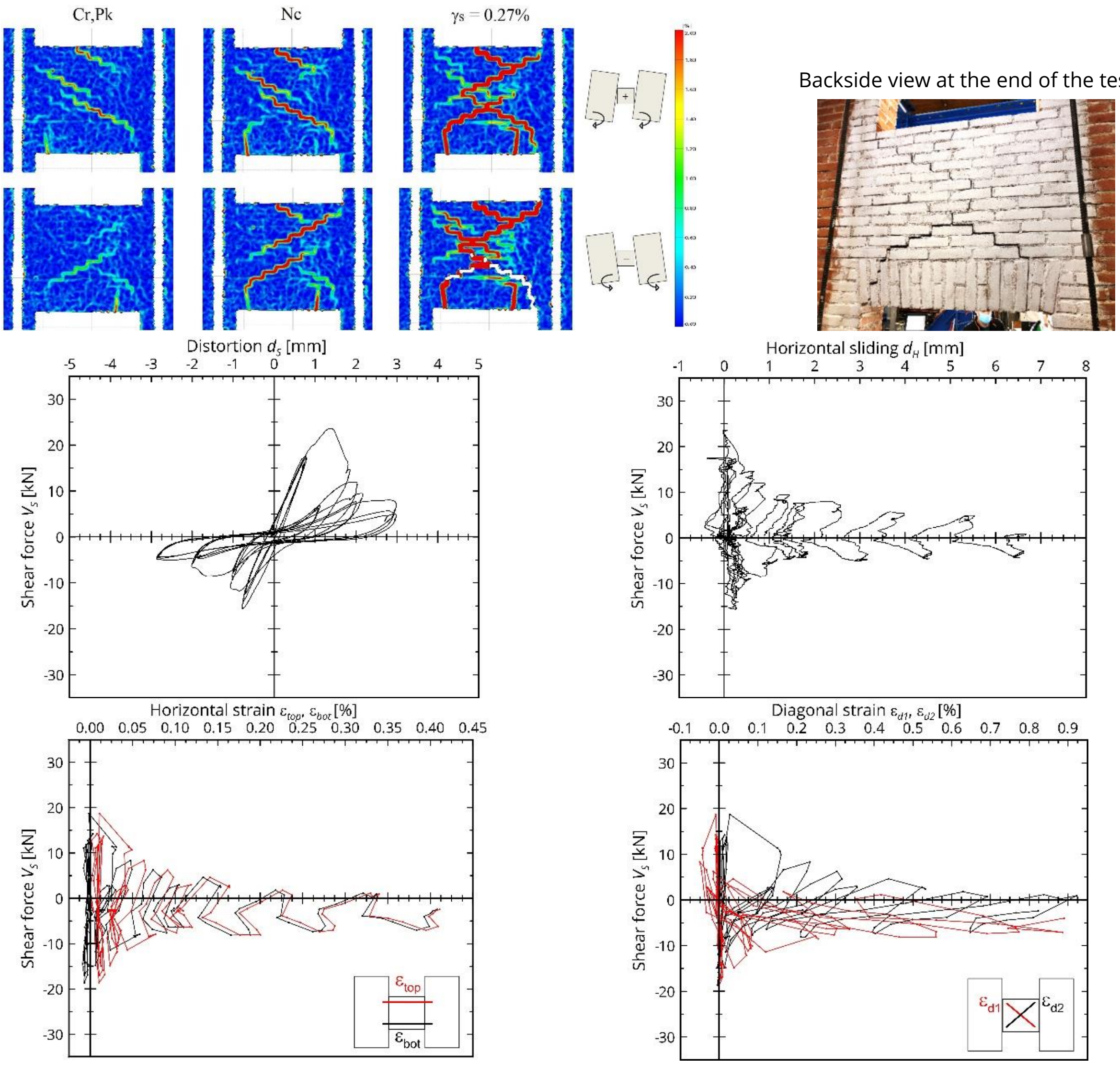

Fig. 3.3.8 Main results of test S-B2U.

- Test S-B2R (Fig. 3.3.11)

The first cracks formed in the coating, at diagonally opposite corners of the spandrel, then the cracks progressively spread: they were initially almost vertical, but then also diagonal cracks appeared in the centre. When peak load was reached, the cracks covered the entire spandrel surface. On the reverse side (unstrengthened masonry), the cracks also gradually diffused, but the trend was that of stepped cracking that mainly followed previously repaired cracks. The lower masonry portion of the spandrel (the jack arch) tended to detatch (similar to what occurred in the unstrengthened configuration). The final collapse was due to failure of some vertical GFRP wires around the left end of the spandrel, reminiscent of vertical shear sliding. No layer separation emerged between the wall leaves but some deobonding of the coating around the cracked areas; however the composite action was maintained until the end. The horizontal strains progressed almost symmetrically, and so did the diagonal strains.

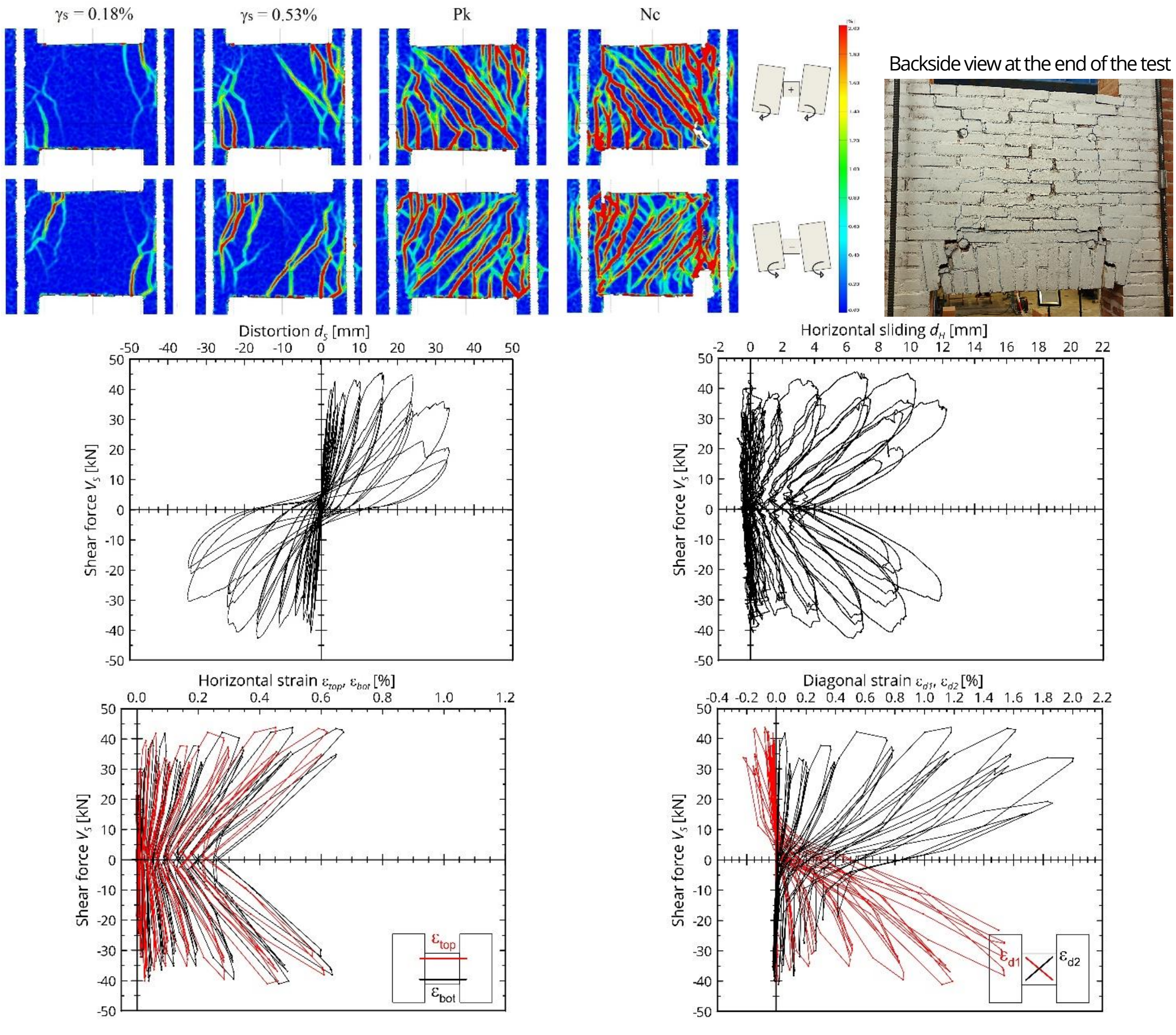

Fig. 3.3.9 Main results of test S-B2R.

- Test S-B1U (Fig. 3.3.10)

The first cracks occurred at the ends of the jack arch, first at the left corner of the spandrel (when loading in the positive direction) and then suddenly also in the right corner (when loading in the negative one). When reaching peak load, cracks also formed around the top corners of the spandrel, leading to activation of the bending failure mechanism. The upper cracks then opened with an inclined pattern, while the lower cracks opened almost vertically, causing a rapid load drop. A horizontal crack also appeared at the top of the jack arch. After the peak load, the right pier moved horizontally, regardless of the loading direction. By the end, the arch was completely surrounded by cracks and on the verge of collapse. The damage pattern on the back of the wall mirrored that on the front, with cracks running almost exclusively through the mortar joints. The horizontal strains at top and bottom were almost comparable; the diagonal strains resulted almost negligible

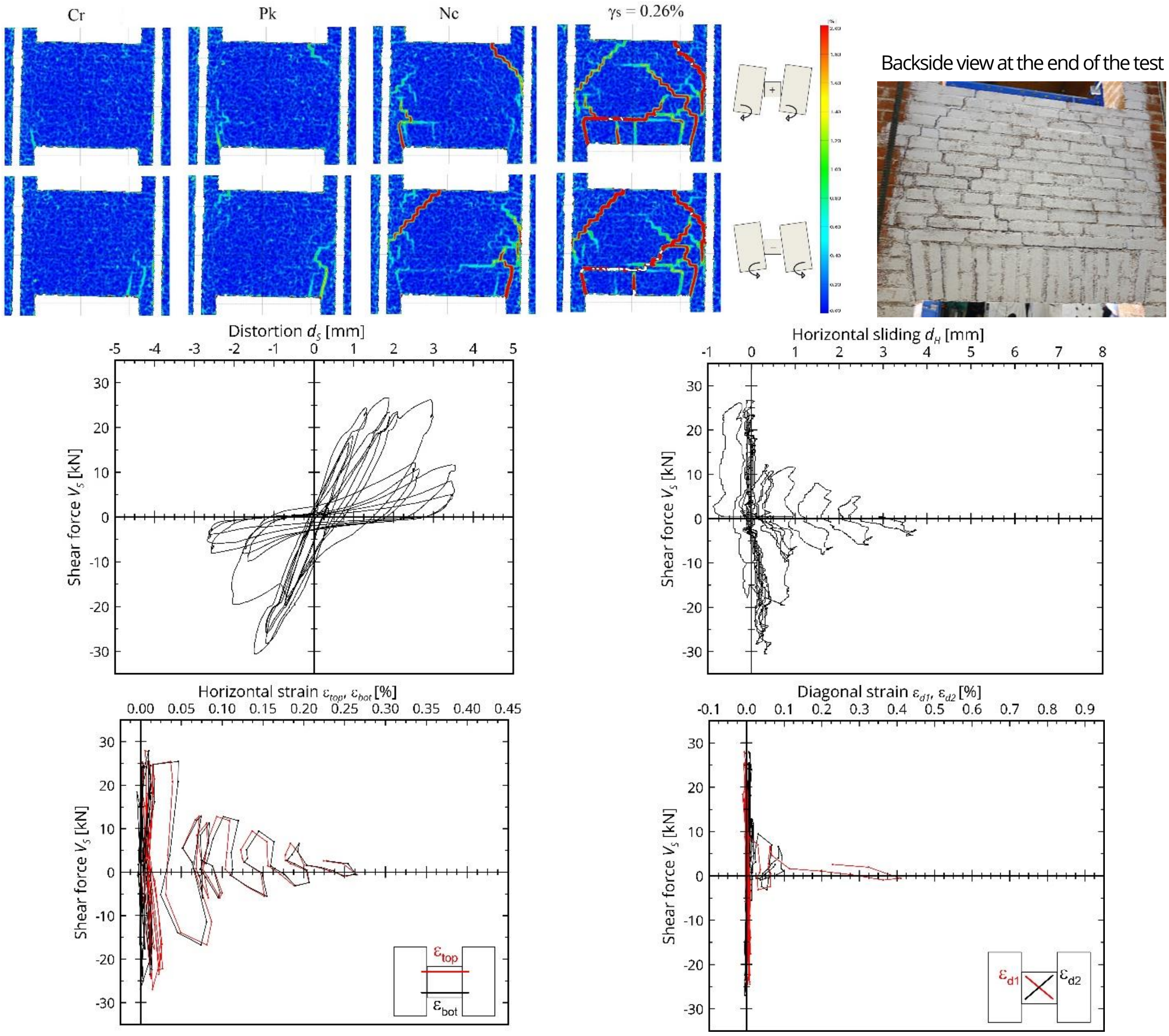

Fig. 3.3.10 Main results of test S-B1U.

- Test S-B1R (Fig. 3.3.11)

Cracks in the coating firstly activated in the spandrel's lower corners and then, at the top corners. Such cracks progressed almost vertically, meanwhile other incluned cracks gradually occurred in the vicinity. At the reaching of the peak load, the entire coating was diffusely covered by cracks, and the cracks at the centre of the spandrel were diagonal. Then, the horizontal GFRP wires at the right end of the spandrel progressively failed in tension, starting from the bottom corner. The coating debonded in the cracked areas, but the anchors and the diatones maintained composite action. The unstrengthened side experienced inclined cracks very similar to those observed in the test of the unstrengthened wall, S-B1-U. The crack above the jack arch opened again, but the arch fallin was prevented. The sliding of the right support was significant and also in the residual sliding. Both the horizontal strains and the diagonal ones progressed almost symmetrically.

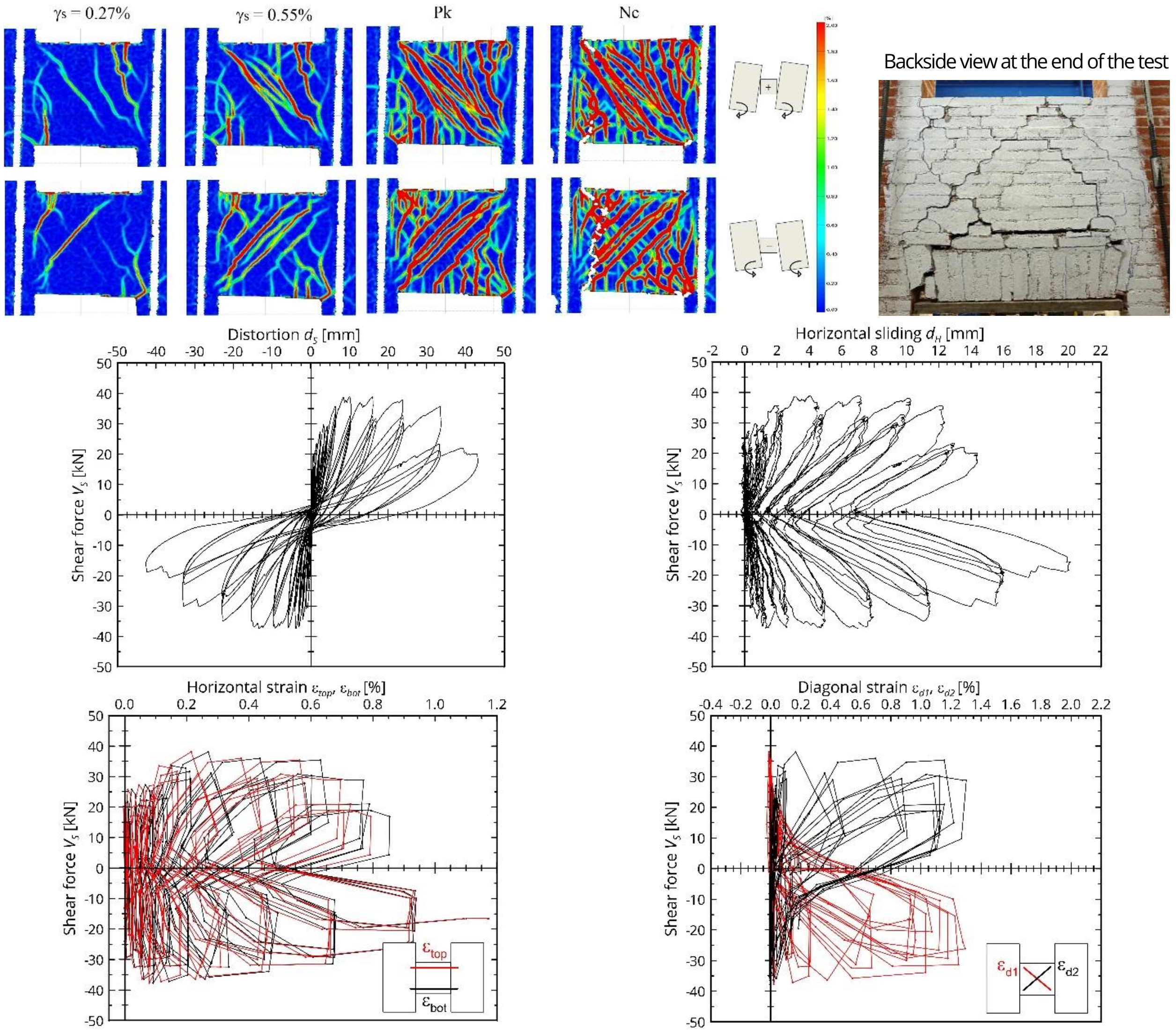

Fig. 3.3.11 Main results of test S-B1R.

The capacity curves of unstrengthened and CRM strengthened spandrel samples are compared in Fig. 3.3.12. The values of shear force V_S and distortion d_S obtained from the eight experimental tests are summarized in Table 3.4 and in Fig. 3.3.13 for the three limit state, namely, first cracking, peak load and near collapse (*Cr*, *Pk*, *Nc*). The latter was identified at the occurrence of a 30% load decrease after the peak load.

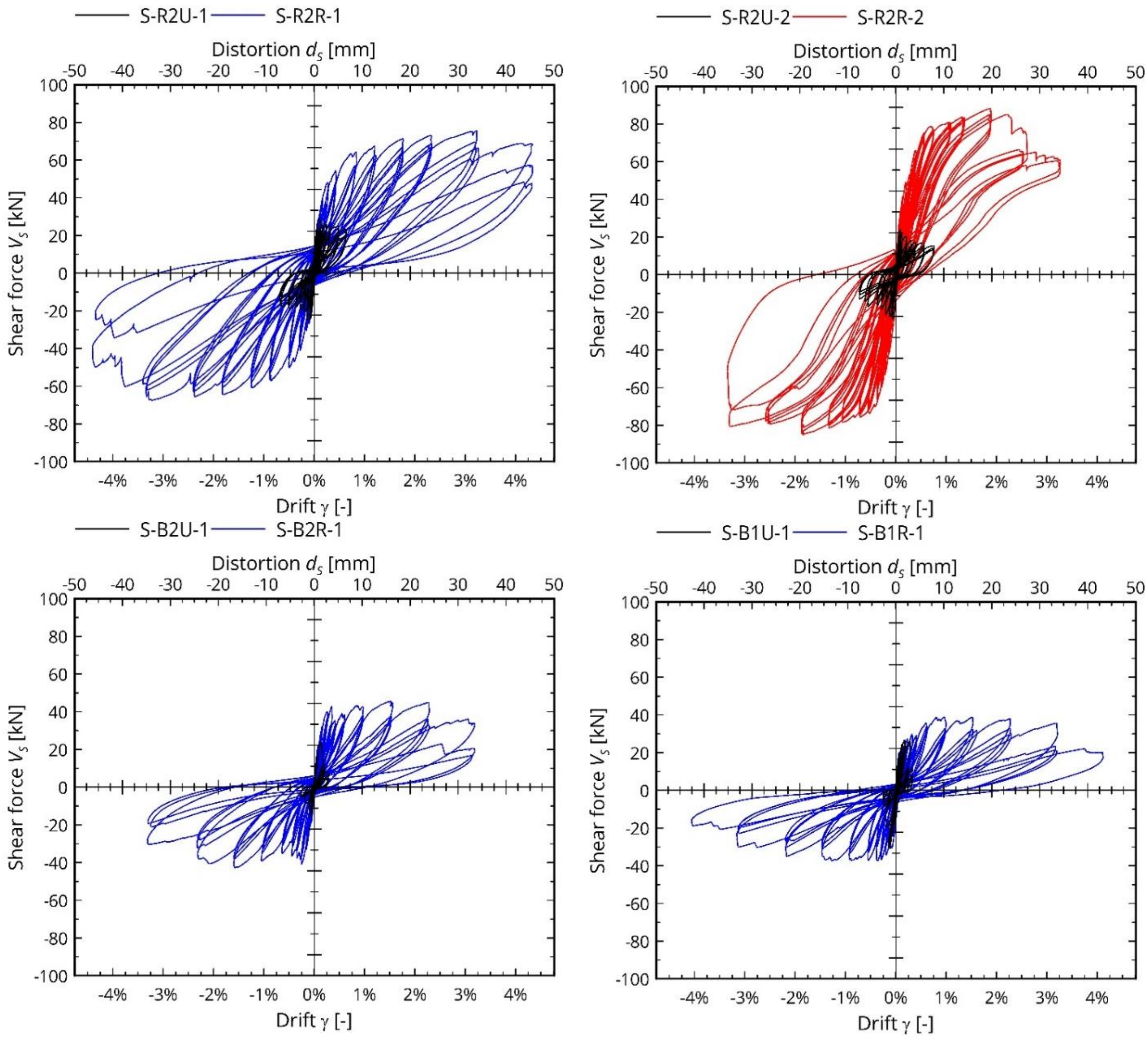

Fig. 3.3.12 Comparison of capacity curves of unstrengthened and CRM strengthened spandrel samples.

Table 3.5 Values of the shear force (V_S) and distortion (d_S) measured in positive and negative loading directions, for the first cracking, peak load and near collapse limit states.

ID	First cracking (*Cr*)		Peak load (*Pk*)		Near collapse (*Nc*)	
	V_S [kN]	d_S [mm]	V_S [kN]	d_S [mm]	V_S [kN]	d_S [mm]
S-R2U-1	23.3	0.28	28.9	0.49	20.2	4.27
	-24.0	-0.33	-25.3	-0.55	-17.7	-4.23
S-R2R-1	29.7	0.26	75.5	18	52.8	24.7
	-26.7	-0.29	-67.5	-17.6	-47.2	-24.6
S-R2U-2	22.1	0.19	23.9	0.26	16.7	3.22
	-22.4	-0.12	-23.5	-0.19	-16.4	-3.15
S-R2R-2	48.6	0.63	88.1	17.8	61.7	31.69
	-53.0	-0.71	-84.8	-17.6	-59.4	-32.15
S-B2U-1	+23.6	+0.44	+23.6	+0.44	+16.5	+0.85
	-15.7	-0.30	-15.7	-0.30	-11.0	-0.55
S-B2R-1	+21.6	+0.26	+45.5	+8.4	+31.9	+18.05
	-23.8	-0.29	-42.7	-8.4	-29.9	-18.50
S-B1U-1	+22.9	+0.29	+26.6	+0.59	+18.6	+1.09
	-26.8	-0.26	-30.6	-0.54	-20.1	-1.17
S-B1R-1	+19.6	+0.33	+38.9	+8.7	+27.2	+18.4
	-23.2	-0.14	-37.4	-7.5	-26.2	-18.4

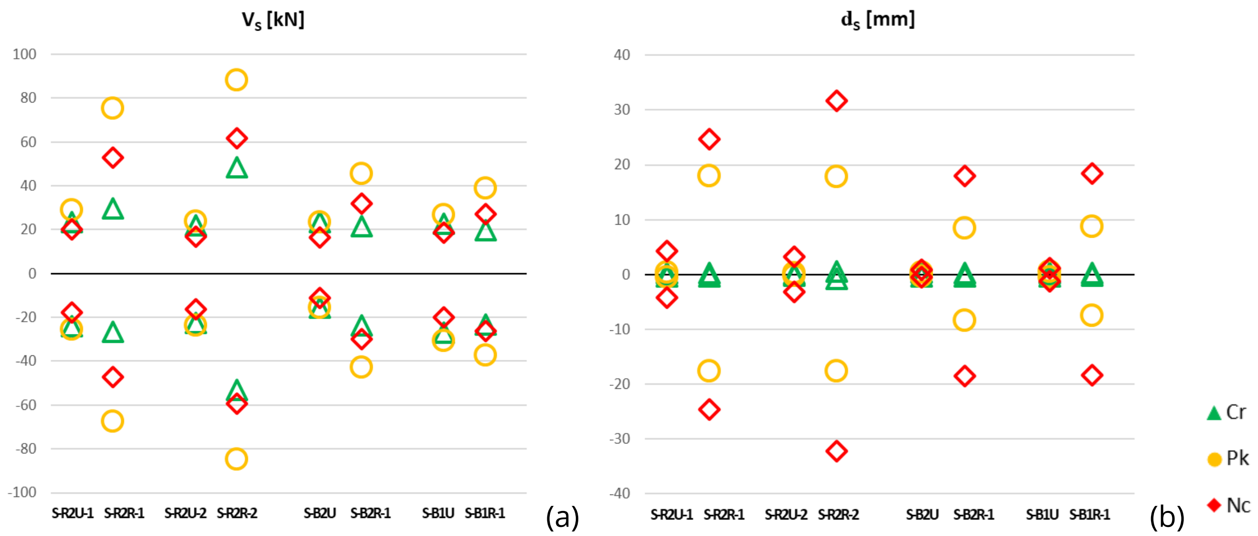

Fig. 3.3.13. Main test results of "S" samples: first cracking, peak and near collapse forces (a) and distortion (b)

The failure of the two unstrengthened rubble stone spandrels and of the single-leaf solid brick masonry was dominated by the bending mechanism, as evidenced from the typical crack pattern with sub-vertical cracks at the spandrel extremities (with cracks running mostly through the mortar joints). Very similar peak resistance values were attained: 27.1 kN for S-R2U-1, 23.7 kN for S-R2U-2 and 28.6 kN for S-B1U. In contrast, the unreinforced masonry spandrel made of double-leaves solid brick failed by shear (diagonal cracks, mean peak load 19.7 kN). The capacity curves showed a quite ductile response for the stone samples with the timber lintel (ultimate displacements 4.25 mm and 3.19 mm, for S-R2U-1 and -2), while the response was brittle in case of masonry arch (0.7 mm for S-B2U and 0.3 mm for S-B1): at the end of the tests, the arch was completely surrounded by cracks and was about to fall.

In the strengthened spandrels, the first nearly vertical cracks formed in the coating, at the extremities of the spandrel (activation of bending mechanism), but then progressively spread, and diagonal cracks also appeared (activation of diagonal cracking mechanism), covering the entire spandrel. At the end of the tests, the bond between the coating and the spandrel was lost in the cracked areas, but the anchors assured the composite action until the end, when the GFRP wires progressively failed in tension at the extremities. It resulted mean peak loads of 71.5 kN for S-R2R-1, 44.1 kN for S-B2R-1 and S-B1R-1; the mean ultimate displacements were 24.7 mm, 18.3 mm and 18.4 mm, respectively. For the sample S-R2R-2, the mean peak resistance and ultimate displacement values were 86.5 kN and 31.9 mm. However, as already noted, the accidental malfunction of the vertical pressure control system limited the pier rotation, affecting the net spandrel distortion.

In the rubble stone masonry, the one-side retrofitting intervention increased the spandrel resistance to 2.8 times of original and the ultimate distortion by 6.6 times with respect to the plain masonry. In case of retrofitting at both sides, the improvement was 3.4 and 8.6 times for the same quantities (lower than expected due to the anomaly in the vertical loading system). In the sigle-leaf solid brick masonry, the peak force of the one-side retrofitted configuration was 2.24 times that of of the unstrengthened one and the distortion more than 26.1 times higher. In the double-leaves solid brick masonry, increment ratios were, respectively, 1.33 and 16.3 times.

The cyclic tests allow also to draw the trends of the spandrels cycle stiffness, K_S (evaluated as the slope of the peak-to-peak line within each loop of the V_S–d_S curve) by varying the distortion d_S (Fig. 3.3.13a). The stiffness degradation with increasing distortion shows an approximately power-law trend, with a softer degradation in the strengthened samples, in respect to the unstrengthened ones. The stiffness gap within the three loops of a single target displacement was quite low. At the end of the tests, the cycle stiffness degraded by about 90–95% of the initial value.

The cumulative input energy (E_{in}) and the dissipated hysteretic energy (E_{hys}) were quantified (Fig. 3.3.13b-c), as well as the E_{hys}/E_{in} ratios (Fig. 3.3.13d). E_{in} is the cumulative work to deform the sample from the beginning of the test to a specific target value of distortion. For each loading cycle, it corresponds to the area under the positive and negative branches of the hysteretic loop of the F_S-d_S graph. Similarly, the cumulative dissipated hysteretic energy E_{hys} is the sum of all the areas included in the hysteretic loops. Three points for each target displacement are reported because of the three iterations cyclic.

For the strengthened samples, an approximate estimation of the equivalent hysteretic damping with varying target displacement was performed (accordingly to the procedure reported in FEMA 440 - [1]), by distinguishing the values of each of the three load iterations (Fig. 3.3.13e).
In general, significantly higher input and dissipated cumulative energies resulted from the strengthened samples, in respect to the plain masonry (Table 3.6). The cumulative dissipated energy at near collapse increased by 21-22 times for R2, by 66 times for B2 and by 26 times for B1. At a given target drift, the reduction in ξ_{hys} result greater between the second and third cycles than between the first and second. Approaching the peak load ξ_{hys} was about 0.11 in S-R2R-1 and 0.08 in S-R2R-2; at the near-collapse limit, ξ_{hys} 0.14 and 0.09, respectively. The values of ξ_{hys} at peak load (0.10–0.11) and near collapse (0.13) almost coincided in S-B1R-1 and S-B2R-1.

Table 3.6 Cumulative input energy E_{in} and dissipated hysteresis E_{hys} at peak load (Pk) and at near collapse (Nc), and mean energy ratio in the cycles (E_{hys}/E_{in})

ID	Peak load (*Pk*)			Near collapse (*Nc*)		
	E_{in} [J]	E_{hys} [J]	E_{in}/E_{hys} [-]	E_{in} [J]	E_{hys} [J]	E_{in}/E_{hys} [-]
S-R2U-1	119.8	78.6	0.66	1233.0	807.8	0.66
S-R2R-1	18496.4	9462.8	0.51	30045.2	16591.2	0.55
S-R2U-2	34.9	23.5	0.67	831.1	641.1	0.77
S-R2R-2	16100.1	5941.8	0.35	35706.6	14362.3	0.40
S-B2U-1	83.8	48.2	0.58	125.2	77.9	0.62
S-B2R-1	4069.1	1883.4	0.46	9560.2	5109.7	0.53
S-B1U-1	152.3	66.8	0.44	334.6	174.0	0.52
S-B1R-1	3333.4	1757.2	0.53	8006.4	4463.2	0.56

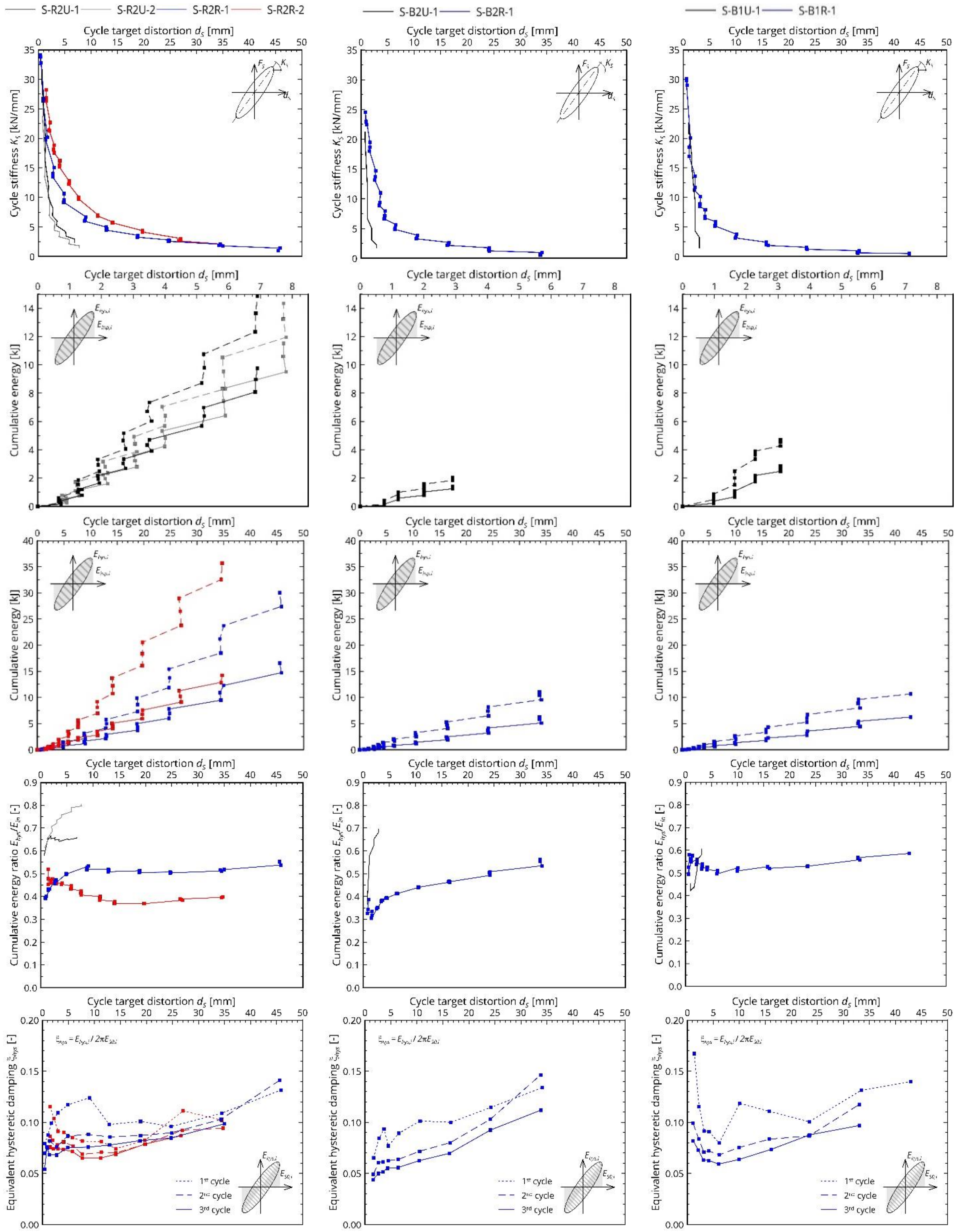

Fig. 3.3.14. Spandrels stiffness and energy characteristics, varying the cycle target distortion d_S.

3.3.2. Analytic model

Symbols:

t	masonry spandrel thickness
b	masonry spandrel width
l	masonry spandrel height (i.e. "effective length")
b_h	average height of a masonry row
b'	net masonry spandrel height (typically, lintel is not considered)
ρ	coefficient = $b'/4b_h$
d_{eff}	effective overlap length of blocks
E_m	masonry Young's modulus
G_m	masonry shear modulus (~$1/3E_m$)
i	number of CRM-strengthened sides (1-2)
t_c	plaster nominal thickness
E_c	plaster Young's modulus
G_c	plaster shear modulus (~$0.4E_c$)
η	coefficient related to the spandrel static scheme (e.g. 3 for cantilever, 12 for shear type)
I	second bending moment of the uncracked spandrel cross section ($tb^3/12$)
σ_0	mean compressive stress on the spandrel. Max. between horizontal compressive stress (if known) and vertical one (evaluated on the basis of the floor load and the diffusion of vertical stresses in adjacent piers). However, it is typically assumed = 0.
σ_{0P}	vertical compressive stress on the piers adjacent to the spandrel
f_m	masonry compressive strength (vertical direction)
$f_{m,h}$	masonry compressive strength (horizontal direction)
τ_0	equivalent masonry shear strength for $\sigma_0 = 0$ (for "Turnšek and Čačovič" formula)
f_{v0}	masonry shear strength for $\sigma_0 = 0$ (shove test)
β	spandrel slenderness factor ($1.0 \leq \beta = l/b \leq 1.5$)
χ	effectiveness reduction factor (=1 for CRM at both-sides, ≤1 at one side)
γ	model coefficient (=2)
A_G	net cross section of a GFRP wire
T_G	mean tensile resistance of a GFRP wire
s	GFRP mesh grid pitch
l_f	CRM effective length (=l, but ≤b')
$\varepsilon_{lim,G}$	limit tensile strain of GFRP
E_G	GFRP Young's modulus
α	coefficient of bending moment distribution (e.g. 1 for cantilever, 2 for shear type)
x	depth of the neutral axis of the cracked cross-section

The empirical evidence has shown that the in-plane behavior of unreinforced masonry spandrels without horizontal ties can be schematized analytically, in a simplified way, as an elastic-brittle behaviour with some residual resistance (Fig. 3.2.15a). Differently, when a horizontal tensile-resistant element is provided (e.g. a steel rod, a r.c. ring beam, a metallic profile, the CRM reinforcement, a fiber-based composite strip…) an elastic-plastic behaviour it is more appropriate (Fig. 3.2.15b).

To estimate the stiffness, resistance and ultimate displacement capacities, well-known correlations available in the literature can be considered for the unstrengthened masonry. For CRM strengthened masonry, the correlations need to be adjusted to account for the CRM contribution.

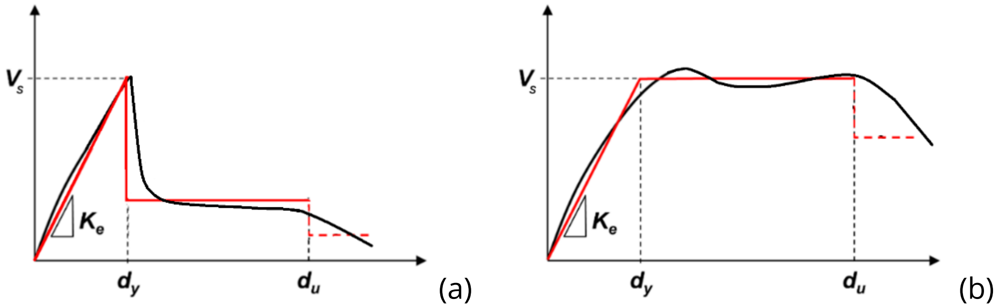

Fig. 3.3.15 Generic, simplified elastic-brittle (a) or elastic-plastic (b) schematization of the in-plane lateral performances of masonry spandrels (red line), in comparison with actual performances (black line).

To evaluate the spandrel stiffness, K_e, both the flexural and shear deformability should be accounted for, as indicated in Eq.(3.11). In case of CRM strengthened masonry, equivalent Young and shear moduli shall be considered, evaluating the average values between masonry and mortar coating, weighted on the respective thickness.

$$K_e = \frac{1}{\frac{l^3}{\eta I E} + \frac{1.2 l}{G b t}} \tag{3.11}$$

For the evaluation of the spandrel's in-plane lateral resistance, V_S, the weakest mechanism between shear failure, $V_{S,d}$, and bending, $V_{S,f}$, is considered:

$$V_S = \min(V_{S,d}; V_{S,f}). \tag{3.12}$$

The typical crack patterns that occur during seismic events are illustrated in Fig. 3.3.16. For these mechanisms to activate, the diagonal masonry strut should not prematurely fail in compression:

$$V_S \le 0.25 \cdot b' t \cdot f_m \tag{3.13}$$

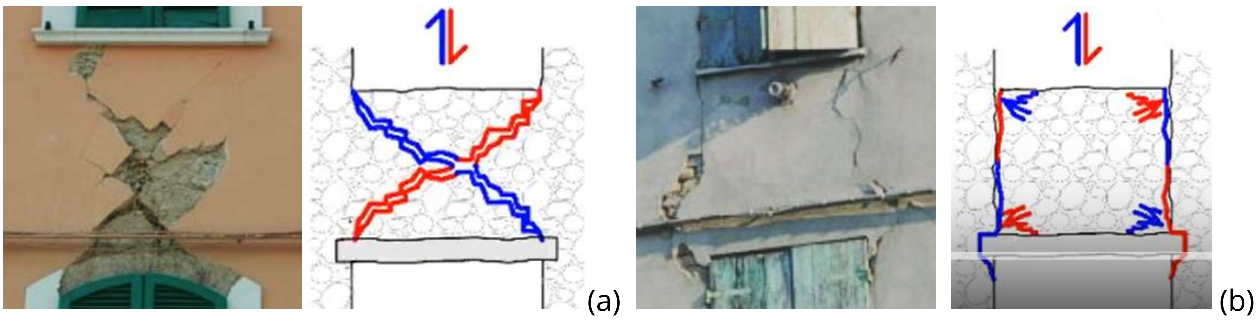

Fig. 3.3.16 Typical in-plane failure mechanism of masonry spandrels: diagonal cracking (a) and bending (b).

For the unstrengthened masonry spandrels (suffix URM), different resistant models can be found in the literature to estimate $V_{S,d(URM)}$. For example, the well-known “Turnšek and Čačovič” correlation, suitable for both regular and irregular masonry, can be applied (according to C8.7.1.16 in MIT 2019 [2]):

$$V_{S,d(URM)} = \frac{1.5\tau_0}{\beta} b' \cdot t \sqrt{1 + \frac{\sigma_o}{1.5\tau_0}} \tag{3.14}$$

Conservatively, the net masonry spandrel height (without lintel) is considered. When failure is dominated by the shear mechanism, a residual resistance, $V'_{S,d(URM)}$, shall be considered. $V'_{S,d(URM)}$ can be estimated proportionally to $V_{S,d(URM)}$ (0.6 for r.c. or steel lintel, 0.4 for timber lintel, 0.1 for masonry arch - [2]).
To estimate the in-plane bending resistance of unreinforced masonry spandrels without an effective horizontal tie (suffix *t0*), Eq. (3.15) can be used with the additional expression for $f_{t,eq}$ (7.3.4 in FEMA 306 [5]), which considers the contribution of block-to-block interaction (cohesion and friction) at the spandrel’s ends:

$$V_{S,f(URM,t0)} = \frac{\alpha M_{S(URM,t0)}}{l} = \frac{\alpha}{l}\frac{2}{3} f_{t,eq} \cdot t \cdot b_h \cdot b' \cdot \rho \qquad \text{with}$$
$$f_{t,eq} = \frac{d_{eff}}{b_h}\left(f_{V0} + 0.65 \cdot \sigma_{0P}\right) \tag{3.15}$$

When failure is dominated by the bending mechanism, a residual resistance, $V'_{S,f(URM)}$, shall be considered. $V'_{S,f(URM)}$ can be estimated by neglecting the cohesion contribution (i.e. assuming f_{v0} = 0 in Eq. (3.15)).

Both mechanisms benefit from the contribution of the CRM system, as the fiber-based composite material (the mesh wires), crossing both the diagonal and the vertical cracks, limits their opening, fostering a wider stress diffusion. However, to be effective against the bending failure, the CRM system has to be sufficiently extended beyond the spandrel area.
In the lack of specific correlations for the evaluation of the resistance of CRM strengthened masonry spandrel (suffix CRM), reference is herein made to CNR-DT 215/2018 [4], an Italian guideline available for FRCM strengthening systems, that have several similarities with CRM ones.
According to [4], the contribution given by the wires along the loading direction crossing the diagonal crack shall be added to that of the unstrengthened masonry:

$$V_{S,d(CRM)} = V_{S,d(URM)} + \chi \frac{1}{\gamma} \cdot i \cdot \frac{A_G}{s} \cdot l_f \cdot \varepsilon_{\lim,G} \cdot E_G \,. \tag{3.16}$$

Note that, if the tensile failure of the fibers is attained, the factor $A_G \cdot \varepsilon_{\lim,G} \cdot E_G$ corresponds to the tensile resistance of a single wire, T_G. It is also observed that, coherently with the behavior of the unreinforced masonry spandrel (Fig. 3.3.15a), its residual resistance, $V'_{S,d(URM)}$, should prudentially be considered, instead of the peak one, $V_{S,d(URM)}$.

For the bending failure mechanism of the CRM strengthened masonry spandrel, the tensile-resistant contribution of the horizontal wires crossing the vertical cracks at the end sections shall be accounted:

$$V_{S,f(CRM)} = \frac{\alpha M_{S(CRM)}}{l} = \frac{\alpha}{l}\left[0.8x \cdot f_{m,h} \cdot t\left(\frac{b'}{2} - 0.4x\right) + \chi \frac{i \cdot A_G \cdot \varepsilon_{\lim,G} \cdot E_G}{s} \cdot \frac{(b'-x)}{2}\left(\frac{b'}{6} + \frac{x}{3}\right)\right] \qquad (3.17)$$

$$\text{with} \quad x = b' \cdot t\left(\sigma_0 + \chi \frac{i\, A_G \cdot \varepsilon_{\lim,G} \cdot E_G}{2s \cdot t}\right) \Big/ \left(0.8 \cdot f_{m,h} \cdot t + \chi \frac{i \cdot A_G \cdot \varepsilon_{\lim,G} \cdot E_G}{2s}\right).$$

Basically, $M_{S(CRM)}$ shall be evaluated by analysing a reinforced section subjected to combined compression and bending in cracked conditions, assuming conservation of plane sections, perfect bond among materials, masonry cracked in tension (no residual frictional contribution) and plastic in compression, fiber mesh with linear-elastic behaviour in tension until reaching the limit strain. Conservatively, the net masonry spandrel height, *b'*, is considered; however, in presence of a lintel that effectively indents at the extremities, the gross height, *b*, can be assumed instead of *b'*. Note that, for this correlation to provide reliable results, it is necessary to ensure that the masonry does not reach the ultimate compressive strain while the fiber wires are still in the elastic range.

It is observed that the plaster contribution is neglected in both mechanisms. It is also worth noting that the introduction of effective transversal connectors in multiple-leaves masonry could be grossly considered by increasing the masonry shear strength, τ_0. Appropriate coefficients (range 1.2-1.5, depending on masonry type) are provided in C8.5.II of MIT 2019 [2].

The ultimate displacement capacity of the masonry spandrel, d_{Su}, is evaluated on the basis of the chord rotation limits at the spandrel extremities, θ_{Su}.

For unstrengthened masonry spandrels without effective horizontal tie, the residual resistance for both failure mechanisms, is maintained up to $\theta_{Su(URM,t0)}$ = 0.015 (C8.7.1.3.1.1 of MIT 2019 [2]).

For CRM masonry, in the lack of any guidance, doubled values could be considered, based on experimental evidence ($\theta_{Su(CRM)}$ = 0.030).

3.3.3. Application and validation

The analytical model described in §3.3.2 is adopted to evaluate the lateral performances of the CONSTRAIN experimental tests on the spandrel samples resumed in §3.3.1.
The mechanical characteristics of the unstrengthened masonry (E_m, τ_0, f_m) considered in the formulations are those already applied for the masonry piers in §3.2.3. The masonry horizontal compressive strength, $f_{m,h}$, is taken as $f_m/2$. The value of f_{v0} for R2 masonry is calculated from the CONSTRAIN experimental test S-R2U (§3.3.1), by solving Eq. (3.15) for f_{v0} (for the resistance $V_{P,d(URM)}$, the peak load is taken and the mean value between positive and negative loading directions is considered). Coherently to the approach already adopted for the piers, for the solid brick samples, the values were taken from Tab.C8.5.I of MIT 2019 [2] (linear interpolation within the provided range, starting from the values of shear strength τ_0).
The main results are summarized in Fig. 3.3.17 and compared graphically with the experimental capacity curves. It is worth to note that, regarding the displacements estimation, the elastic deformability of the lateral masonry piers ($1/K_{add,S}$, quantified analytically of the basis of a cantilever static scheme) is added to that of the spandrel, since the displacement transducers monitoring the spandrel distortion in the experimental tests were actually located at the inner corner of the metallic lever beams at the base.

Main data								
l	[mm]	1050	A_G	[mm^2]	3.8	η	[-]	12
t_c	[mm]	30	T_G	[kN]	5.11	α	[-]	2
E_c	[GPa]	10	s	[mm]	66	σ_{0P}	[MPa]	0.33
G_c	[GPa]	4	l_f	[mm]	1050			

		S-R2U	**S-B2U**	**S-B1U**
b	[mm]	1170	1095	1095
d_{eff}	[mm]	80	125	65
b_h	[mm]	111	65	65
b'	[GPa]	1000	845	845
f_{v0}	[MPa]	0.103	0.208	0.248

		S-R2U	S-R2R-1	S-R2R-2
t	[mm]	350	350	350
$f_{m,h}$	[MPa]	1.24	1.24	1.24
τ_0	[MPa]	0.071	0.071	0.071
i	[-]	-	1	2
χ	[-]	-	1.0	1.0
E	[MPa]	1074.2	1931.3	2788.5
G	[MPa]	358.1	700.9	1043.8
K_e	[N/mm]	95097	183181	271117
$K_{add,S}$	[N/mm]	32400	51000	69600
x	[mm]	-	117.4	213.3
M_S	[kNm]	13.3	31.5	56.7
$V_{S,f}$	[kN]	25.4	59.9	108.0 (81.0)*
$V_{S,d}$	[kN]	35.5	52.9	91.6
V_S	**[kN]**	**25.4**	**52.9**	**91.6 (81.0)**
Mode	[-]	Bending	Shear°	Sh. (Bend)
$d_{S,e}$	**[mm]**	**1.05**	**1.33**	**1.65 (1.46)**
$d_{S,u}$	**[mm]**	**16.5**	**32.5**	**32.8 (32.7)**

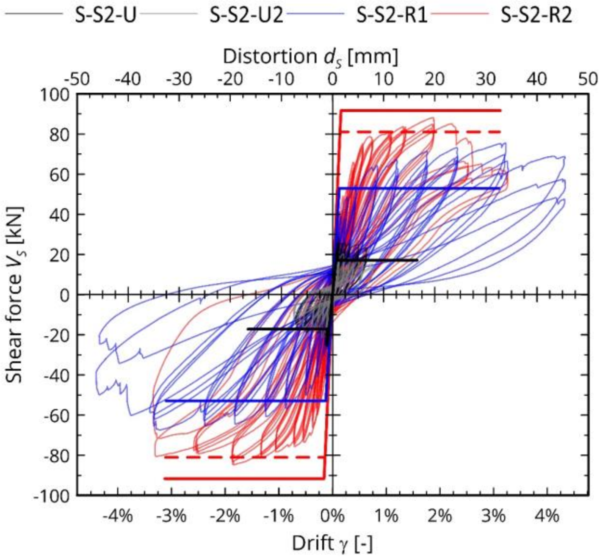

(*) calculated with α=1.5, as "in between" the shear-type and the cantilever scheme, to account grossly for the anomaly in the vertical loading system, as evidenced in §3.3.1.
(°) since $V_{S,f}$ and $V_{S,d}$ are vely close, a combined shear/bending failure is expected.

		S-B2U	S-B2R-1
t	[mm]	250	250
$f_{m,h}$	[MPa]	1.49	1.49
τ_0	[MPa]	0.068	0.068x1.3*
i	[-]	-	1
χ	[-]	-	1.0
E	[MPa]	1335.7	2535.7
G	[MPa]	445.2	925.2
K_e	[N/mm]	77051	157094
$K_{add,S}$	[N/mm]	20500	39100
x	[mm]	-	97.0
M_S	[kNm]	24.2	16.1
$V_{S,f}$	[kN]	46.0	30.7
$V_{S,d}$	[kN]	17.4	35.0
V_S	**[kN]**	**17.4**	**30.7**
Mode	[-]	Shear	Bending°
$d_{S,e}$	**[mm]**	**1.07**	**0.98**
$d_{S,u}$	**[mm]**	**16.6**	**32.3**

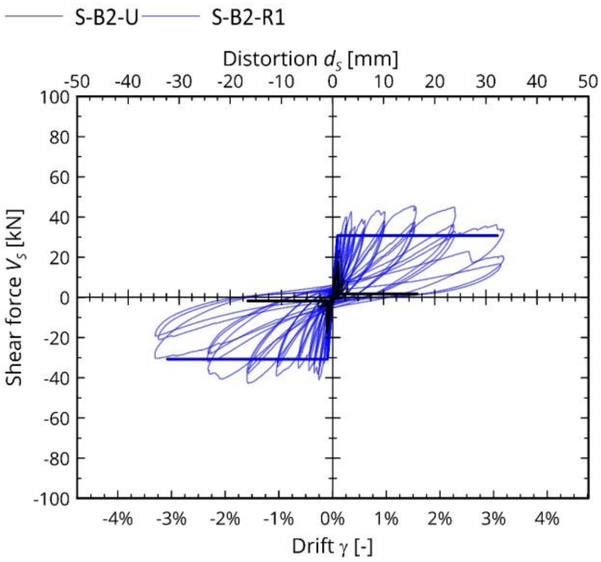

(*) 1.3 is the amplification factor of the shear strength in multiple-leaves roughly-cut stone solid brick masonry, to account for the benefits of effective transversal connectors.
(°) since $V_{S,f}$ and $V_{S,d}$ are vely close, a combined shear/bending failure is expected.

		S-B1U	S-B1R-1
t	[mm]	250	250
$f_{m,h}$	[MPa]	1.92	1.92
τ_0	[MPa]	0.108	0.108
i	[-]	-	1
χ	[-]	-	1.0
E	[MPa]	1638.6	2838.6
G	[MPa]	546.2	1026.2
K_e	[N/mm]	94523	174588
$K_{add,S}$	[N/mm]	25400	43700
x	[mm]	-	77.3
M_S	[kNm]	13.8	16.6
$V_{S,f}$	[kN]	26.2	31.6
$V_{S,d}$	[kN]	27.7	35.5
V_S	**[kN]**	**26.2**	**31.6**
Mode	[-]	Bending°	Bending°
$d_{S,e}$	**[mm]**	**1.31**	**0.90**
$d_{S,u}$	**[mm]**	**16.8**	**32.2**

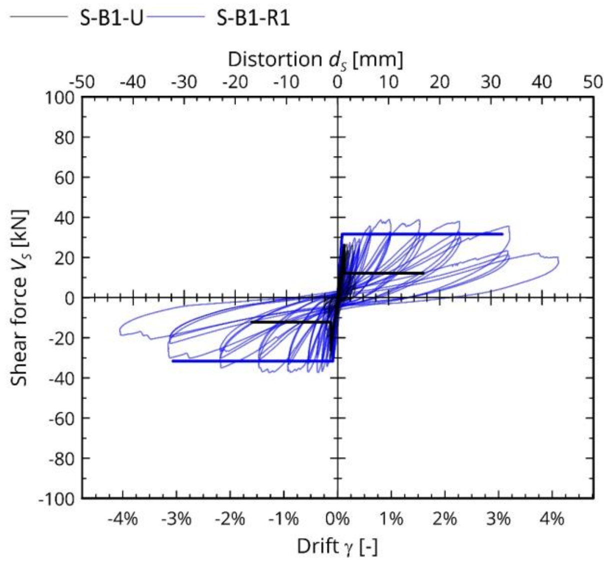

(°) since $V_{S,f}$ and $V_{S,d}$ are vely close, a combined shear/bending failure is expected.

Fig. 3.3.17 Analytic results concerning the masonry spandrel samples and comparison with the experimental behaviour.

3.4. Out-of-plane behaviour

3.4.1. Summary and analysis of the experimental results

The samples of the out-of-plane tests consisted in rectangular masonry panels having a width of 1030 mm and a height of 2480 mm (Fig. 3.4.1). Each specimen was built between a bottom and a top reinforced concrete (RC) beam 250 mm height, 1030 mm long and with a thickness equal to that of the plain masonry. A total of three panels were built and tested (Table 3.7), one for each masonry type: R2, B2 and B1 (Appendix A.). The samples were strengthened with the CRM system applied at one side only. The positioning of the GFRP connectors and of GFRP connectors combined with artificial diatones is schematized in Fig. 3.4.2.

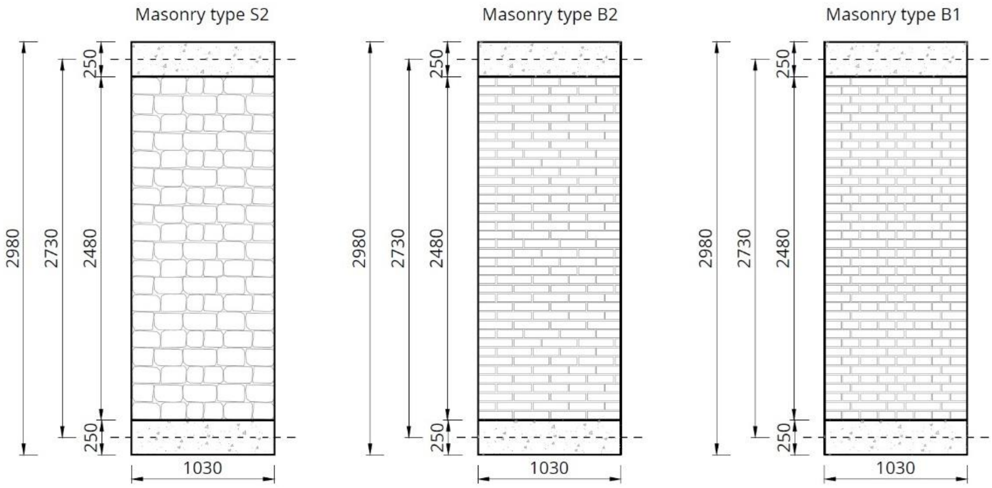

Fig. 3.4.1 Main geometric characteristics of the samples.

Table 3.7: Summary of the CONSTRAIN experimental out-of-plane tests

Sample ID	Masonry type	Strengthening system	Connectors
B-R2	R2	CRM on one-side	GFRP + diatons, 1 side
B-B2	B2	CRM on one-side	GFRP + diatons, 1 side
B-B1	B2	CRM on one-side	GFRP, 1 side

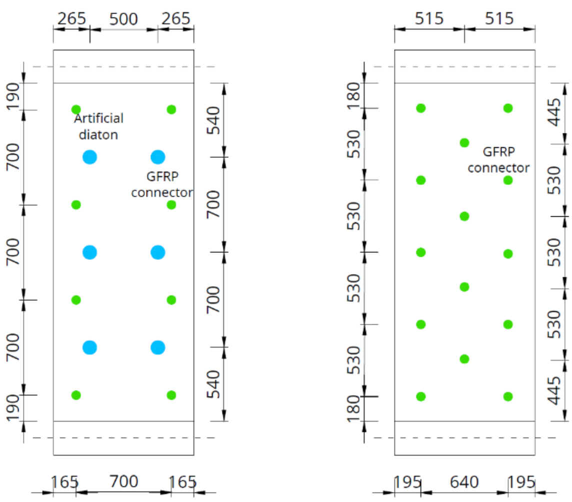

Fig. 3.4.2 Positioning of the connectors in CRM strengthened samples.

The test setup, schematized in Fig. 3.4.3, was a vertical three-point bending test with the samples hinged at the top and bottom. The apparatus was composed of a steel truss reaction frame, four restraining bars, a trolley for the load distribution system and a hydraulic actuator. A smooth horizontal steel bar running through each RC beam allowed to connect to the reaction frame to the wall, by means of the restraining bars provided with knuckle joints. All the samples were arranged so that the CRM-strengthened side was that on the front side. During testing, the actuator, positioned horizontally at the mid-height of the samples, at the rear side, moved a loading trolley to apply the out-of-plane loading cycles at increasing displacements, acting in the positive (pushing from the rear to the front side) and negative (pulling from the front to the rear side) directions and gradually increasing the target amplitude. Each load amplitude was repeated only once before it was increased. When a net deflection equal to 1/100 of the sample height was reached, the test was prosecuted by pushing monotonically.
When pushed, the coating was in tension, simulating the strengthened wall response; when pulled, the coating was in compression, which simulated the unreinforced wall response.
Each specimen was equipped with 13 displacement transducers and two load cells. The displacement transucers were used to measure out-of-plane displacements at the top, middle and bottom of the sample, and rotations of the top and bottom RC elements. Two transducers were placed at the sides of the walls to measure vertical deformations at the mid-height of the pier. The load cells measured the force acting on the wall.

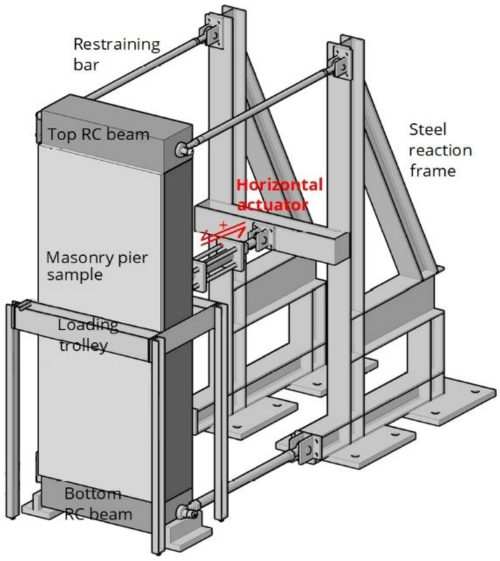

Fig. 3.4.3 Schematization of the test setup for out-of-plane tests.

The behaviour of each sample is described in the following, reporting also monitored loads and displacements and evolution of the crack pattern (surveyed at the front side by means of a Digital Image Correlation system). The main results are then summarized and compared.
The global behaviour of the samples is described in terms of capacity curves, representing the applied horizontal load F_B varying the net horizontal deflection d_B, at the mid-height of the sample.

- Test B-R2 (Fig. 3.4.4)

The first crack occurred at first on the unreinforced side, when pulling, near the mid-height; then also on the strengthened side, when pushing. As the displacement amplitudes increased, the crack pattern on the unstrengthened side remained the same as the single crack opened increasingly more. On the other side, several new horizontal cracks opened on the strengthened side, involving an increasingly wider sample portion. The cracks in the coating multiplied and spread over almost 2/3 of the pier height. The final collapse was due to the tensile failure of the GFRP vertical wires crossing a crack around the mid-span.

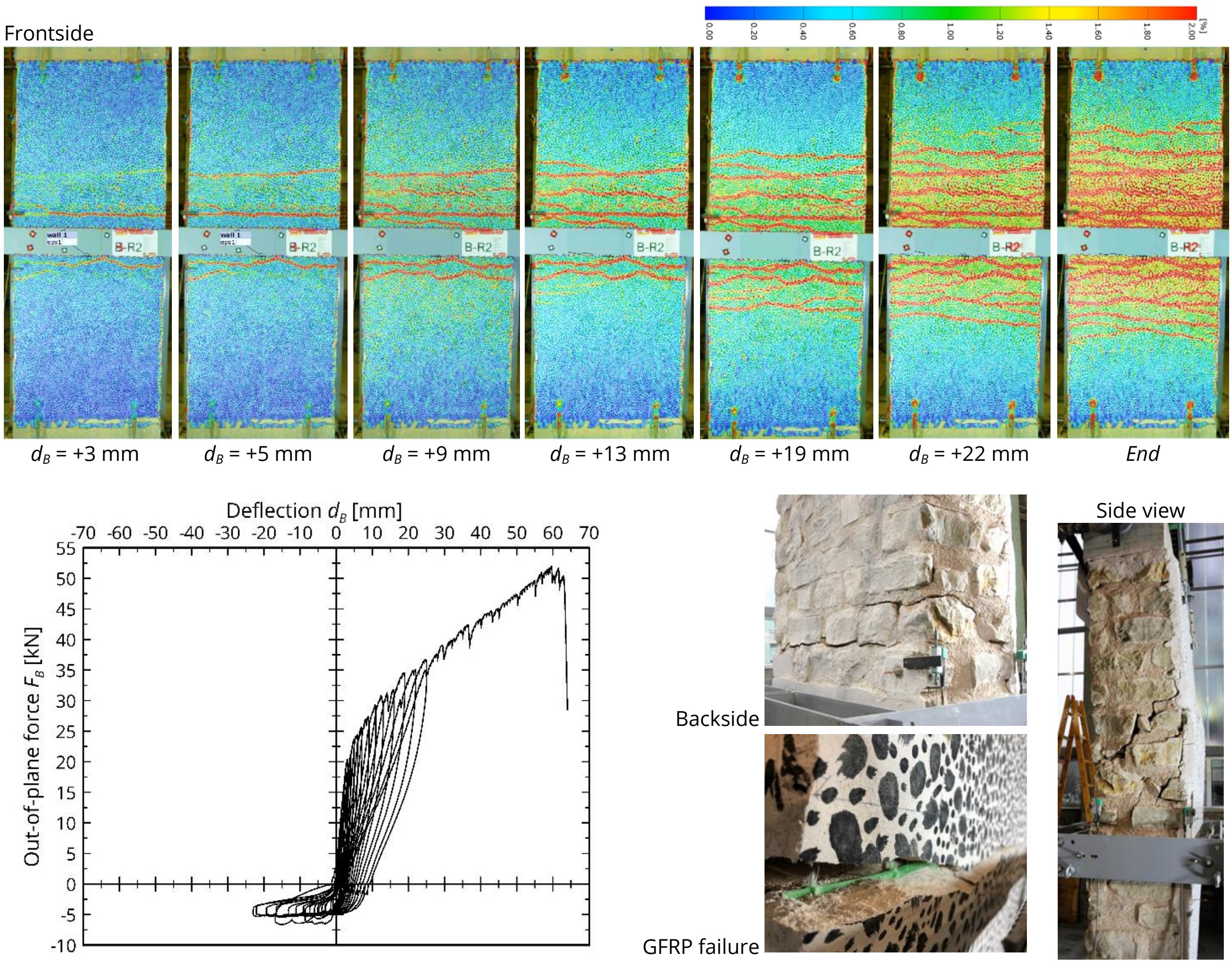

Fig. 3.4.4 Main results of test B-R2.

- Test B-B2 (Fig. 3.4.5)

A single horizontal crack occurred on the unreinforced side, in the middle section, which then gradually opened during the pulling stages. On the coated side, the first crack appeared next to the mid-height and had a sub-vertical trend. As the pushing load increased, new cracks appeared in the coating. All cracks in the coating were primarily horizontal. The cracks originated from the midsection and gradually spread toward the top and bottom of the pier, involving more than 2/3 of the height. At collapse, the GFRP vertical wires in the coating fractured around the mid-span.

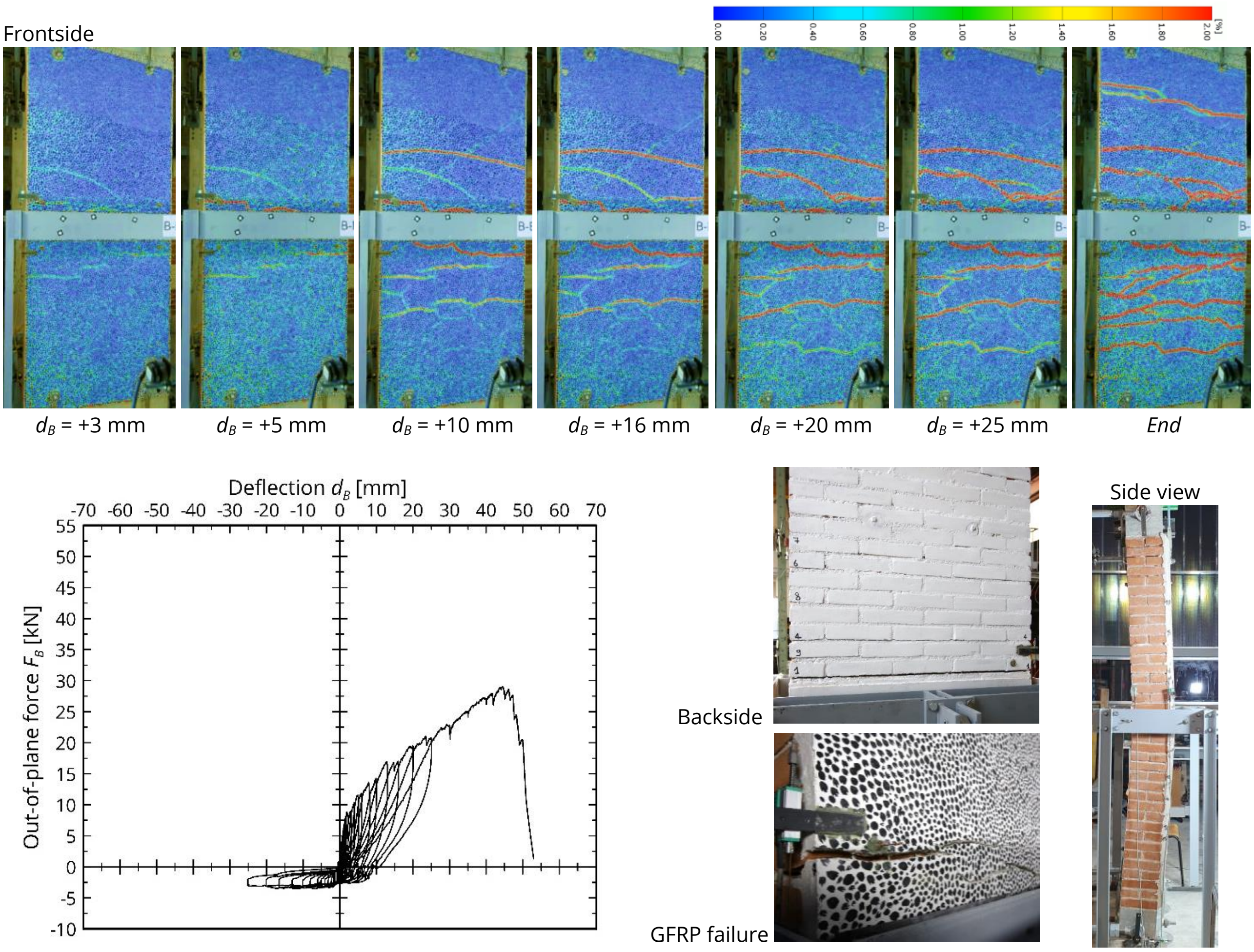

Fig. 3.4.5 Main results of test B-B2.

- Test B-B1 (Fig. 3.4.7)

The first crack appeared when pulling and was horizontal in the mid-height bed joint of the unreinforced side; a second horizontal crack formed slightly upper when the deflection was increased. On the coated side, the first horizontal crack appeared at mid-height. As the pushing load increased, new cracks appeared in the coating. All cracks in the coating were primarily horizontal. The cracks originated from the midsection and gradually spread toward the top and bottom of the pier, involving almost 2/3 of the height. At collapse, the GFRP vertical wires in the coating fractured at the mid-span.

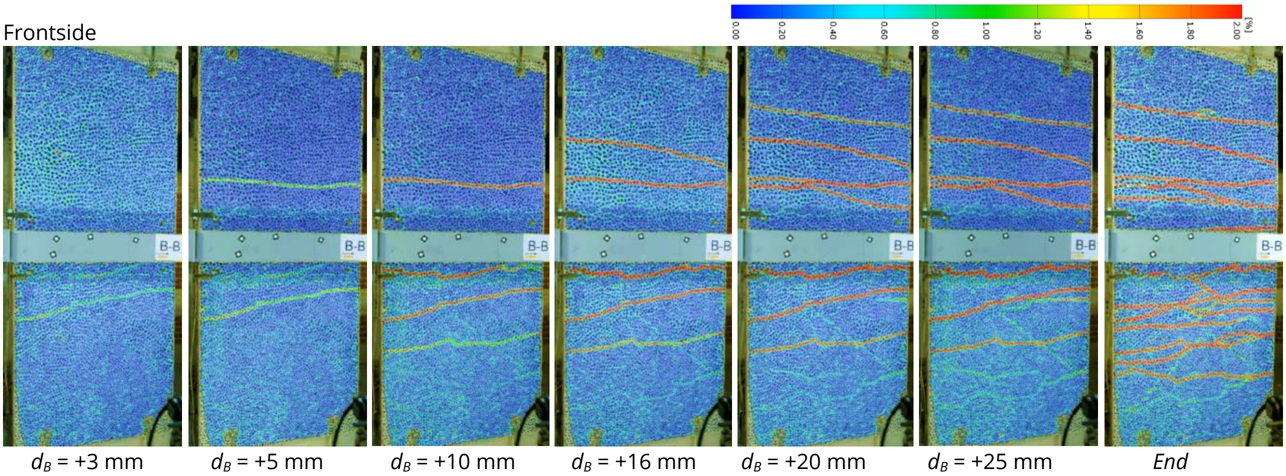

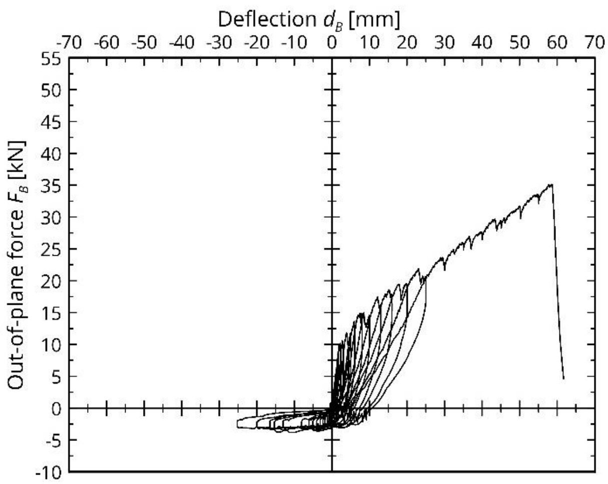

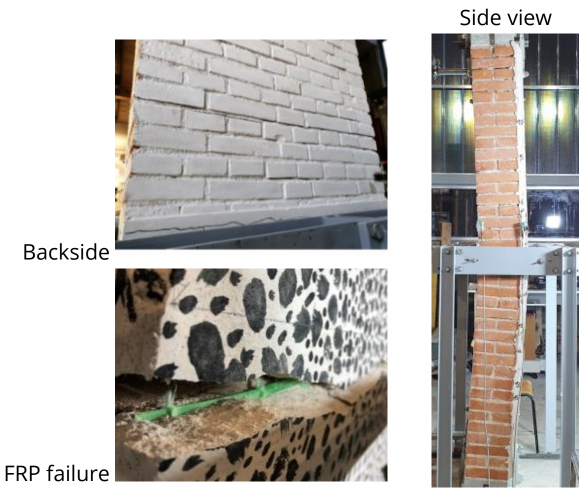

Fig. 3.4.6 Main results of test B-B1.

The values of F_B and d_B obtained from the three experimental tests are summarized in Fig. 3.4.7 and Table 3.8, for first cracking ald ultimate load (*Cr*, *Ul*). When pushing, the ultimate load is taken in correspondance of the peak load; when pulling, the value correspondant to a net deflection equal to 1/150 the height is assumed.
It is observed that the comparison between the sample performances in pushing and pulling directions almost provided a comparison between CRM-strengthened and unstrengthned masonry. In fact, the contribution of CRM in compression is almost negligible (except for the small additional thickness, due to the mortar).

Table 3.8 Values of the out-of-plane horizontal load (F_B) and net deflection (d_B) measured in positive and negative loading directions, for the first cracking and ultimate load.

ID	Side in tension	First cracking (*Cr*)		Ultimate load (*Ul*)	
		F_B [kN]	d_B [mm]	F_B [kN]	d_B [mm]
B-R2	URM	-6.49	-2.81	-5.15	-16.7
	CRM	20.4	3.28	52.0	59.6
B-B2	URM	-3.42	-3.15	-3.43	-16.7
	CRM	8.83	2.25	29.0	44.5
B-B1	URM	-3.37	-3.1	-3.32	-16.7
	CRM	9.80	1.90	35.1	58.6

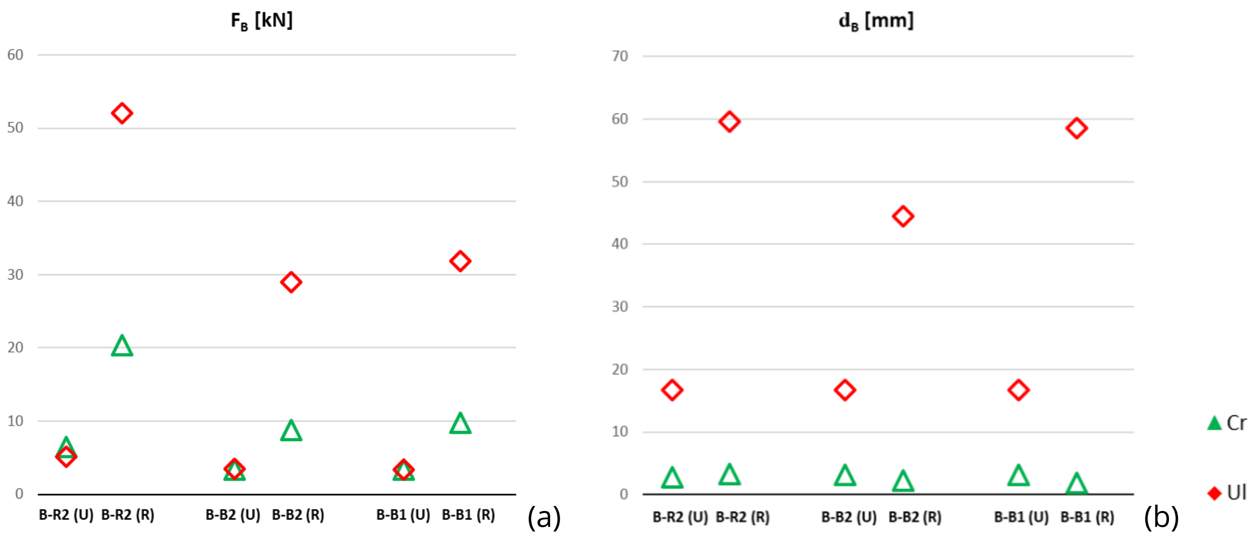

Fig. 3.4.7. Main results of out-of-plane tests: first cracking, peak and near collapse forces (a) and net deflections (b).

In general, on the unstrengthened side, the failure mechanism was characterized by the opening of one or two nearly horizontal cracks in masonry bed joints. Differently, on the strengthened side, many cracks in the coating widely spread from the central section: the CRM and the masonry performed as a composite element.; when the collapse occurred, the vertical GFRP wires fractured due to tension, indicating it was exploited at its maximum.

Significant improvements were attained in terms of resistance (ratio between ultimate forces): 10.1 in B-R2, 8.5 in B-B2 and 10.6 in B-B1. The failure on the fibres occurred at 45.8 times the span in B-R2, 61.4 in B-B2 and 46.6 in B-B1.

3.4.2. Analytic model

Symbols:

t	masonry wall thickness	A_G	net cross section of a GFRP wire
b	masonry wall width	T_G	mean tensile resistance of a GFRP wire
l	masonry wall height	s	GFRP mesh grid pitch
E_m	masonry Young's modulus	$\varepsilon_{lim,G}$	limit tensile strain of GFRP
G_m	masonry shear modulus (~1/3E_m)	E_G	GFRP Young's modulus
t_c	plaster nominal thickness	n_G	number of GFRP wires subjected to tension = 1+*int(b/s)*
E_c	plaster Young's modulus	c	covering of GFRP mesh (typically, = t_c/2)
G_c	plaster shear modulus (~0.4E_c)	f_m	masonry compressive strength
η	coefficient related to the wall static scheme (e.g. 48 for three-point bending)	$f_{c,f}$	plaster flexural strength
I	second bending moment of the uncracked cross section ($bt^3/12$)	α	coefficient of bending moment distribution (e.g. = 4 for three-point bending)
σ_0	mean vertical compressive stress on the wall	α_e	plaster/masonry modular ratio = E_c/E_m
f_{v0}	masonry shear strength for σ_0 = 0 (shove test)	x	depth of the neutral axis of the cracked cross-section

To schematize analytically, in a simplified way, the out-of-plane lateral performances of masonry piers:

- an elastic-plastic behaviour with linear softening can be considered when the unstrengthened masonry is on the tensed side (Fig. 3.4.8a);
- an elastic-plastic behaviour with linear hardening can be considered when the CRM layer is on the tensed e (Fig. 3.4.8b).

To estimate the stiffness, resistance and ultimate displacement capacities, well-known correlations available in the literature can be considered for the unstrengthened masonry side. For CRM strengthened masonry side, the correlations need to be adjusted, so to account for the CRM contribution.

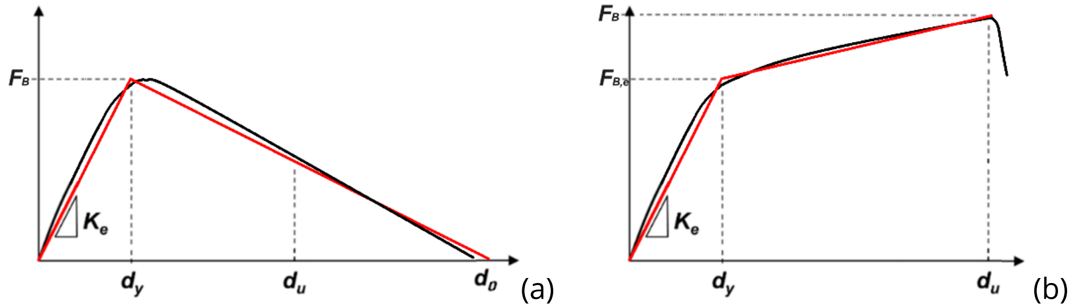

Fig. 3.4.8 Generic, simplified elastic-brittle (a) or elastic-plastic (b) schematization of the out-of-plane performances of masonry walls (red line), in comparison with actual performances (black line).

To evaluate the pier stiffness, K_e, just the flexural deformability can be accounted, as indicated in Eq. (3.18), where a three point bending static scheme is considered. In case of CRM strengthened masonry, equivalent Young modulus shall be considered, evaluating the average values between masonry and mortar coating, weighted on the respective thickness.

$$K_e = \frac{\eta I E}{l^3}. \quad (3.18)$$

Typically, during seismic events, masonry panels subjected to out-of-plane seismic actions exhibit maximum bending moment at the centre of the panel and negligible stresses at the edges (Fig. 3.4.9). Such mechanism is likely to activate in masonry types not prone to disaggregation or leaves-separation phenomena.

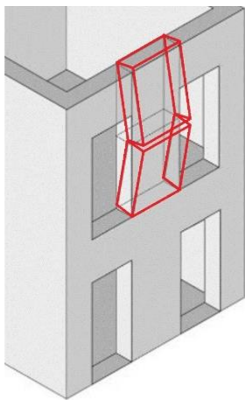

Fig. 3.4.9 Typical out-of-plane failure mechanism of masonry walls.

The wall out-of-plane resistance related to bending, F_B, when the unstrengthened masonry is on the tensed side (suffix U) is mainly due to the masonry compressive resistance and the stabilizing effect of the vertical loads (7.8.2.2.3 in MIT 2018 [3]):

$$F_{B,f(U)} = \frac{\alpha M_{B(U)}}{l} = \frac{\alpha}{l}\frac{\sigma_o b t^2}{2}\left(1-\frac{\sigma_o}{0.85 f_m}\right). \quad (3.19)$$

For this mechanism to activate, the masonry should not prematurely fail in shear in the cracked sections:

$$F_{B,f} \le f_v \cdot b \cdot x \;. \quad \text{with} \quad f_v = f_{v0} + 0.4 \cdot \sigma_0 \,, \tag{3.20}$$

where f_{v0} shall be taken equal to zero, due to cyclic action.

When the CRM layer is on the tension side, the fibre-based composite material (the mesh wires) crossing the cracks, limits their opening, fostering a wider stress diffusion. In the lack of specific guidelines for the evaluation of the resistance of CRM strengthened masonry pier (suffix R), reference is herein made to CNR-DT 215/2018 [4], an Italian guideline available for FRCM strengthening systems, that have several similarities with CRM ones:

$$F_{B,u(R)} = \frac{\alpha M_{B,u(R)}}{l} = \frac{\alpha}{l}\left[0.8x \cdot f_m \cdot b \cdot (y_G - 0.4x) + n_G \cdot A_G \cdot \varepsilon_{\lim,G} \cdot E_G \cdot (t + t_c - c - y_G)\right], \tag{3.21}$$

$$\text{with} \quad x = (\sigma_0 \cdot b \cdot t + n_G \cdot A_G \cdot \varepsilon_{\lim,G} \cdot E_G) / (0.8 \cdot f_m \cdot b)$$

$$\text{and} \quad y_G = \left[\frac{b}{2}(t + t_c)^2 + n_G \cdot A_G \cdot (t + t_c - c)\right] \Big/ \left[b \cdot (t + t_c) + n_G \cdot A_G\right].$$

Basically, $M_{B,u(R)}$ shall be evaluated by analysing a reinforced section subjected to combined compression and bending in cracked conditions, assuming conservation of plane sections, perfect bond among materials, masonry and plaster cracked in tension and plastic in compression, fiber mesh with linear-elastic behaviour in tension until reaching the limit strain. Note that, if the tensile failure of the fibres is attained, the factor $A_G \cdot \varepsilon_{\lim,G} \cdot E_G$ corresponds to the tensile resistance of a single wire, T_G.
The conventional elastic limit force of the bi-linear curve (Fig. 3.4.8b), $F_{B,e(R)}$, can be calculated from the bending moment related to first cracking, $M_{B,e(R)}$:

$$F_{B,e(R)} = \frac{\alpha M_{B,e(R)}}{l} = \frac{\alpha}{l}\left[\frac{b \cdot (t + t_c)^2}{6} \cdot \left(\sigma_0 + \frac{f_{c,f}}{\alpha_e}\right)\right]. \tag{3.22}$$

According to C8.7.1.2.1.6 of MIT 2019 [2], the ultimate out-of-plane deflection of the unstrengthened wall, $d_{Bu(U)}$, corresponds to 60% the displacement for which $F_{B(U)} = 0$ ($d_{B0(U)}$), that is evaluated on the basis of equilibrium analysis of rigid blocks.
For CRM masonry, the ultimate deflection $d_{Bu(R)}$ corresponds to the attainment of the limit strain in tensed GFRP wires. As first attempt, based on experimental evidences, it is taken as $l/50$.

3.4.3. Application and validation

The analytical model described in §3.4.2 is adopted to evaluate the lateral performances of the CONSTRAIN experimental out-of-plane bending tests resumed in §3.4.1.
The mechanical characteristics of the unstrengthened masonry considered in the formulations are those already applied for the masonry piers and spandrels in §3.2.3 and §3.3.3.
To evaluate $d_{B0(U)}$, the contribution of the sample only was considered, as first attempt, thus $d_{B0(U)} = t/3$.
The main results are summarized in Fig. 3.4.10 and compared graphically with the experimental capacity curves.

Main data											
b	[mm]	1030		n_G	[-]	16		η	[-]	48
l	[mm]	2730		A_G	[mm^2]	3.8		α	[-]	4
t_c	[mm]	30		T_G	[kN]	5.11		α_e	[-]	8
E_c	[GPa]	10		s	[mm]	66		$f_{c,f}$	[MPa]	3.0

		B-R2	B-B2	B-B1
t	[mm]	350	250	250
f_m	[MPa]	2.48	2.98	3.84
E_m	[MPa]	1074.2	1335.7	1638.6
E	[MPa]	1931.3	2535.7	2838.6
σ_0	[MPa]	0.034	0.032	0.032
K_e	[N/mm]	21459	11271	12618
y_G	[mm]	~190	~140	~140
$M_{B(U)}$	[kNm]	2.5	1.3	1.3
$M'_{B(U)}$	[kNm]*	3.5	2.3	2.3
$F_{B,f(U)}$	**[kN]**	**5.2**	**3.3**	**3.3**
$d_{B,e(U)}$	**[mm]**	**0.24**	**0.30**	**0.26**
$d_{B,e(U)}$	**[mm]**	**70.0**	**50.0**	**50.0**
$x_{(C)}$	[mm]	46.6	37.0	28.7
$M_{B(C)}$	[kN]	30.6	21.6	21.9
$M'_{B(C)}$	[kN]*	31.6	22.6	22.9
$F_{B,f(C)}$	**[kN]**	**46.3**	**33.1**	**33.6**
$M_{B,e(C)}$	[kN]	8.84	4.02	4.84
$M'_{B,e(C)}$	[kN]*	9.84	5.02	5.84
$F_{B,e(C)}$	**[kN]**	**14.4**	**7.4**	**8.6**
$d_{B,e(C)}$	**[mm]**	**0.67**	**0.65**	**0.68**
$d_{B,u(C)}$	**[mm]**	**54.6**	**54.6**	**54.6**

(*) evaluated by adding to M_B the additional contribution due to the friction of the testing apparatus (approximately 1 kNm)

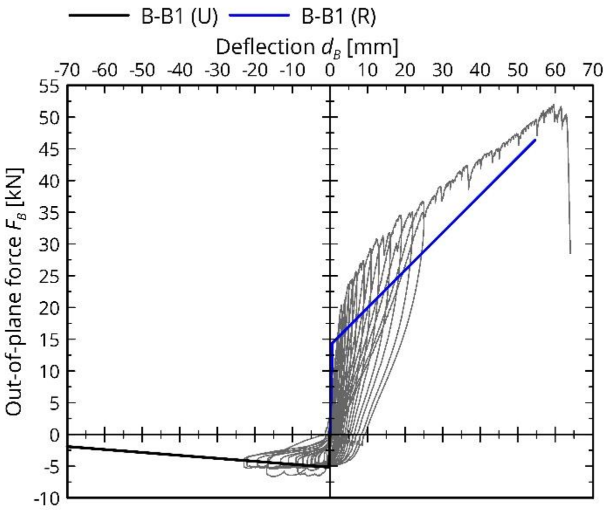

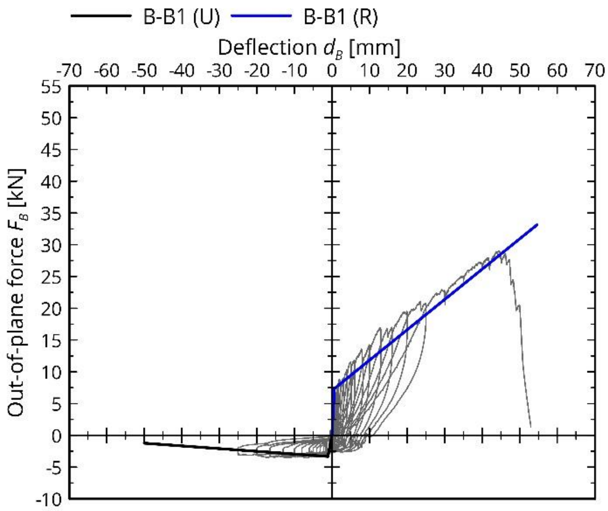

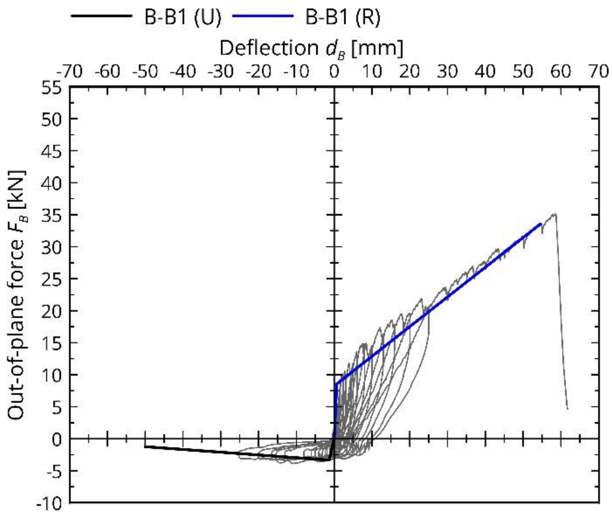

Fig. 3.4.10 Analytic results concerning the out-of-plane tests and comparison with the experimental behaviour.

4. Roof ring beams with FRP meshes embedded in bed joints

4.1. Technique characteristics

The technique can be generally adopted for the reconstruction of the roof masonry ring beams by embedding FRP pre-formed meshes in the bed joints (Fig. 4.1.1), so to improve the out-of-plane response of the walls and foster the global, box-like behaviour of the masonry structure, contrasting overturning phenomena. It is observed that the intervention is also capable of improving the in-plane performances of the upper masonry spandrels.
In particular, Glass fibres meshes are herein considered (GFRP). The main characteristics for the components materials adopted in the "CONSTRAIN" tests are resumed in Appendix A.

Fig. 4.1.1 Reconstruction of the roof masonry ring beams FRP meshes embedded in bed joints

4.2. Out-of-plane behaviour

4.2.1. Summary and analysis of the experimental results

The masonry ring beam samples with GFRP meshes embedded in the bed joints ("T") were 3500 mm long. The first sample was made of 350 mm–thick double-leaf rubble stone masonry ("T-R2"), which was 660 mm tall and had four reinforced bed joints (Fig. 4.2.1a). The other sample was made of 250 mm-thick single-leaf solid clay brick masonry ("T-B1") that was 465 mm tall, with six reinforced bed joints (Fig. 4.2.1b).

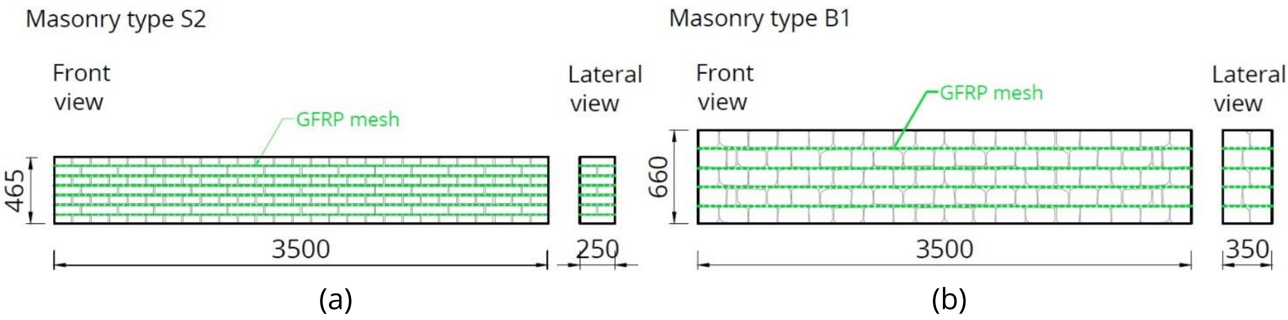

Fig. 4.2.1 Main geometric characteristics of the roof ring beam masonry samples: (a) T-R2 and (b) T-B1.

The setup was composed of the horizontal sliding system (supporting the sample vertically), the horizontal restraining system, and the loading system. The sliding system consisted of a smooth, flat surface covered with two plastic sheets with grease in between. The restraining system comprised four stiff steel columns connected to the laboratory basement (two at each side), which was connected to the sample with hinged rods that provided support against out-of-plane horizontal sliding, but allowed rotations. The net span between the supports was 3000 mm. The loading system was a horizontal actuator located at the midspan of the sample and connected on one side to a concrete ballast and on the other to a steel frame on a trolley. The load was applied cyclically, alternatively pulling (negative loading) and pushing (positive loading), gradually increasing the amplitude of the deflection.

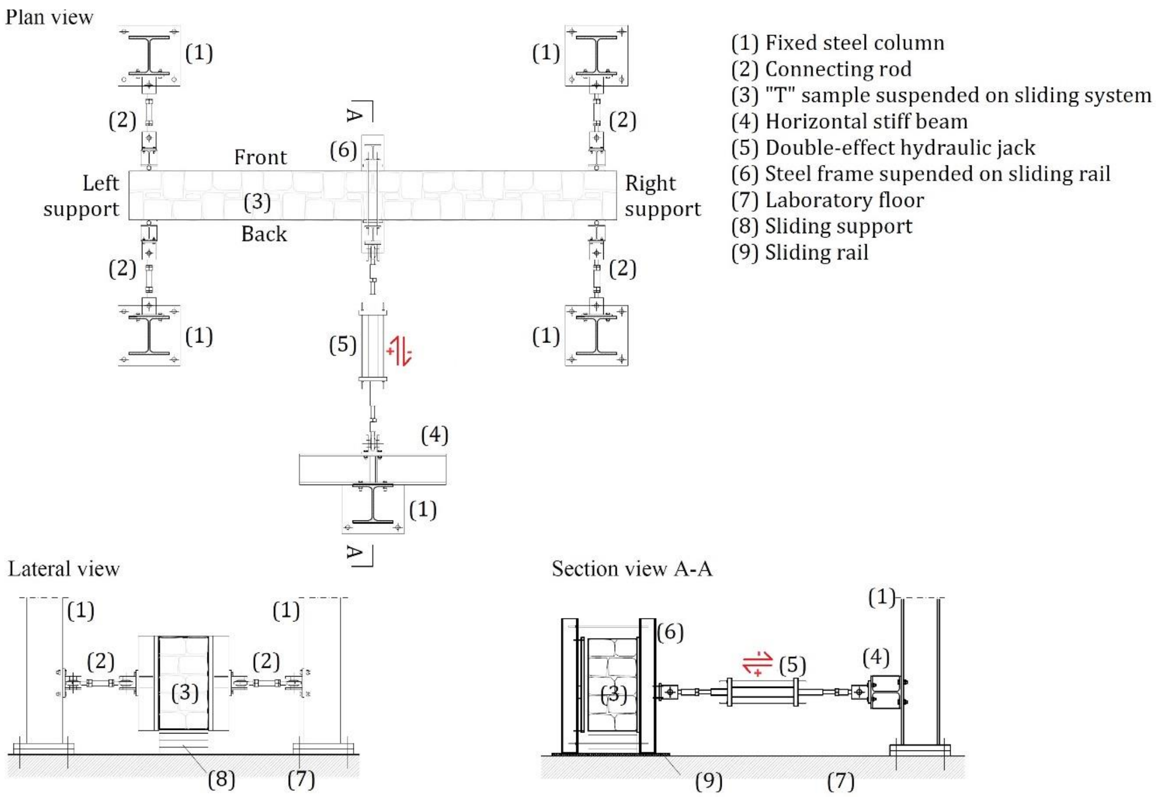

Fig. 4.2.2. Experimental setup for "T" samples.

The main results are summarized in the following, reporting also monitored loads and displacements and evolution of the crack pattern (visual surveyed during the test).
The global behaviour of the samples is described in terms of capacity curves, representing the out-of-plane horizontal load, F_T, varying the net horizontal deflection at the midspan, d_T.

- Test T-R2 (Fig. 4.2.3)

A first pair of central cracks opened on the rear face, when pulling, and just after of the front face, inversing the load direction. The cracks followed an almost vertical trend along the mortar joints. With increasing load, the deflection increased, and new sub-vertical cracks formed. The cracks progressively formed alternately at front and back, according to the loading direction. When the number of cracks stabilized, a gradual and significant widening of the central cracks emerged at increasing deflection. The collapse was due to the fracture of the GFRP longitudinal wires near the back side, when pulling, and then near the front side, when pushing. The behaviour was almost symmetric in the two directions.

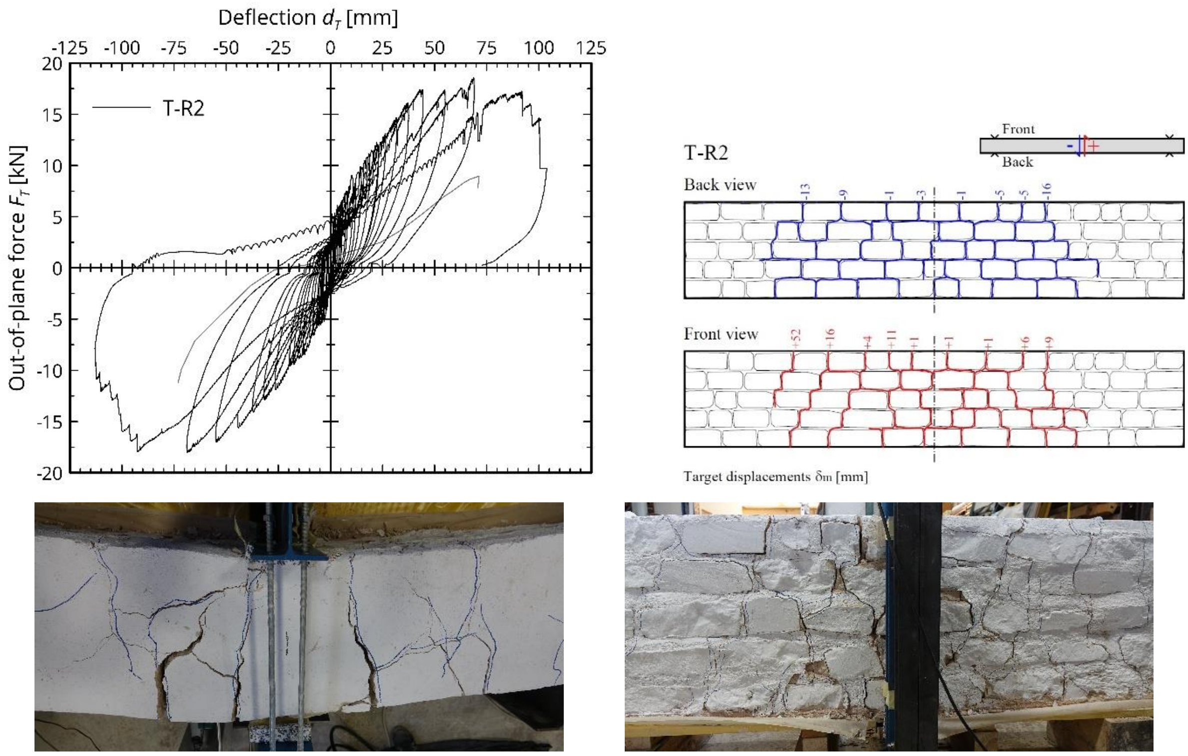

Fig. 4.2.3 Main results of test T-R2.

- Test T-B1 (Fig. 4.2.4)

A first pair of cracks formed in the vicinity of the midspan, when pushing. The cracks were vertical but followed the joints at the front side. As the load direction was inversed, the cracks on the front side closed, and the cracks on the back side opened. With increasing load, the new sub-vertical cracks (following the joints) developed almost throughout the whole sample height, gradually covering an increasingly wider portion of the sample. Once the formation of most of the cracks was completed, the existing cracks widened with the deflection increase. Near the ultimate state, a continuous horizontal discontinuity at the upper bed joint caused a gradual separation of the last brick row from the lower part of the sample on the left side; thus, the last layer of reinforcement mesh lost part of its effectiveness. At the test prosecuted, some longitudinal GFRP wires on the rear face fractured at the mid-span; similarly, at the opposite loading direction, the GFRP wires on the front face fractured at the mid-span. The behaviour was quite asymmetric in the two loading directions (the hardening was stiffer in pulling).

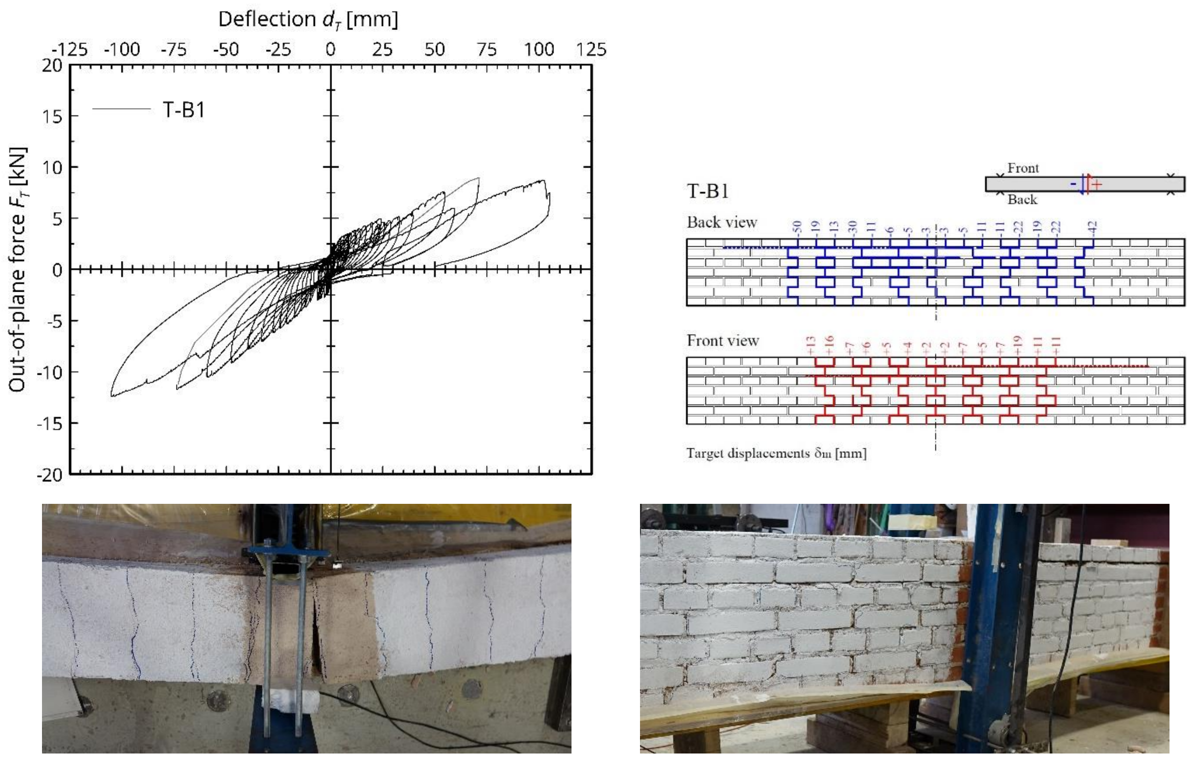

Fig. 4.2.4 Main results of test T-B1.

Generally, the first cracks in the masonry formed on the tensed side, in the vicinity of the midspan. As the load direction was inversed, the cracks on one side closed, and the cracks on the other side opened. With increasing load, new sub-vertical cracks developed on the tensed side, almost throughout the whole sample height, gradually covering an increasingly wider portion of the sample (of a width of about 1800 mm). Moreover, as the deflection increased, the existing cracks widened. Both sample attained to peak load just before some longitudinal GFRP wires fractured on the tensed side, at the mid-span; then the load rapidly dropped down. The backbone of the load-deflection F_T–d_T curves assumed a roughly tri-linear trend: the first elastic part with an initial stiffness, a second plastic part with hardening, and a third part with near-zero stiffness.
The main results of the two tests in terms of load and deflection at first cracking (*Cr*) and at collapse (*Ul*) are summarized in Table 4.1 and Fig. 4.2.5. For sample T-R2, the resistance of almost 18.3 kN at about 1/44 of the net span for both directions. Sample T-B1 reached 12.4 kN and 9.0 kN in pulling and pushing, respectively; the difference was likely influenced by the detachment of the upper rows mentioned before. However, the ultimate deflections were similar (about 1/29 the net span).

Table 4.1. Main results of tests on masonry ring beams with FRP meshes embedded in bed joints, in terms of load and deflection at first cracking (Cr) and at collapse (Ul).

		First cracking (*Cr*)		**Ultimate load (*Ul*)**	
Sample	**Load direction**	**F_T [kN]**	**d_T [mm]**	**F_T [kN]**	**d_T [mm]**
T-R2	Pull (−)	−2.3	−1.0	−18.0	−68.8
	Push (+)	+5.2	+0.8	+18.6	+69.0
T-B1	Pull (−)	−3.1	−2.7	−12.4	−105.1
	Push (+)	+2.6	+2.3	+9.0	+101.9

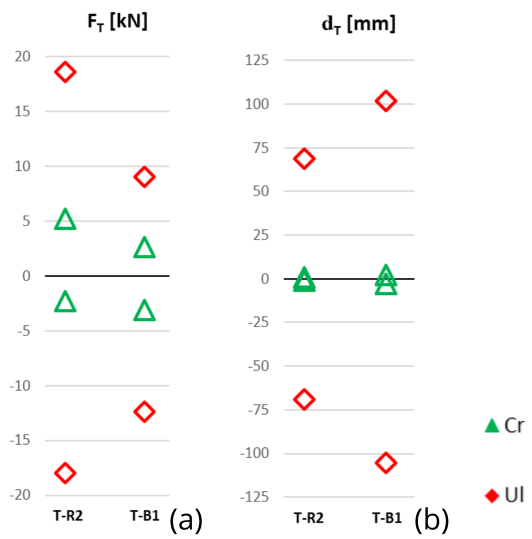

Fig. 4.2.5 Main test results of "T" samples: first cracking and ultimate force (a) and deflection (b) values

The cyclic tests allow also to draw the trends of the cycle stiffness, K_T (evaluated as the slope of the peak-to-peak line within each loop of the F_T–d_T curve) by varying the net deflection d_T (Fig. 4.2.6a). The stiffness degradation with increasing deflection shows an approximately power-law trend; at the end of the tests, the cycle stiffness was less than 10% the initial value.
The cumulative input energy (E_{in}) and the dissipated hysteretic energy (E_{hys}) were quantified (Fig. 4.2.6b), as well as the E_{hys}/E_{in} ratios (Fig. 4.2.6c). E_{in} is the cumulative work to deform the sample from the beginning of the test to a specific target value of deflection. For each loading cycle, it corresponds to the area under the positive and negative branches of the hysteretic loop of the F_T-d_T graph. Similarly, the cumulative dissipated hysteretic energy E_{hys} is the sum of all the areas included in the hysteretic loops. Moreover, an approximate estimation of the equivalent hysteretic damping with varying target displacement was performed (Fig. 4.2.6d).
In respect to the first cracking condition, the cumulative dissipated energy at collapse resulted more than 500 times greater in both cases. The damping ratio, ξ_{hys}, decreased as the deflection progressed and resulted about 11-12% at collapse.

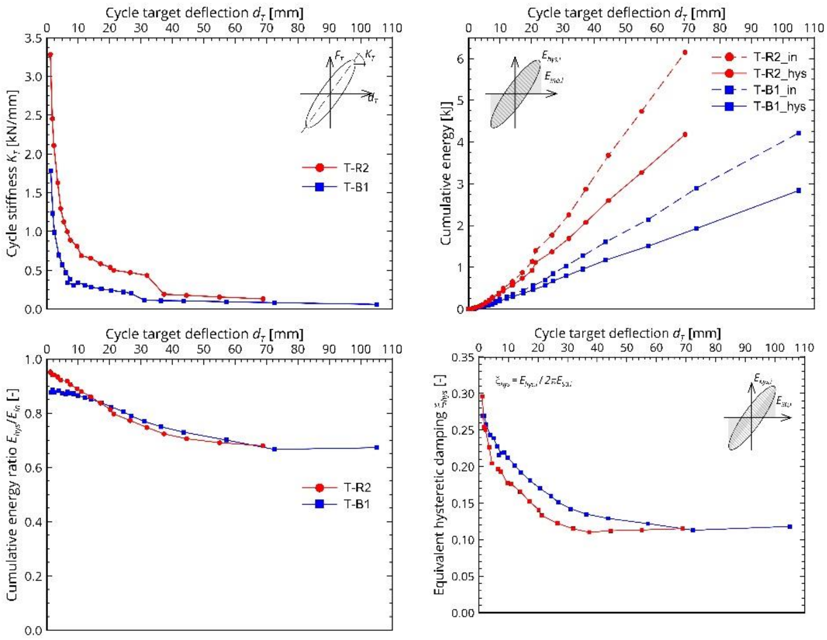

Fig. 4.2.6. Roof ring beam stiffness and energy characteristics, varying the cycle target deflection d_T.

4.2.2. Analytic model

Symbols:

t	masonry beam thickness	E_G	GFRP Young's modulus
b	masonry beam height	n_G	total number of GFRP wire levels in a single bedjoint
l	Masonry beam span	n'_G	number of GFRP wire levels in tension in a single bedjoint
E_m	masonry Young's modulus	c	covering (distance between the outer GFRP wires and the tensed edge of the cross section
η	coefficient related to the beam static scheme (e.g. =48 for 3 point bending)	$f_{m,f}$	masonry flexural strength (horizontal mending)
I	second bending moment of the uncracked beam cross section ($tb^3/12$)	α	coefficient of bending moment distribution (e.g.=4 for 3 point bending)
A_G	net cross section of a GFRP wire	α_G	GFRP/masonry modular ratio = E_G / E_m
n_B	number of bed joints with GFRP embedded		
T_G	mean tensile resistance of a GFRP wire		
s	GFRP grid pitch		
$\varepsilon_{lim,G}$	limit tensile strain of GFRP		

To schematize analytically, in a simplified way, the out-of-plane lateral performances of masonry beams with GFRP mesh embedded in the bed joints a tri-linear behaviour with final plastic stage can be considered (Fig. 3.4.8).

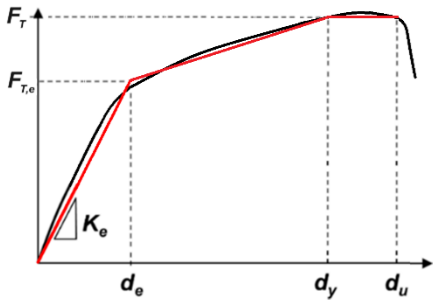

Fig. 4.2.7 Generic, simplified tri-linear schematization of the out-of-plane performances of masonry beams with GFRP meshes embedded in the bed joints (red line), in comparison with actual performances (black line).

To evaluate the beam stiffness, K_e, just the flexural deformability of the masonry can be accounted, as indicated in Eq. (4.1):

$$K_e = \frac{\eta I E_m}{l^3} \qquad (4.1)$$

Typically, during seismic events, masonry roof ring beams subjected to out-of-plane seismic actions exhibit maximum bending moment at the centre of the span. Such mechanism is likely to activate in masonry types not prone to disaggregation or leaves-separation phenomena.

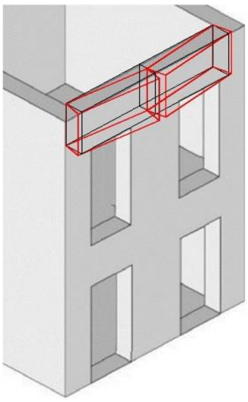

Fig. 4.2.8 Typical out-of-plane failure mechanism of masonry ring beams.

In masonry beams with GFRP meshes embedded in the bed joints, the out-of-plane resistance, $F_{T,u(R)}$, shall be evaluated by analysing a reinforced section subjected to bending in cracked conditions, assuming conservation of plane sections, perfect bond among materials, masonry cracked in tension and plastic in compression, fiber mesh with linear-elastic behaviour in tension until reaching the limit strain.

$$F_{T,u(R)} = \frac{\alpha M_{Tu(R)}}{l} = \frac{\alpha}{l} \frac{\varepsilon_{\lim,G} \cdot E_G \cdot I_{id}}{\alpha_G \left(t - c - x_{id}\right)} \tag{4.2}$$

with $\quad x_{id} = \frac{\alpha_G \cdot n_B A_G \cdot n'_G}{b} \left(-1 + \sqrt{1 + \frac{2b \cdot (t-c) - b s \cdot (n'_G - 1)}{\alpha_G \cdot n_B A_G \cdot n'_G}} \right)$ and

$$I_{id} = \frac{b \cdot x_{id}^3}{3} + \alpha_G \cdot n_B A_G \cdot n'_G (t - c - x_{id})^2 - \alpha_G \cdot n_B A_G \cdot s\,(t - c - x_{id})\,(n'_G - 1)\, n'_G + \alpha_G \cdot n_B A_G \cdot s^2 \;(2n'_G - 1)(n'_G - 1)\, n'_G / 6$$

Since n'_G is unknown, a first attempt value corresponding to the total number of wire levels n_G can be set, and equilibrium calculated. If the calculated neutral axis, x_{id}, is compatible with the assumption, the result is correct; otherwise, the procedure continues iteratively by reducing n'_G until a good solution is found.
Note that, if the tensile failure of the fibres is attained, the factor $\varepsilon_{\lim,G} \cdot E_G$ corresponds to the tensile strength of the wires, T_G/A_G.
The conventional elastic limit force of the bi-linear curve (Fig. 3.4.8), $F_{T,e(R)}$, can be calculated from the bending moment related to the masonry first cracking, $M_{T,e(R)}$:

$$F_{T,e(R)} = \frac{\alpha M_{T,e(R)}}{l} = \frac{\alpha}{l} \frac{b \cdot t^2}{6} \cdot f_{m,f} \,. \tag{4.3}$$

Note that the contribution of the reinforcement is neglected. This is likely the resistance of the unstrengthened masonry beam.

For GFRP reinforced masonry, the deflection d_y, based on the experimental evidences, it is taken as $5 * l/t$, and $d_u = 1.5 * d_y$.

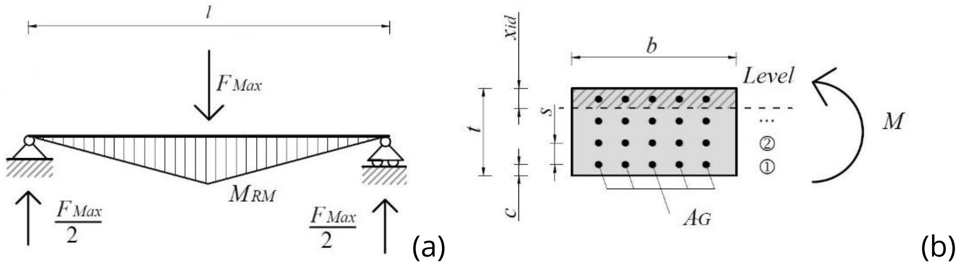

Fig. 4.2.9 "T" samples: (a) static scheme assumed for the evaluation of the ultimate and first cracking load and (b) schematisation of the reinforced masonry cross-section.

4.2.3. Application and validation

The analytical model described in §4.2.2 is adopted to evaluate the lateral performances of the CONSTRAIN experimental out-of-plane bending tests of masonry ring beams resumed in §4.2.1. The mechanical characteristics of masonry and GFRP wire considered in the formulations are those already applied in §3.2.3, §3.3.3 and §3.4.3. The values of $f_{m,f}$ are calculated from the average first cracking load measured in the CONSTRAIN experimental tests on the ring beams, solving Eq. (4.3) for $f_{m,f}$.

The main results are summarized in Fig. 4.2.10 and compared graphically with the experimental capacity curves.

Main data						
l	[mm]	3000		E_G	[MPa]	72816
η	[-]	48		T_G	[kN]	5.11
α	[-]	4		A_G	[mm^2]	3.8
				s	[mm]	66

		T-R2	**T-B1**
t	[mm]	350	250
b	[mm]	660	465
E_m	[MPa]	1074.2	1638.6
$f_{m,f}$	[MPa]	0.235	0.442
n_b	[-]	4	6 (5*)
n_G	[-]	5	4
n'_G	[-]	4	3
c	[mm]	43	26
K_e	[N/mm]	4503	1764
$M_{T,e}$	[kNm]	3.17	2.14
I_{id}		1.52.E+8	4.5(3.84*) E+7
x_{id}	[mm]	45.1	33.7 (31.3*)
$M_{T,u(R)}$	[kN]	11.5	10.2 (8.6*)
$F_{T,e}$	**[kN]**	**4.22**	**2.85**
$F_{T,u(R)}$	**[kN]**	**15.4**	**13.6 (11.5*)**
$d_{T,e(R)}$	**[mm]**	**0.94**	**1.62**
$d_{T,y(R)}$	**[mm]**	**42.9**	**60.0**
$d_{T,u(R)}$	**[mm]**	**64.3**	**90.0**

* Assuming the ineffectiveness of the GFRP mesh in the upper bedjont

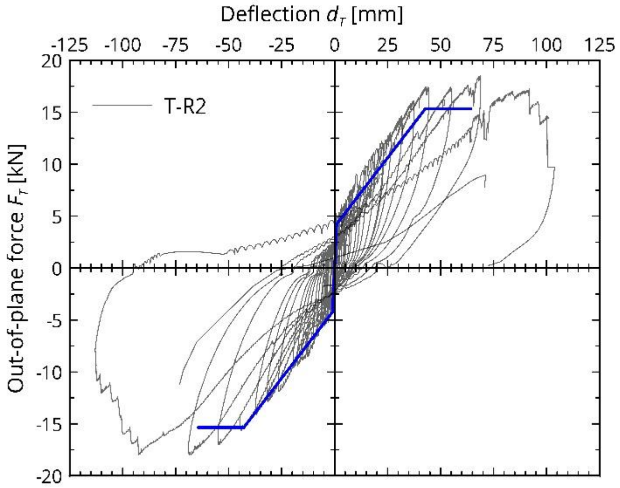

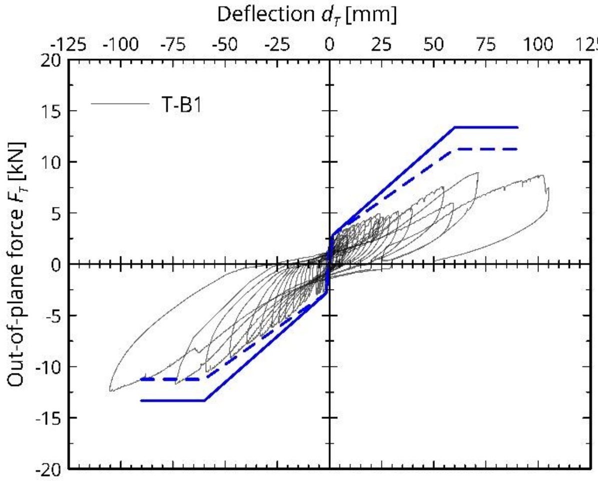

Fig. 4.2.10 Analytic results concerning the out-of-plane tests and comparison with the experimental behaviour.

5. Ring beams with externally-bonded FRP strips

5.1. Technique characteristics

The technique can be generally adopted to improve the out-of-plane response of masonry walls and foster the global, box-like behaviour of the masonry structure. It consists of bonding Fibre–Reinforced Polymer (FRP) strips onto the outer surface of the masonry ring beams in a building (Fig. 5.1.1). Being an eccentric system (since FRP is on only one side), the continuity of the strip around the corner is crucial.

It is observed that the intervention is also capable of improving the in-plane performances of the masonry spandrels, since a horizontal tensile-resistant element in introduced.

In particular, unidirectional Carbon fibres strips are herein considered (CFRP). To apply the strips, the masonry surface was first levelled by applying a flat and smooth layer of a rapid-setting, thixotropic cementitious grout. Then, a first layer of epoxy resin was spread and the strip was applied; on top of the strip, a new layer of epoxy resin was spread. The main characteristics for the component materials adopted in the "CONSTRAIN" tests are resumed in Appendix A.

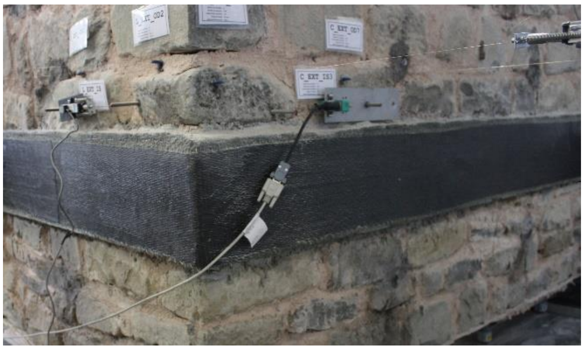

Fig. 5.1.1 CFRP strip externally bonded on a masonry ring beam.

5.2. Out-of-plane behaviour

5.2.1. Summary and analysis of the experimental results

The samples for testing the masonry ring beams with externally bonded FRP strips were C-shaped masonry samples ("C") and had nominal dimensions of 3650×1035 mm^2 (l×b = central span × side, measured along the axes) and height h = 1000 mm. The first sample ("C-R2") was made of 350 mm–thick double-leaf rubble stone masonry and the other ("C-B1") of 250 mm-thick single-leaf solid clay brick masonry. A 200 mm–wide CFRP strip was bonded externally to each sample at mid-height around the outer perimeter, rounding the corners with a bend radius of 20 mm. In the double-leaf rubble stone sample, transversal connectors (i.e "artificial diatones", as those described in section 3) were added to prevent leaves separation in the masonry.

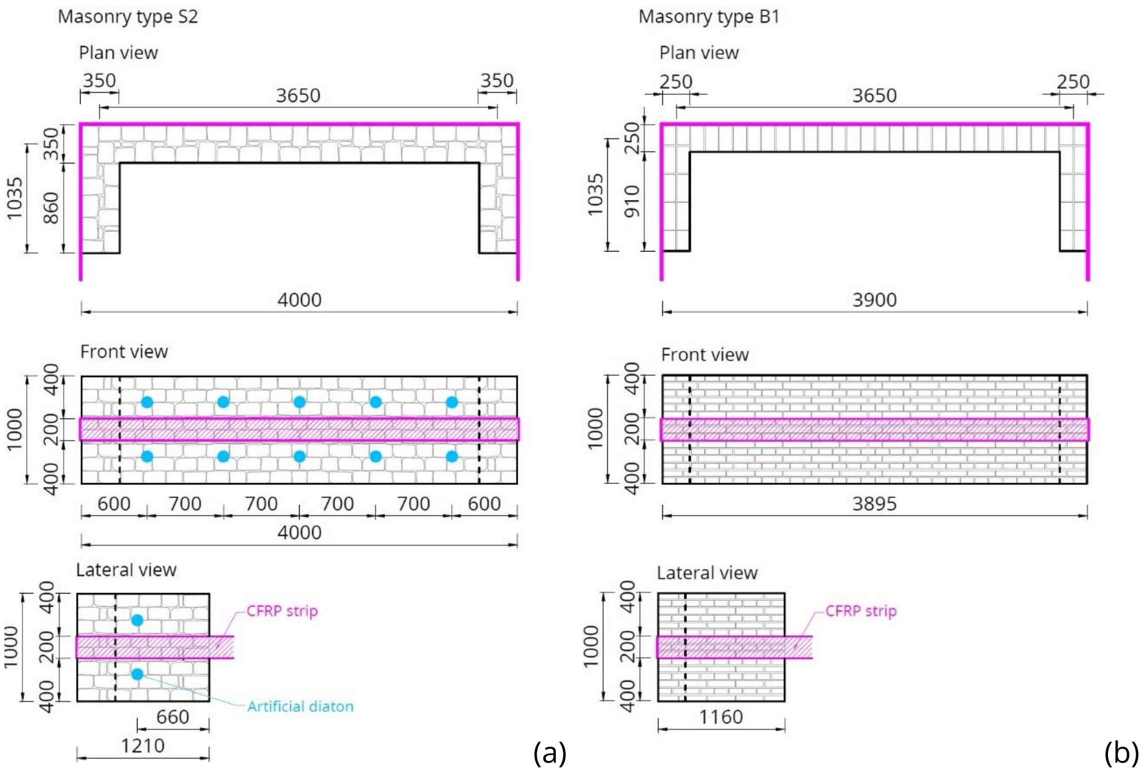

Fig. 5.2.1 Main geometric characteristics of the C-shape masonry samples: (a) C-R2 and (b) C-B1.

The test setup for the "C" samples is schematized in Fig. 5.2.2. Each sample laid on six trolleys, which moved on the smooth horizontal surface with minimal friction. The out-of-plane horizontal cyclic loading was applied at the midspan using a hydraulic jack. The ends of the sample wings were clamped to a reaction wall (fixed concrete ballast) via supports capable to prevented rotation about vertical axis but to allow lateral movement. The CFRP strips were anchored into the supports (by clamping), thus fixing the axial movement of the sample (in the direction of the loading) when the actuator was pushing. In the case when the actuator was pulling the sample, the wings pressed against a vertical steel beam.

The load was applied cyclically, alternatively pushing (positive loading) and pulling (negative loading), gradually increasing the amplitude of the deflection. When the CFRP strip at the midspan failed during pushing, the test was stopped, and the reinforcement continuity was restored just to prevent the separation of the two wall portions (no other influence on negative loading). Then, the test was restarted by pulling monotonically to induce the failure of the CFRP strip at the corners.

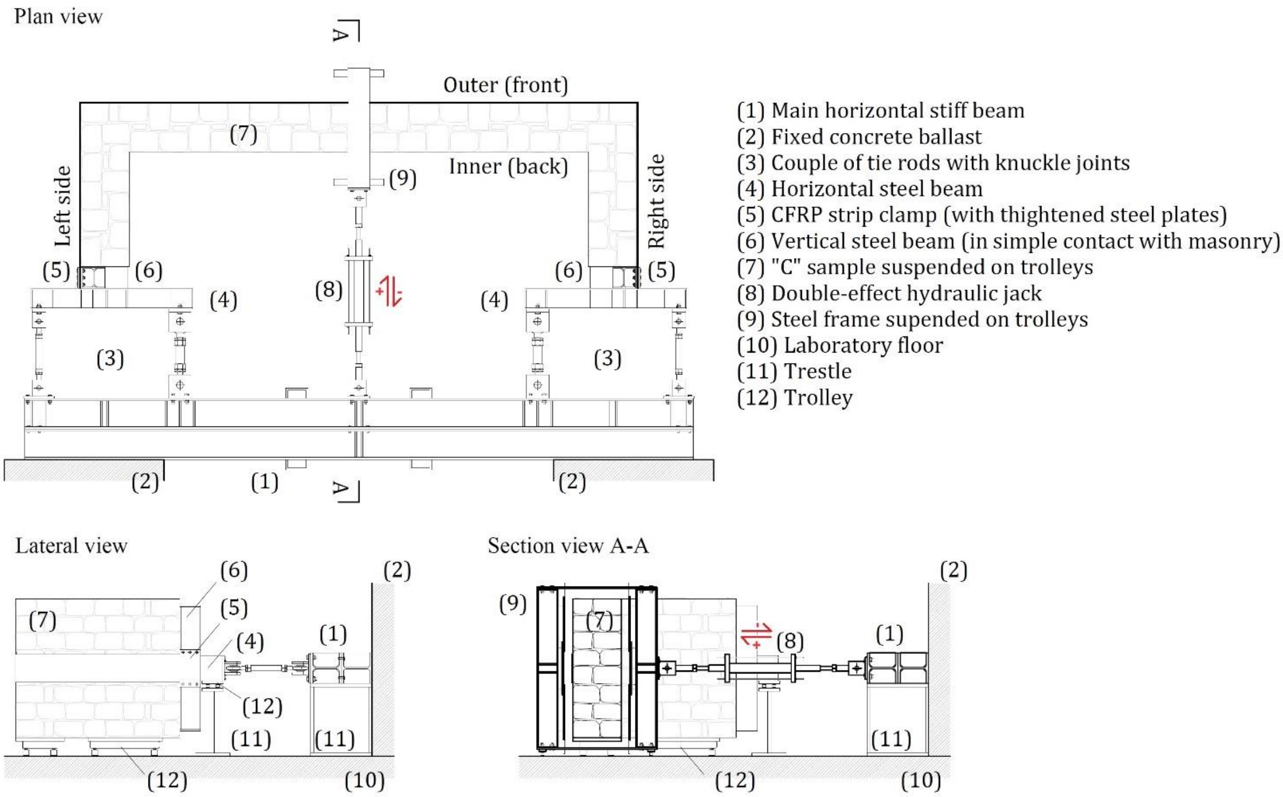

Fig. 5.2.2 Experimental setup for "C" samples. The instrumentation is shown in the plan view.

The main results are summarized in the following. The global behaviour of the samples is described in terms of capacity curves, representing the out-of-plane horizontal load, F_C, varying the net horizontal deflection at the midspan, d_C.
Besides the deflection, the relative opening of the midspan crack (inner side, w_i, and external side, w_e) was monitored. Horizontal displacements at the wing extremities were also surveyed (left wing, h_L, and right one, h_R). In addition, pairs of displacement transducers were installed on the outer side of the wall, near the corners, enabling the survey of the corner rotations θ.

- Test C-R2 (Fig. 5.2.3)

The first sub-vertical cracks occurred at midspan and located at the outer side, when pushing, while at the inner side, when pulling, once the flexural tensile strength of the masonry parallel to the bed joint was attained. In the former case, the load did not drop, owing to the CFRP strip; conversely, in the latter, it dropped down and later increased again. The stiffness reduction was significant in both cases but more pronounced when pulling. The progressive deflection in the pushing direction led to the onset of CFRP debonding at the midspan and to the opening of other nearly vertical cracks on the outer masonry surface (about 500 mm from the midspan). Finally, the tensile fracture failure of the CFRP strip in the vicinity of the midspan occurred. Looking the fractured reinforcement, it is observed that some local delamination of occurred just around the crack: it involved both the GFRP-grout and the grout-masonry interfaces.
The test then proceeded monotonically in the pulling direction and induced the anticipated fracturing of impregnated fibers at the right clamp. This was likely caused by local stress concentration in the fibers due to rotation of the clamped supports, which might have aggravated the local weakening of the fibers. The fracturing caused a partial load decrease. Then, as the load was further increased, the cracking of the masonry close to the left corner and the tensile failure of the CFRP strip at the fold at the left corner, also accompanied by diffuse debonding, were attained. Actually the extensive debonding phenomena at the corner was observed concurrently with the failure of the strip; it involved mainly the masonry-levelling grout interface, while the grout-CFRP bond remained effective.
Consistently with the crack pattern, the crack opening at midspan resulted higher for pulling than pushing. The inward horizontal translations at supports when pushing were slightly higher at the left side in positive load direction, and the opposite was observed when pulling. However, the corner rotations were almost symmetric.

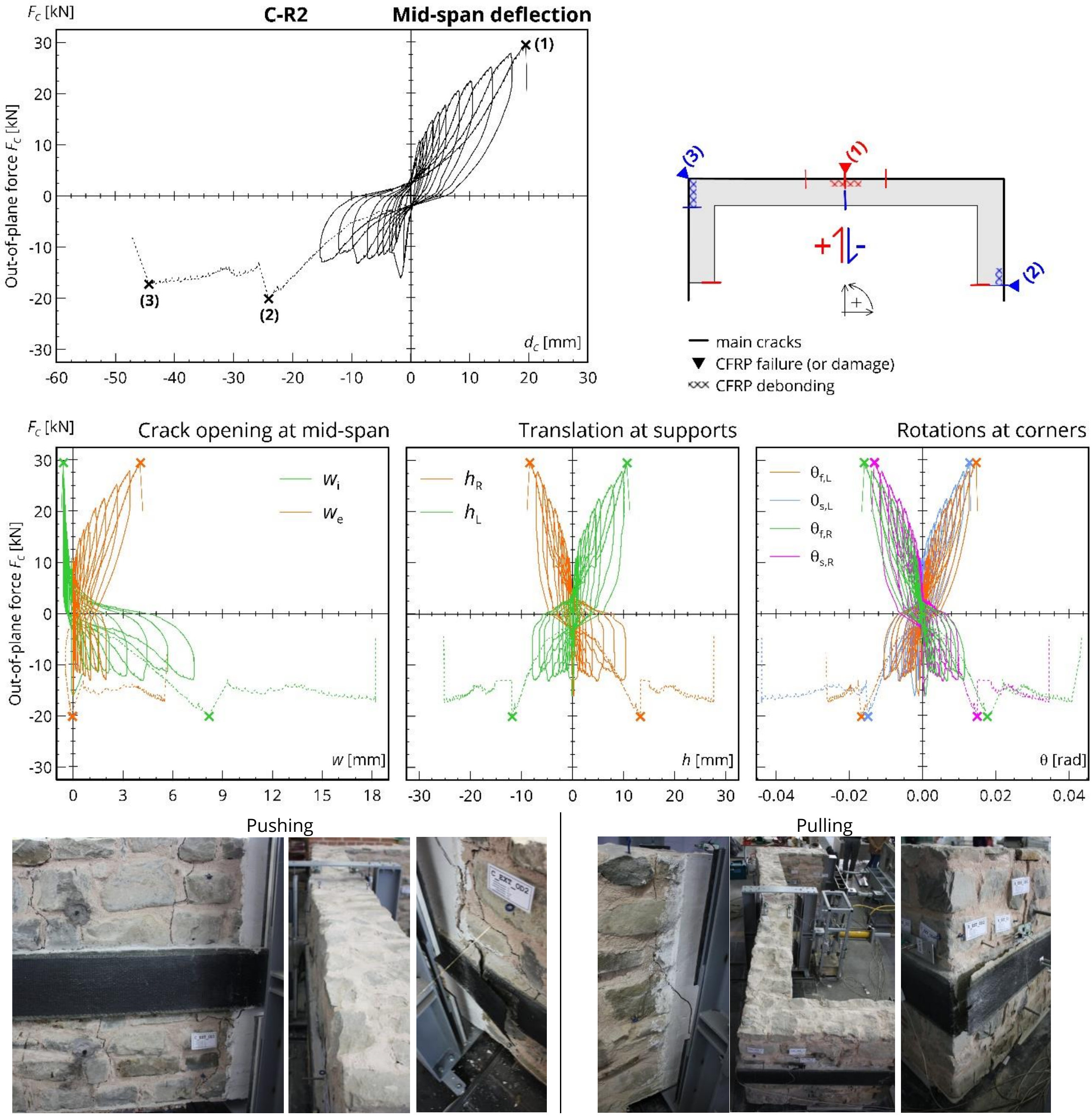

Fig. 5.2.3 Main results of test C-R2.

- Test C-B1 (Fig. 5.2.4)

The first crack, almost vertical, appeared in the masonry at the mid-span, on the outer side, for the attainment of the flexural tensile strength of the solid clay masonry parallel to the bed joint, when pushing. However, no significant load decrease occurred with the crack opening (just a slight stiffness degradation) because of the presence of the CFRP reinforcement. In contrast, the opening of a midspan vertical crack on the inner side, when pulling, induced a rapid load decrease. Afterwards, the load was gradually recovered in subsequent cycles but with a significant stiffness reduction. As the cyclic test progressed, the midspan crack alternatively opened on the outer side when pushing and on the inner side when pulling. As the deflection increased, a slight CFRP debonding was observed around the outer crack (masonry-grout interface), and new sub-vertical cracks opened at about 250–300 mm from the midspan section, as a consequence of the stress distribution effect of the CFRP strip). Because of this cracks, the stiffness reduced further. Some debonding also occurred near the right clamp, but the strip remained effective in carrying the tensile strength. The failure of the CFRP strip (tensile fracture of the fibres) occurred abruptly at the midspan with significant values of deflection. When loading monotonically in the opposite direction (pulling), the masonry began cracking in the vicinity of the corners and some diagonal and horizontal cracks appeared in the central part of the sample. The collapse occurred for the tensile failure of the CFRP strip at the left corner and, then, at the right side, near the corner bend. Some CFRP debonding was also observed in these sections, just before the failure.

The trend of the horizontal displacements at the wing extremities indicates quite comparable values of inward and outward lateral movement associated with a given deflection level. However, slightly higher translations occurred at the left side for both loading directions. The rotations at the corners almost coincided for both sides until achieving the positive peak value, after which a slightly asymmetrical behaviour occurred in the final loading cycle, with higher rotations at the right corner compared to the left. This was most likely due to the inhomogeneity of the masonry and imperfect symmetry of the damage. Consequently, the outward support translation was higher on the left than on the right side.

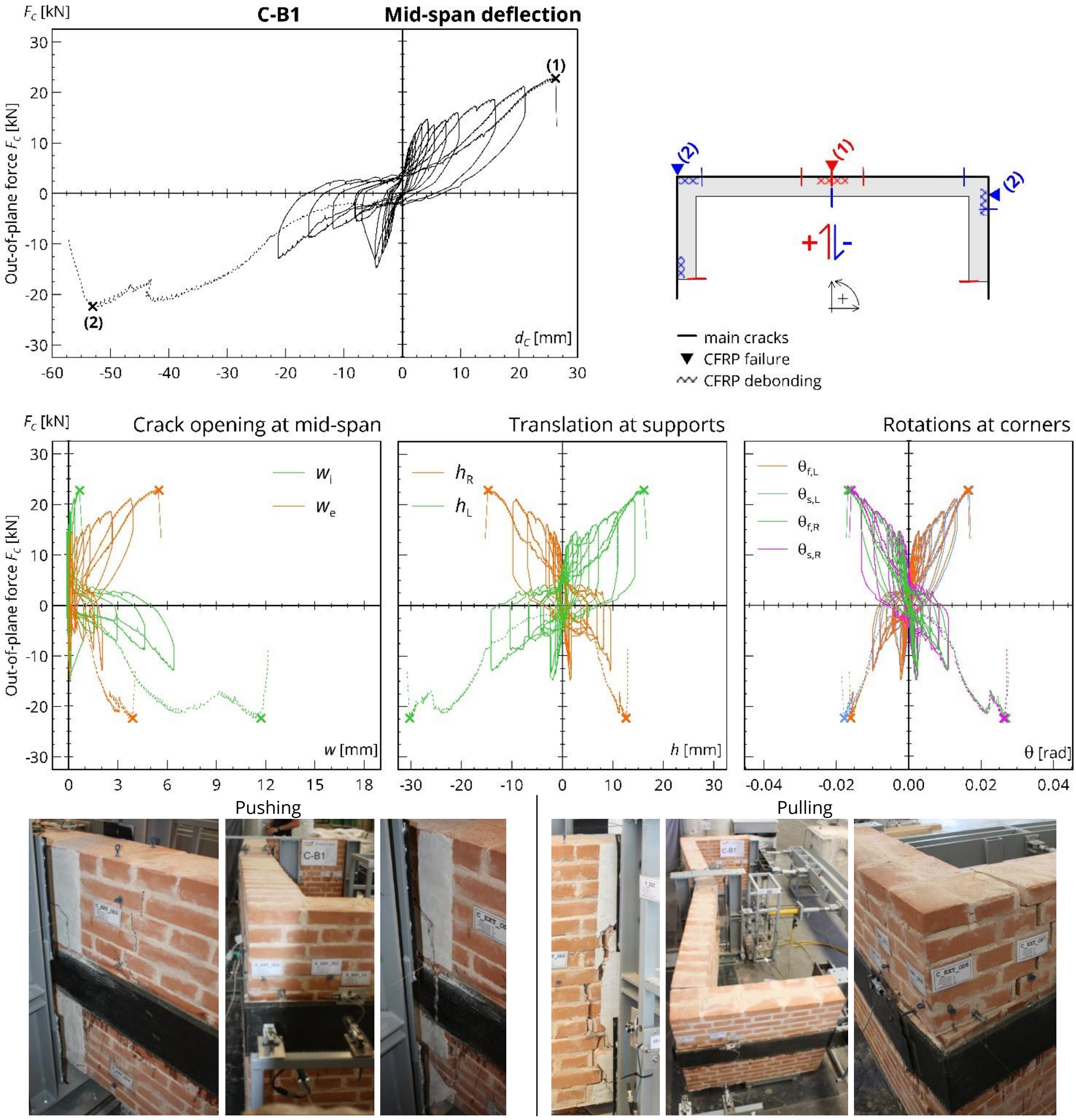

Fig. 5.2.4 Main results of test C-B1.

.

The main results of the two tests in terms of load and deflection at first cracking (*Cr*) and at collapse (*Ul*) are summarised in Table 5.1 and Fig. 5.2.5. Since the eccentric reinforcement intervened differently, depending on the loading direction, the envelope of the load-deflection capacity curves had asymmetric trend: when pulling, the trend is elastic-plastic with hardening (end of the elastic phase at first cracking); when pushing, a sudden load decrease interrupts the elastic stage at first cracking, then a plastic stage with hardening is detected. When pushing, the CFRP strip fractures at the mid span; when pulling, the CFRP strip fractured around the corners. Sample C-R2 exhibited in pushing a peak resistance of +29.6 kN and a deflection 1/187 of the net span. The peak resistance and respective deflection in pulling were -20.3 kN, at 1/152 of the span and were lower than expected, since affected by the premature damage of fibres at the support and at the corner bend, as previously described.
Because of the smaller thickness, the resistances of C-B1 sample were lower (~22.6 kN for both loading directions). Because of different stiffness, the ultimate deflection for pulling (equal to 1/70 of the net span) resulted approximately twice that for pushing (1/140 of the net span).

Table 5.1. Main results of the tests on masonry ring beams with externally bonded FRP strips, in terms of load and deflection at first cracking (Cr) and at collapse (Ul).

		First cracking (*Cr*)		**Ultimate load (*Ul*)**	
Sample	**Load direction**	**F_C [kN]**	**d_C [mm]**	**F_C [kN]**	**d_C [mm]**
C-R2	Push (+)	+9.6	+1.2	+29.6	+19.5
	Pull (−)	−14.0	−1.2	−20.3*	−24.1*
C-B1	Push (+)	+10.4	+1.7	+22.9	+26.0
	Pull (−)	−14.8	−4.5	−22.2	−52.8

*premature damage of fibres

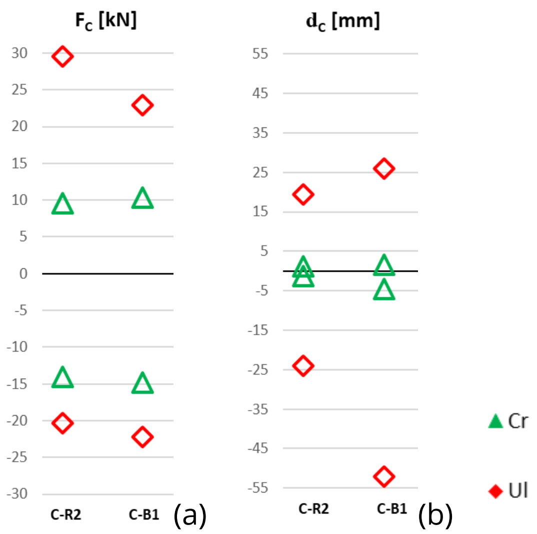

Fig. 5.2.5 Main test results of "C" samples: first cracking and collapse force (a) and deflection (b) values

5.2.2. Analytic model

Symbols:

t	thickness of the masonry cross section	A_C	CFRP cross section
b	width of the masonry cross section	f_C	maximum stress of the CFRP
l	beam span	x_{id}	idealised depth of the neutral axis of the cracked, homogenised cross-section
E_m	masonry Young's modulus	I_{id}	second moment of area of the cracked, homogenised cross-section
E_C	CFRP Young's modulus		
α_C	ratio of the CFRP and masonry Young's moduli (modular ratio) = E_C / E_m		

The static system of the "C" samples to evaluate the resistance is different for pulling (Fig. 5.2.6a) and pushing (Fig. 5.2.6b). For the positive loading (pushing), the system has free rotation at the extremities (vertical crack is free to occur at the inner side of the wings). In the opposite direction (pulling), the rotations are constrained at the extremities (assuming an effective continuity of the CFRP reinforcement), and a moment hinge is at the midspan (representing the vertical crack in masonry at the inner side).

However, according to the static systems, the resistance F_{Max} is the same for both cases - Eq. (5.1):

$$F_{Max} = 4\frac{M_{RM}}{l} \tag{5.1}$$

being M_{RM} the resisting bending moment and F_{Max} the respective load.

The resisting bending moment M_{RM} of the CFRP reinforced cross section (Fig. 5.2.6c) can be estimated according to Eq. (5.2) assuming, for the sake of simplicity, plane cross-sections remain planar after deflection, perfect bond between the reinforcement and masonry, masonry has zero tensile strength and a linear-elastic response in compression, the CFRP reinforcement has a linear-elastic response in tension until reaching maximum stress f_F.

$$M_{RM} = \frac{f_C \cdot I_{id}}{\alpha_C \left(t - x_{id}\right)}, \tag{5.2}$$

$$x_{id} = \frac{\alpha_C \cdot A_C}{b}\left(-1 + \sqrt{1 + \frac{2bt}{\alpha_C \cdot A_C}}\right) \tag{5.3}$$

$$I_{id} = \frac{b \cdot x_{id}^{\,3}}{3} + \alpha_C \cdot A_C (t - x_{id})^2 \tag{5.4}$$

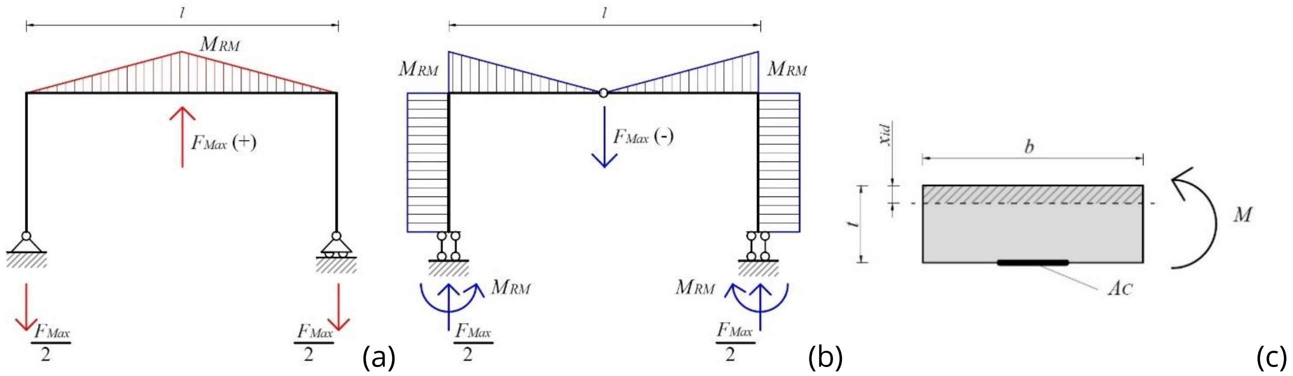

Fig. 5.2.6 "C" samples: static scheme for the evaluation of the resistance in (a) positive and (b) negative directions and (c) reinforced masonry cross-section.

5.2.3. Application and validation

The analytical results are reported in Fig. 5.2.7, also in comparisons with the experimental outcomes.

Main data		
l	[mm]	3650
b	[mm]	1000
E_F	[MPa]	353000
A_F	[mm^2]	66.6
f_F	[MPa]	1314

		C-R2	**C-B1**
t	[mm]	350	250
E_m	[MPa]	1074.2	1638.6
α_F	[-]	329	215
x_{id}	[mm]	103.8	71.6
I_{id}	[mm^4]	1.7E+09	5.8E+08
M_{RM}	[kN·m]	27.6	19.8
F_{Max}	[kN]	30.3	21.7

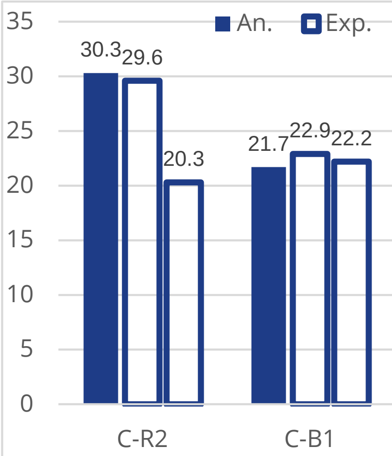

Fig. 5.2.7 Analytic results concerning the out-of-plane tests and comparison with the experimental behaviour.

6. Conclusions

The detailed review and critical analysis of the "CONSTRAIN" experimental tests were achieved, with focus on masonry piers and spandrels strengthened with CRM and subjected to in plane loads, and masonry elements strengthened with CRM, CFRP strips and GFRP meshes embedded in the bed joints, subjected to out-of-plane bending. The mechanical response was described through appropriate, simple analytical-mechanical models, useful for preliminary design purposes. The ongoing parametric numerical analyses (under activities A1.2 and A1.3 of the PRO-SIS project) will allow for further refinement and validation of the proposed analytical models, to be adopted by professional designers.

Acknowledgments

The PRO-SIS project is funded by the Interreg VI-A Italy-Slovenia Programme 2021-2027, co-funded by the European Union.
All the project partners that actively contributed to the project are gratefully acknowledged.

References

[1] ATC. FEMA440 - Improvement of nonlinear static seismic analysis procedures. Washington, D.C., 2005.

[2] MIT - Ministero delle Infrastrutture e dei Trasporti. Circolare 21 gennaio 2019, n. 7 C.S.LL.PP.: Istruzioni per l'applicazione dell'«Aggiornamento delle "Norme tecniche per le costruzioni"» di cui al decreto ministeriale 17 gennaio 2018. 2019

[3] MIT - Ministero delle Infrastrutture e dei Trasporti. Aggiornamento delle «Norme tecniche per le costruzioni». Decreto 17 gennaio 2018.

[4] CNR DT 215/2018 Guide for the Design and Construction of Externally Bonded Fibre Reinforced Inorganic Matrix Systems for Strengthening Existing Structures.

[5] ATC. FEMA 306 - Evaluation of earthquake damaged concrete and masonry wall buildings – basic procedures manual. Washington, D.C., 1999.

[6] Tomazevic M. Earthquake-resistant Design of Masonry Buildings, Series on Innovation in Structures and Construction. Imperial College Press: London, UK, 1999.

[7] Castori G., Borri A, Corradi M, Righetti L. Structural analysis of transversal steel connectors applied on multi-leaf walls. In: Proceedings of the 13th Canadian Masonry Symposium, 4-7 June 2017, Halifax, Canada.

Appendix A.

Material characteristics

I. Masonry characteristics

Three different masonry types were considered in the "CONSTRAIN" experimental campaign (Fig. I.1): double leaf rubble stone masonry, 350 mm thick (R2), double leaf solid clay brick masonry, 250 mm thick (B2) and single leaf solid clay brick masonry, 250 mm thick (B1).

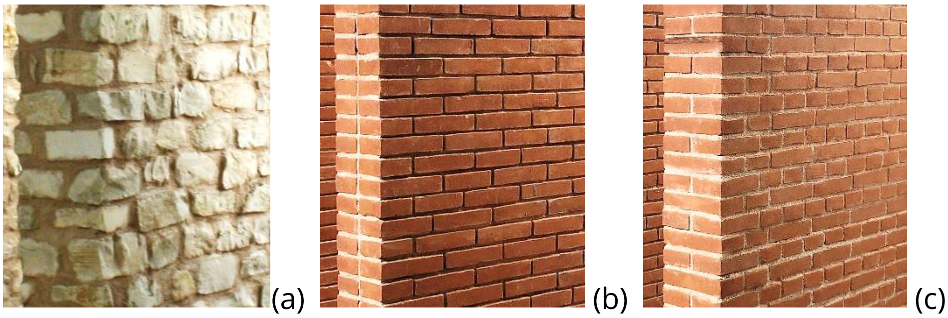

Fig. I.1 Masonry types (a) R2, (b) B2 and (c) B1.

The stone units were a mix of two Credaro stones: Berrettino (sandstone) and Medolo (limestone), with approximate compressive and flexural strengths of 160 MPa and 20 MPa, respectively. The units had approximate dimensions of 150x100x210 mm^3 (width x height x length), laid in a two-leaves masonry configuration, although there was substantial size variability between the elements. The thickness of the joints was about 10 mm but varied significantly due to the irregular shape of the stones.
The solid clay bricks (120x55x250 mm^3, width x height x length) had a surface roughness replicating the typical appearance of old masonry structures and had a nominal compressive strength of 18 MPa. The bricks in the samples were arranged in two different bond patterns (~10 mm thick joints). The former (for masonry B2) replicated a double-leaf masonry wall composed of two adjacent, independent wythes made up following the "stretcher bond"; headers were provided at the ends of alternating rows. The latter (for masonry B1) followed to the "English bond", alternating courses of headers and stretchers, with headers laid centred over the stretchers in the course below.
All the masonry types were assembled with a natural lime mortar simulating the weak mortar typically found in historical buildings. It was a mixture of natural hydraulic lime and sand, in a lime-to-sand ratio of 1:7 by mass (i.e., 200 kg hydraulic lime and 1400 kg of sand per m^3 of mortar). The mean values of flexural ($f_{b,f}$) and compressive strength ($f_{b,c}$) are reported in Table A.1.

Table A.1 Mechanical properties from tests on masonry prisms.

Ref. sample name	n° samples	Age [days]	Mechanical properties	
			$f_{b,f}$ [MPa] (CoV [%])	$f_{b,c}$ [MPa] (CoV [%])
S-R2-1, A3_1, A3_1	-	-	0,23 (18 %)	1,11 (17 %)
S-R2-2	21	36	0,36 (23%)	1,95 (12 %)
S-B1	/	/	/	/
S-B2	21	38	0,30 (15 %)	1,86 (6 %)
A2_1, A2_2	6	34	0,30(10 %)	1,50 (9 %)
A1_1, A1_1	6	97	0,29 (12 %)	1,63 (7 %)
T1	12	43	0,76 (10 %)	1,99 (11 %)
T2	6	43	0,59 (5 %)	1,62 (7 %)
P-R2U, P-R2R-1, P-R2R-2, B-R2	12	66	0.17 (16%)	0,93 (5 %)

For each of the three masonry types, monotonic compressive tests were carried out on two masonry wallets (500 mm width, 1000 mm height); the main test results are summarized in Table A.2 **-** Table A.4.

Table A.2 Mechanical properties of stone masonry (R2).

Sample ID	Peak force [kN]	Compressive strength [MPa]	Young modulus [MPa]	Ultimate strain [%]
A3_1	451.64	2.58	1162.0	1.2 %
A3_2	416.96	2.38	986.4	2.8 %
Average	**434.30**	**2.48**	**1074.2**	**2 %**

Table A.3 Mechanical properties of double-leaf brick masonry (B2).

Sample ID	Peak force [kN]	Compressive strength [MPa]	Young modulus [MPa]	Ultimate strain [%]
A2_1	875.60	6.86	2073.5	1.1
A2_2	750.68	6.00	2293.1	*
Average	**813.14**	**6.43**	**2183.3**	**1.1**

* Instruments were damaged after reaching a strain of 0.37%

Table A.4 Mechanical properties of single-leaf brick masonry (B1).

Sample ID	Peak force [kN]	Compressive strength [MPa]	Young modulus [MPa]	Ultimate strain [%]
A1_1*	490.3	3.8	1589.1	0.35
A1_2	852.4	6.7	2341.1	**
Average	**852.4**	**6.7**	**2341.1**	**-**

* Failure of the sample was eccentric. Values are not considered.
** Instruments were damaged after reaching a strain of 0.3%

II. Strengthening materials characteristics

For the CRM, a pre-mixed natural hydraulic lime mortar was used for the coating. The mean values of flexural ($f_{c,f}$) and compressive strengths ($f_{c,c}$) are reported in Table A.5.

Table A.5 Mechanical properties of mortar for strengthening.

Ref. sample name	n° samples	Age [days]	Mechanical properties	
			$f_{c,f}$ [MPa] (CoV [%])	$f_{c,c}$ [MPa] (CoV [%])
S-R2-1	3	40	4,2 (5 %)	22,9 (10 %)
S-R2-2	12	38	5,6 (4%)	24,6 (5 %)
S-B1	12	84	4,4 (7 %)	20,1 (8 %)
S-B2	15	39	3,9 (15 %)	15,0 (20 %)
P-R2R-1, P-R2R-2,B-R2	6	35	3,0 (10 %)	30,1 (4%)

The preformed FRP meshes (Fig. II.*1*) embedded within the coating were composed of long Alkali-Resistant glass fibres embedded in a thermosetting resin made of epoxy vinylester with benzoyl peroxide as catalyst (Glass FRP - GFRP). They had a 66x66 mm^2 grid dimension and were composed of twisted-fibre wires in the warp direction, weaved on parallel-fibre wires in the weft direction (dry fibre cross-sectional area in the wire of 3.8 mm^2). The main mechanical properties are presented in Table A.6The same type of meshes were used also for the masonry ring beams samples with meshes embedded in bed joints.


(a)
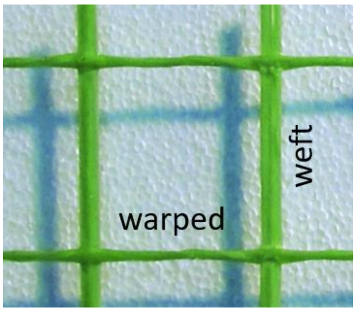

(b)

Fig. II.1 GFRP mesh for the CRM system: (a) general view of the mesh rolls and (b) detail.

Table A.6 Mechanical properties of the GFRP mesh: tensile resistance T_G, ultimate strain $\varepsilon_{u,G}$ and axial stiffness EA_G.

	Twisted fibres wires		Parallel fibres wires	
Property	**Mean**	**COV (%)**	**Mean**	**COV (%)**
T_G (kN)	5.11	2.4	5.93	3.9
$\varepsilon_{u,G}$ (%)	1.85	1.9	2.03	4.2
EA_G (kN)	276.7	2.6	291.2	1.6

The GFRP L-shaped connectors had a cross-section of 7 x 10 mm^2, with a dry fiber cross section of 32.4 mm^2 (nominal characteristic tensile strength of 17 kN and ultimate strain of 1.9 %.) - Fig.

II.2a. The holes drilled in the masonry had a diameter of 24 mm for double-side application (with connectors overlapping length of at least 200 mm), and of 16 mm for sigle-sided. The hole were injected with bi-component vinylester chemical anchor. The GFRP mesh sheets were 165x165 mm^2, with a 33x33 mm^2 mesh grid dimension (Fig. II.2b).

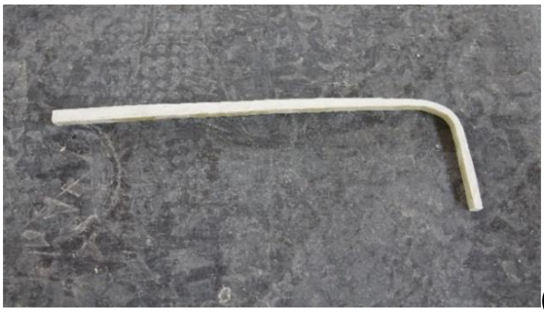(a) (b)

Fig. II.2 GFRP transversal connections: (a) the "L"-shape connector and (b) the mesh sheets.

The artificial diatons (Fig. II.3) were made with a 16 mm diameter threaded stainless steel bar (AISI 316) embedded in a 50 mm diameter core of high resistance thixotropic cement-based mortar and were provided at the head with a perforated stainless steel washers (4 mm thick, 150 mm diameter), with a nut welded at the centre, screwed on the head of the threaded bar.

(a) (b)

Fig. II.3 Artificial diaton: (a) assembling of the steel connector and (b) detail of the perforated head washer.

Generally, the number, position and diameter of connectors are crucial for the transversal tying and depend on the masonry texture, thickness and mechanical characteristic. In lack of a specific design procedure, reference was made to the literature. In particular, the GFRP injected connectors were distributed by considering the range 4–6/m^2 suggested by Tomazevic [6] for traditional reinforced-cement coating. For dimensioning the artificial diatons, reference was made to the ranges suggested by Castori et al. [7] for historic hard-stone masonry (barely cut stones and pebbles assembled with lime-based mortars): connector diameter: 16–20 mm; hole diameter to connector diameter ratio: 3–4; connectors distance to hole diameter ratio: 9–11.

The unidirectional CFRP strips for the masonry ring beams with the externally bonded strengthening system (Fig. II.4) had a width of 200 mm and a dry fibre cross-section of 66.6 mm^2 (fibre mass per unit area 600 g/m^2). Epoxy-impregnated CFRP coupons provided mean values of tensile strength and Young modulus of 1314.3 MPa (*CoV* = 8.7%) and 353 GPa (*CoV* = 13.6%), respectively.


(a)
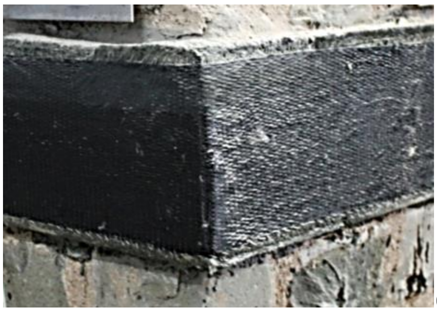
(b)

Fig. II.4 CFRP strips: (a) dry fibres roll and (b) detail of application